Thesis for the Degree of Licentiate of Philosophy

A Two-stage Numerical Procedure for an Inverse Scattering Problem

John Bondestam Malmberg

Division of Mathematics
Department of Mathematical Sciences
Chalmers University of Technology
and University of Gothenburg
Gothenburg, Sweden, 2015

A Two-stage Numerical Procedure for an Inverse Scattering Problem
John Bondestam Malmberg

Department of Mathematical Sciences
Chalmers University of Technology
and University of Gothenburg
SE–412 96 Gothenburg
Sweden
Phone: +46 (0)31-772 10 00

Typeset with LaTeX.
Printed in Gothenburg, Sweden, 2015.

Abstract

In this thesis we study a numerical procedure for the solution of the inverse problem of reconstructing location, shape and material properties (in particular refractive indices) of scatterers located in a known background medium. The data consist of time-resolved backscattered radar signals from a single source position. This relatively small amount of data and the ill-posed nature of the inversion are the main challenges of the problem. Mathematically, the problem is formulated as a coefficient inverse problem for a system of partial differential equations derived from Maxwell's equations.

The numerical procedure is divided into two stages. In the first stage, a good initial approximation for the unknown coefficient is computed by an approximately globally convergent algorithm. This initial approximation is refined in the second stage, where an adaptive finite element method is employed to minimize a Tikhonov functional. An important tool for the second stage is a posteriori error estimates – estimates in terms of known (computed) quantities – for the difference between the computed coefficient and the true minimizing coefficient.

This thesis includes four papers. In the first two, the a posteriori error analysis required for the adaptive finite element method in the second stage is extended from the previously existing indirect error estimators to direct ones. The last two papers concern verification of the two-stage numerical procedure on experimental data. We find that location and material properties of scatterers are obtained already in the first stage, while shapes are significantly improved in the second stage.

Keywords: coefficient inverse problem, inverse scattering, backscattering data, approximate global convergence, finite element method, adaptivity, a posteriori error analysis

List of included papers

The following papers are included in this thesis:

- **Paper I.** John Bondestam Malmberg. *A posteriori error estimate in the Lagrangian setting for an inverse problem based on a new formulation of Maxwell's system*, volume 120 of *Springer Proceedings in Mathematics and Statistics*, pages 42–53, Springer, 2015.
- **Paper II.** John Bondestam Malmberg. *A posteriori error estimation in a finite element method for reconstruction of dielectric permittivity*. Preprint.
- **Paper III.** Larisa Beilina, Nguyen Trung Thành, Michael V. Klibanov and John Bondestam Malmberg. Reconstruction of shapes and refractive indices from backscattering experimental data using the adaptivity. *Inverse problems* 30:105007, 2014.
- **Paper IV.** Larisa Beilina, Nguyen Trung Thành, Michael V. Klibanov and John Bondestam Malmberg. Globally convergent and adaptive finite element methods in imaging of buried objects from experimental backscattering radar measurements. *Journal of Computational and Applied Mathematics* (2014), http://dx.doi.org/10.1016/j.cam.2014.11.055.

The following papers are not included in this thesis:

- John Bondestam Malmberg and Larisa Beilina. *Approximate globally convergent algorithm with applications in electrical prospecting*, volume 52 of *Springer Proceedings in Mathematics and Statistics*, pages 29–41, Springer, 2013.
- Larisa Beilina, Nguyen Trung Thành, Michael V. Klibanov and John Bondestam Malmberg. *Methods of Quantitative Reconstruction of Shapes and Refractive Indices from Experimental data*, volume 120 of *Springer Proceedings in Mathematics and Statistics*, pages 13–41, Springer, 2015.

Acknowledgments

I would like to extend my deepest gratitude to Larisa Beilina for introducing me to the strange world known as Research, for giving me just the right amount of encouragement and constructive criticism, for keeping my mind on the work, and for averting my participation in an unnecessary "re-invention of the bicycle"... Our discussions have always left me wiser and with renewed energy.

I am also very grateful to Mohammad Asadzadeh for much the same reasons, and possibly also for keeping my mind *off* the work now and then.

Finally, many but more diffuse thanks to various colleagues at the department – perhaps you are one of them? – for making up what I have for the last few years perceived to be a good and friendly working environment.

John Bondestam Malmberg
Gothenburg, 2015

Contents

Part 1

Introduction

1. The problem framework

In this thesis we study a numerical procedure for solving a so-called *coefficient inverse problem* (CIP) which is an *inverse scattering problem* for electromagnetic wave propagation. In this introduction, we will start from a short description of the physical problem, gradually proceed with the mathematical formulation, and give an overview of the numerical procedure.

As a starting point, let us consider the idea behind radar detection. A basic radar device involves essentially three parts: a transmitter, a receiver, and a processor. This is a very simplified description, but it will be sufficient for our purposes. For a more detailed overview, see for instance the introduction in [16]. The transmitter produces electromagnetic signals at certain frequencies. These electromagnetic signals propagate through the surrounding medium until they hit an obstacle, a *scatterer*. When this occurs, some of the signals are reflected back in (approximately) the direction from which they came. Some of these *backscattered* signals are detected by the receiver when they return to the radar device.

In the processor, information about the scatterer is derived by analyzing the backscattered signals. In the simplest case, when the scatterer is located in air, we deduce the distance between the scatterer and the source, in the direction from which the backscattered signal was received, from the time between the moment the outgoing signal was produced and the moment the backscattered signal was detected. Thus we know where the scatterer is located. By studying the backscattered signal more carefully additional information about the scatterer can be obtained. The situation is much more complicated in practice. Overlap of signals from many scatterers and noisy signals are examples of sources for increased complexity.

The information we seek to determine in this thesis is, in addition to the location of scatterers, also their shapes and material properties. For the latter we seek to classify scatterers as metallic or non-metallic (dielectric) or a mixture of metallic and non-metallic parts. In the case of non-metallic scatterers we also determine their refractive indices.

In many of our target applications, the scatterers are potentially hazardous, such as in the detection of explosives. For that reason we seek to work with a minimal amount of data: only the time-resolved backscattered part of a signal of a single frequency emitted from a single position.

This makes the problem of obtaining good reconstructions more challenging than in the case where more data are available (and the problem is overdetermined).

To summarize: The problem we consider is to, given a single backscattered time-resolved electromagnetic signal, determine the location, shape and basic material properties of the scatterer. In order to understand what the difficulties with this problem are and describe how they may be overcome, let us pass over to a more precise mathematical formulation of the problem. Since Maxwell's equations are fundamental to the mathematical description of electromagnetism, these equations form a natural starting point.

1.1. Maxwell's equations. These well-known equations relate the magnetic flux density $\mathbf{B}$, the electric displacement field $\mathbf{D}$, the magnetizing field $\mathbf{H}$, the electric field $\mathbf{E}$, and the electric current density $\mathbf{J}$, considered as functions of the spatial coordinates $\mathbf{x} = (x, y, z) \in \mathbb{R}^3$ and time coordinate $t \in [0, T]$ for some final time $T > 0$, to each other. On classical differential form, Maxwell's equations are

$$\frac{\partial \mathbf{B}}{\partial t} + \nabla \times \mathbf{E} = 0 \qquad \text{in } \mathbb{R}^3 \times (0, T], \tag{1.1}$$

$$\frac{\partial \mathbf{D}}{\partial t} - \nabla \times \mathbf{H} = -\mathbf{J} - \sigma \mathbf{E} \qquad \text{in } \mathbb{R}^3 \times (0, T], \tag{1.2}$$

$$\nabla \cdot \mathbf{D} = \rho \qquad \text{in } \mathbb{R}^3 \times (0, T], \tag{1.3}$$

$$\nabla \cdot \mathbf{B} = 0 \qquad \text{in } \mathbb{R}^3 \times (0, T], \tag{1.4}$$

where $\nabla = (\partial/\partial x, \partial/\partial y, \partial/\partial z)$, σ is the conductivity of the medium and ρ is the charge density. In addition we have the two constitutive relations

$$\mathbf{B} = \mu \mathbf{H} \qquad \text{in } \mathbb{R}^3 \times (0, T], \tag{1.5}$$

$$\mathbf{D} = \varepsilon \mathbf{E} \qquad \text{in } \mathbb{R}^3 \times (0, T], \tag{1.6}$$

where μ is the magnetic permeability and ε is the dielectric permittivity. They are related to the refractive index n by $n = \sqrt{\mu\varepsilon/c_0}$, where $c_0 \approx 2.9979 \cdot 10^8$ m/s is the speed of light in vacuum.

We also impose the initial conditions

$$\mathbf{E}(\cdot, 0) = 0, \quad \frac{\partial \mathbf{E}}{\partial t}(\cdot, 0) = \mathbf{I}_0 \delta(\mathbf{x} - \mathbf{x}_0) \qquad \text{in } \mathbb{R}^3, \tag{1.7}$$

where $\mathbf{I}_0 \in \mathbb{R}^3$ is a given vector, $\mathbf{x}_0 \in \mathbb{R}^3$ is a given point, and δ is the Dirac delta. These initial conditions describe the initialization of a signal at $\mathbf{x}_0$

at time $t = 0$. We remark that the initial conditions have implications concerning the uniqueness of the solution to the inverse problem. In fact, existing proofs of uniqueness require non-vanishing initial vakues, which is not the case here. Nevertheless it is reasonable to assume that uniqueness holds. Some further comments on this can be found in the included papers.

In the cases studied in the included papers we have made additional assumptions concerning the nature of the medium: it is non-conductive ($\sigma = 0$), non-magnetic (μ is a (known) constant), in absence of charges and currents ($\rho = 0$ and $\mathbf{J} = 0$), isotropic, and stationary (ε is scalar and independent of t). Under these assumptions the medium is completely characterized by the permittivity $\varepsilon = \varepsilon(\mathbf{x})$.

This means that the properties (location, shape, material) of scatterers are encoded in ε. In the background medium we will have one known value for ε, while in a scatterer the value for ε will differ from that in the background. This information gives us both the location and the shape of the scatterer, and by studying the value of ε inside the scatterer, relative to the value in the background, we can compute its refractive index (or classify the material as a metal).

If ε is known, we can (at least in accurate approximation) compute how the medium scatters electromagnetic waves. Since only the electric field $\mathbf{E}$ is available for measurement, we seek a model which does not involve $\mathbf{B}$, $\mathbf{D}$ and $\mathbf{H}$. Under the above assumptions, it is possible to derive such a model formally from (1.1)–(1.6):

$$\mu\varepsilon\frac{\partial^2\mathbf{E}}{\partial t^2} + \nabla\times(\nabla\times\mathbf{E}) = 0 \qquad \text{in } \mathbb{R}^3\times(0,\,T], \tag{1.8}$$

$$\nabla\cdot(\varepsilon\mathbf{E}) = 0 \qquad \text{in } \mathbb{R}^3\times(0,\,T]. \tag{1.9}$$

In Papers I and II, equations (1.8) and (1.9) are combined into a specific formulation which relies on the assumptions (positivity and regularity) on ε, which are required to treat the inverse problem. This formulation is:

$$\mu\varepsilon\frac{\partial^2\mathbf{E}}{\partial t^2} - \Delta\mathbf{E} - \nabla\left(\frac{\nabla\varepsilon\cdot\mathbf{E}}{\varepsilon}\right) = 0 \qquad \text{in } \mathbb{R}^3\times(0,\,T], \tag{1.10}$$

where $\Delta = \partial^2/\partial x^2 + \partial^2/\partial y^2 + \partial^2/\partial z^2$ is the Laplacian.

In Papers III and IV we use the *stabilized scheme*, see for instance [14, 15],

$$\mu\varepsilon\frac{\partial^2\mathbf{E}}{\partial t^2} + \nabla\times(\nabla\times\mathbf{E}) - \xi\nabla(\nabla\cdot(\varepsilon\mathbf{E})) = 0 \quad \text{in } \mathbb{R}^3\times(0,T], \tag{1.11}$$

where $\xi \geq 1$ is a parameter reflecting how strongly we wish to enforce (1.9). Regardless of which one of equations (1.10) and (1.11) is used, if we know ε we can compute the corresponding electric field $\mathbf{E} = \mathbf{E}_\varepsilon$. But the problem we study is the *inverse* one, that is, to determine the function $\varepsilon(\mathbf{x})$ given measurements of the electric field $\mathbf{E}_\varepsilon$.

1.2. The inverse problem. Suppose that we have backscattered data $\mathbf{G}$ for the electric field generated by a single source, measured on some surface $\Gamma \subset \mathbb{R}^3$. Later, we will assume that Γ is (a part of) the boundary of some domain in $\mathbb{R}^3$. To determine the nature of the scatterer (or scatterers) which generated the data we seek to determine the function ε such that

$$\mathbf{E}_\varepsilon = \mathbf{G} \text{ on } \Gamma. \tag{1.12}$$

Note that, although we can compute $\mathbf{E}_\varepsilon$ for any given (admissible) ε, $\mathbf{E}_\varepsilon$ does not depend on ε in a simple and explicit manner. Hence (1.12) is very difficult to solve directly in its current form. In order to find a solution algorithm, we must first rewrite (1.12) on a more appropriate form by observing that

$$\mathbf{E}_\varepsilon = \mathbf{G} \text{ on } \Gamma \quad \Longleftrightarrow \quad \|\mathbf{E}_\varepsilon - \mathbf{G}\|_\Gamma = 0,$$

where $\|\cdot\|_\Gamma$ is an appropriate norm over Γ. Moreover, as $\|\mathbf{E}_\varepsilon - \mathbf{G}\|_\Gamma > 0$ whenever $\mathbf{E}_\varepsilon - \mathbf{G} \neq 0$ on Γ, we may seek ε by minimizing the functional

$$F(\varepsilon) := \|\mathbf{E}_\varepsilon - \mathbf{G}\|_\Gamma .$$

This, however, does still not give a suitable method. There are two significant difficulties involved in the minimization of F. Firstly, due to the ill-posed nature of the problem, we cannot guarantee the existence of a minimizer to F for any given $\mathbf{G}$ (which may – and in practice *will* – contain noise). Secondly, even if a minimizer exists we may not be able to find it by standard minimization methods because the functional F may have local minima, possibly far away from the global minimizer for which $F(\varepsilon) = 0$. Thus we need a sufficiently good starting approximation for the minimizer.

The first difficulty can be handled by the method of Tikhonov, developed for ill-posed problems (see for example [9, 17]). By this method, we assume that there exists ideal noiseless data $\mathbf{G}^*$ corresponding to the exact permittivity ε^*. We also assume that the data $\mathbf{G}$ has a known noise level δ such that $\|\mathbf{G}^* - \mathbf{G}\|_\Gamma \leq \delta$. Then F is replaced by the *Tikhonov functional* F_α defined by

$$F_\alpha(\varepsilon) := \frac{1}{2}\|\mathbf{E}_\varepsilon - \mathbf{G}\|_\Gamma^2 + \frac{\alpha}{2}\|\varepsilon - \varepsilon_0\|_\varepsilon^2, \tag{1.13}$$

where $\alpha > 0$ is a (small) *regularization parameter* which should be selected appropriately with regard to the noise level δ (in particular $\alpha = \alpha(\delta) \to 0+$ when $\delta \to 0+$), $\|\cdot\|_\varepsilon$ is another suitable norm, and ε_0 is an initial approximation to ε^*. Under some assumptions on α and ε_0 one can guarantee that a minimizer of F_α exists, and that this minimizer tends to the exact permittivity ε^* as the noise level δ tends to zero.

The second difficulty – that of finding a sufficiently good initial approximation to avoid local but non-global minima – remains, and more explicitly so since such an approximation is required by the definition of F_α. As we will see in the next section, it is possible to construct such an initial approximation.

Once a good initial approximation is obtained we can minimize F_α and thus determine the nature of the scatterers to an accuracy determined by the level of noise in $\mathbf{G}$. We will return to the minimization in Section 3.

2. The first stage: A globally convergent method

As we saw in the previous section, before we can proceed with the minimization approach to the inverse problem, we must determine a good initial approximation for the exact coefficient ε^*. In this section we give an overview of a globally convergent method, originally described in [4], for finding such an approximation. This is the first stage of the two-satge procedure referred to in the title of this thesis.

Here we study only one component of the electric field, the component parallel to the vector $\mathbf{I}_0$ of (1.7), which we denote by u. We describe it by the scalar wave equation, rather than a system derived from Maxwell's

equations:

$$\mu\varepsilon\frac{\partial^2 u}{\partial t^2} - \Delta u = 0 \qquad \text{in } \mathbb{R}^3 \times (0,\, T], \tag{2.1}$$

$$u(\cdot,\, 0) = 0, \quad \frac{\partial u}{\partial t}(\cdot,\, 0) = |\mathbf{I}_0|\, \delta(\mathbf{x} - \mathbf{x}_0) \qquad \text{in } \mathbb{R}^3. \tag{2.2}$$

where we assume that the coefficients ε and μ are the same as in (1.10) or (1.11), and the initial conditions (2.2) come from the corresponding components of (1.7).

Our goal is to transform (2.1) so that ε can be isolated to one side of the equation. The most straight-forward approach, to write

$$\varepsilon(\mathbf{x}) = \frac{1}{T}\int_0^T \frac{\Delta u(\mathbf{x},\, t)}{\mu\frac{\partial^2 u}{\partial t^2}(\mathbf{x},\, t)}\, \mathrm{d}t,$$

is appropriate either in the case when we have complete data, that is, when $u(\mathbf{x},\, t)$ is known from measurements for every $\mathbf{x}$ and t, or when the initial conditions are non-vanishing (see [6]). Since neither of these cases are applicable here, we instead start by *Laplace transformation*:

$$\tilde{u}(\mathbf{x},\, s) \coloneqq \int_0^\infty u(\mathbf{x},\, t)\mathrm{e}^{-st}\, \mathrm{d}t, \tag{2.3}$$

where the variable $s \geq \underline{s} > 0$ is referred to as the *pseudo-frequency*.

For $\mathbf{x} \neq \mathbf{x}_0$, this transformation together with (2.1) results in the equation

$$\mu\varepsilon s^2\tilde{u} - \Delta\tilde{u} = 0. \tag{2.4}$$

It can be shown (see Section 2.7 of [5]) that $\tilde{u}$ is positive, and bounded as $|\mathbf{x}| \to \infty$, hence the following function is well-defined:

$$v(\mathbf{x},\, s) \coloneqq \frac{\ln\tilde{u}(\mathbf{x},\, s)}{s^2}. \tag{2.5}$$

Using the function v we can write $\tilde{u} = \exp(s^2 v)$, and obtain

$$\Delta\tilde{u} = \left(\Delta v + s^2(\nabla v)^2\right) s^2\tilde{u},$$

which with (2.4) gives us the following expression for ε:

$$\varepsilon = \frac{1}{\mu}\left(\Delta v + s^2(\nabla v)^2\right). \tag{2.6}$$

In other words, if we know the function $v(\mathbf{x},\, s)$ (for any $s \geq \underline{s}$) we can compute $\varepsilon = \varepsilon(\mathbf{x})$ explicitly from (2.6). Though the function v is a priori unknown, the asymptotic behaviour of v and its derivatives with respect

to s, for large s, can be predicted (Lemma 2.2 and following remark concerning smoothness in [11]):

$$v(\mathbf{x},\, s) = \frac{f(\mathbf{x})}{s} + \mathcal{O}(s^{-2}), \quad s \to \infty, \tag{2.7}$$

where f is as regular as $\tilde{u}$ with respect to the spatial variable.

Via truncation, this gives us a method for iteratively computing v, hence ε, from a first approximation of the *tail function*

$$V(\mathbf{x}) \coloneqq v(\mathbf{x},\, \overline{s}), \tag{2.8}$$

where $\overline{s} > \underline{s}$ is a sufficiently large pseudo-frequency.

2.1. The iterative procedure. We start by differentiating (2.6) with respect to s, since ε does not depend on s it vanishes, leaving

$$0 = \Delta q + 2s(\nabla v)^2 + 2s^2 \nabla v \cdot \nabla q,$$

where $q \coloneqq \partial v/\partial s$.

To proceed we make a uniform partition of the interval $[\underline{s},\, \overline{s})$ into N subintervals $[s_n,\, s_{n-1})$, $n = 1, \ldots, N+1$, of length $d = (\overline{s} - \underline{s})/N$. Note that we index pseudo-frequencies in decreasing order, since we aim at a stepping scheme from higher to lower pseudo-frequencies. On each such subinterval we approximate q by a constant function with respect to s, that is:

$$q(\mathbf{x},\, s) \approx q_n(\mathbf{x}), \quad s \in [s_n,\, s_{n-1}).$$

Further, we expand v for $s \in [s_n,\, s_{n-1})$ as

$$\begin{aligned} v(\mathbf{x},\, s) &= V(\mathbf{x}) - \int_s^{\overline{s}} q(\mathbf{x},\, s')\, \mathrm{d}s' \\ &\approx V(\mathbf{x}) - (s_{n-1} - s) q_n(\mathbf{x}) - d \sum_{j=0}^{n-1} q_j(\mathbf{x}), \end{aligned}$$

and so we obtain

$$\begin{aligned} &\Delta q_n + 2s(2s_{n-1} - 3s) \nabla W_n \cdot \nabla q_n \\ &\qquad = 2s(s - s_{n-1})(2s - s_{n-1})(\nabla q_n)^2 - 2s(\nabla W_n)^2, \end{aligned} \tag{2.9}$$

where $W_n \coloneqq V - d \sum_{j=0}^{n-1} q_j$ and we have defined $q_0 = 0$.

Finally, in order to reduce the non-linearity of (2.9), we multiply it by a Carleman weight function $c_{n,\Lambda}(s) := \exp(\Lambda(s_{n-1} - s))$ where $\Lambda \gg 1$ and integrate over $[s_n,\, s_{n-1})$ to obtain

$$\Delta q_n + A_n \nabla W_n \cdot \nabla q_n = B_n(\nabla q_n)^2 - C_n(\nabla W_n)^2 \tag{2.10}$$

with coefficients A_n, $C_n = \mathcal{O}(1)$ and $B_n = \mathcal{O}(\Lambda^{-1})$ which can be calculated explicitly. Thus the term $B_n(\nabla q_n)^2$ can be neglected for large Λ.

The algorithm is, briefly, the following (see also the flowchart, Figure 1 of Paper IV):

(1) Compute an initial approximation for the tail function V using the asymptotics (2.7).
(2) Compute the corresponding function q_n via (2.10) using the data $\mathbf{G}$ (after transformation) for boundary conditions to truncate the problem domain.
(3) Compute the function $v(\mathbf{x},\, s_n) = dq_n(\mathbf{x}) + d\sum_{j=0}^{n-1} q_j(\mathbf{x})$.
(4) Compute ε from v using (2.6).
(5) Compute u from ε using (2.1).
(6) Compute new tail function V from u using transformations (2.3) and (2.5).
(7) Check stopping criteria. If the algorithm has converged for the current n, then step to the next pseudo-frequency interval. Otherwise, repeat from (2) with the new tail function. If the algorithm has converged with respect to the coefficient, then return the last computed coefficient, denoted $\varepsilon_{\text{glob}}$.

2.2. Approximate global convergence. The algorithm outlined above gives a coefficient $\varepsilon_{\text{glob}}$. In Section 1 we claimed that it would be a good initial approximation for the Tikhonov functional F_α defined in (1.13). Here we will confirm this by stating the important properties of $\varepsilon_{\text{glob}}$.

We begin by explaining the *approximately globally convergent* property of the algorithm that produced $\varepsilon_{\text{glob}}$. The term should be understood in the sense that, without additional restrictive assumptions, it can be shown that the coefficient $\varepsilon_{\text{glob}}$ is close to the exact solution ε^*, but we cannot guarantee that $\varepsilon_{\text{glob}}$ tends to ε^* as the computations become increasingly refined. To be more precise, we give the following simplified version of the global convergence theorem (originally Theorem 6.1 of [4], improved in [5]):

THEOREM 2.1. *Assume that the coefficient ε is bounded from below and above by known, positive constants, is sufficiently smooth, and is constant outside a bounded domain Ω. Then if the pseudo-frequencies $\overline{s} > \underline{s} > 1$ and Carleman weight parameter Λ are taken sufficiently large, and the step-size in pseudo-frequency d is sufficiently small, there exist a constant $C > 0$ and a number $\eta \in (0, 1)$, depending on Ω, $\overline{s}$, d, the regularity of the tail function for the exact coefficient ε^*, the noise level in the data, and the bounds on ε, such that*

$$\|\varepsilon_{\text{glob}} - \varepsilon^*\|_\beta \leq C\left(\frac{1}{\sqrt{\Lambda}} + \eta\right), \tag{2.11}$$

where $\|\cdot\|_\beta$ is the Hölder norm

$$\|f\|_\beta \coloneqq \max_{\mathbf{x},\mathbf{y}} \frac{|f(\mathbf{x}) - f(\mathbf{y})|}{|\mathbf{x} - \mathbf{y}|^\beta},$$

for some $\beta \in (0, 1)$ depending on the regularity of ε^*.

The approximate nature of the convergence is reflected in the fact that the quantity on the right hand side of (2.11) can be made small, but not arbitrarily small as the numerical precision increases (unless the noise level in the data drops to zero). However, the next result, which follows directly from Theorem 3.1 of [7] in view of Theorem 2.1, shows that it can be made small enough.

THEOREM 2.2. *If the conditions of Theorem 2.1 hold and the regularization parameter α is selected appropriately with respect to the noise level δ, then the Tikhonov functional F_α defined in* (1.13)*, with $\varepsilon_0 = \varepsilon_{\text{glob}}$, is strongly convex in a neighbourhood of $\varepsilon_{\text{glob}}$, containing the minimizer of F_α.*

It follows in particular that it is possible to minimize F_α using conventional gradient-based methods such as (quasi-) Newton or the conjugate gradient method.

We can conclude that $\varepsilon_{\text{glob}}$ is indeed an initial approximation of the type required, as discussed in Section 1. Numerical experiments show that it is in fact more than that. From the results presented in Papers III and IV, as well as in references therein, we see that two out of the three of the scatterers' properties are accurately reconstructed already by $\varepsilon_{\text{glob}}$. Recall that we seek to determine scatterer's location, shape, and refractive index (or alternatively classify it as metal). Out of these three properties,

the location and refractive index can be determined from $\varepsilon_{\text{glob}}$. The shape is not well reconstructed from $\varepsilon_{\text{glob}}$, which tends to produce disc-shaped approximations, too flat in the direction away from the source of the backscattered signal. Hence it is justified to proceed with the minimization of F_α. The next section gives an overview of how to do this via an adaptive finite element method.

3. The second stage: Adaptivity

In this section we give an overview of adaptive finite elements applied to the minimization problem for the Tikhonov functional F_α defined in equation (1.13). This is the second stage of the two-stage numerical procedure. Our aim is not to give a complete exposition, but instead to underline the principles and ideas behind the method. For the details concerning our particular application, see the included papers. For the theory of finite elements and adaptivity in general, we refer to [8, 10, 12].

It should be noted that it is possible to include adaptivity already in the globally convergent method, when solving equation (2.10) for q_n. This method is described in [1]. Our main reasons to use adaptivity as a second stage, rather than as a part of the procedure outlined in the previous section, are the following: Firstly, we wish to take the full system – (1.7) and (1.10) or (1.11) – into account, which is not the case in the globally convergent method. Secondly, the theory for the two-stage approach is more developed. In particular, it is possible to show the relaxation property of mesh refinements for this approach (Theorem 4.2 of [7]). This property states that the coefficient obtained by minimizing the Tikhonov functional on a refined mesh is strictly closer to the exact minimizer than the coefficient obtained on a coarser mesh is. It follows that the coefficient obtained after the adaptive stage is closer to the exact coefficient ε^* than $\varepsilon_{\text{glob}}$ is.

Since we now have access to a good initial approximation $\varepsilon_{\text{glob}}$ as described above, we can minimize F_α using conventional gradient-base techniques. Such techniques naturally require that the gradient $F'_\alpha(\varepsilon)$ of F_α with respect to ε can be calculated (or accurately approximated). This is far from trivial since $F_\alpha(\varepsilon)$ depends on $\mathbf{E}_\varepsilon$ which in turn depends implicitly on ε via the solution of a partial differential equation.

Via the introduction of a Lagrangian multiplier $\boldsymbol{\lambda}$ in a Lagrangian functional $L(\varepsilon, \mathbf{E}, \boldsymbol{\lambda})$, derived from F_α and the direct equation ((1.10) or (1.11)) for $\mathbf{E}$, where the arguments ε, $\mathbf{E}$, and $\boldsymbol{\lambda}$ are varied independently

of each other, it is possible to find the following expression for $F'_\alpha(\varepsilon)$ acting on $\bar{\varepsilon}$:

$$F'_\alpha(\varepsilon;\,\bar{\varepsilon}) = (\alpha(\varepsilon-\varepsilon_0),\,\bar{\varepsilon})_\varepsilon - \mu(\bar{\varepsilon}\tfrac{\partial \mathbf{E}_\varepsilon}{\partial t},\,\tfrac{\partial \boldsymbol{\lambda}_\varepsilon}{\partial t}) + (\nabla\left(\tfrac{\bar{\varepsilon}}{\varepsilon}\right)\cdot\mathbf{E}_\varepsilon,\,\nabla\cdot\boldsymbol{\lambda}_\varepsilon). \tag{3.1}$$

where $(\cdot,\,\cdot)_\varepsilon$ and $(\cdot,\,\cdot)$ are appropriate inner products, the former corresponding to the norm $\|\cdot\|_\varepsilon$. This expression is valid for the case when (1.10) is used for the direct problem. The corresponding expression for the case when (1.11) is used is

$$F'_\alpha(\varepsilon;\,\bar{\varepsilon}) = (\alpha(\varepsilon-\varepsilon_0),\,\bar{\varepsilon})_\varepsilon - \mu(\bar{\varepsilon}\tfrac{\partial \mathbf{E}_\varepsilon}{\partial t},\,\tfrac{\partial \boldsymbol{\lambda}_\varepsilon}{\partial t}) + \xi(\nabla\cdot(\bar{\varepsilon}\mathbf{E}_\varepsilon),\,\nabla\cdot\boldsymbol{\lambda}_\varepsilon), \tag{3.2}$$

In (3.1) and (3.2), $\mathbf{E}_\varepsilon$ denotes the solution to the direct problem with the given coefficient ε, and $\boldsymbol{\lambda}_\varepsilon$ denotes the solution to an *adjoint* problem where the difference $\mathbf{E}_\varepsilon - \mathbf{G}$ enters as boundary data.

If $\mathbf{E}_\varepsilon$ and $\boldsymbol{\lambda}_\varepsilon$ could be computed exactly, then the inverse problem would essentially be solved at this point, but this is not feasible in general. Instead approximations $\mathbf{E}_h$ and $\boldsymbol{\lambda}_h$ as well as an approximate coefficient ε_h must be used.

We obtain such approximations via a finite element method. That is, we divide space and time into (small) subdomains and prescribe that the approximations $\mathbf{E}_h$, $\boldsymbol{\lambda}_h$ and ε_h should be described by simple functions (polynomials of fixed maximum degree) on each subdomain. In theory, as the subdomains are made arbitrarily small, the approximations will be arbitrarily close to the true solutions. Numerically, this cannot be achieved as we cannot perform infinitely accurate computations. The question is instead how to obtain solutions with a desired finite precision at a minimum computational cost (in principle using as few subdomains as possible).

This leads us to adaptive methods, where the computational mesh is successively refined locally in regions where the contribution to the total error is large. In principle, the method follows these steps:

(1) Make an initial (coarse) computational mesh.
(2) Compute approximations $\mathbf{E}_h$, $\boldsymbol{\lambda}_h$ and ε_h by iterative minimization on the current mesh.
(3) On the basis of the computed approximations, estimate the error $\varepsilon_h - \varepsilon$, where ε is the exact minimizer, in every subdomain of

the mesh. If the sum of local errors is smaller than a preset tolerance, ε_h is an acceptable approximation and the computations are done. Otherwise

(4) refine the mesh by subdividing those subdomains where the error is large. Then repeat from step (2).

Proceeding in this manner we eventually obtain a sufficiently accurate approximation ε_h of the exact minimizer ε of the Tikhonov functional F_α in (1.13). The exact minimizer will be as close to the exact solution ε^* as can be expected, given the noise in the data and accuracy of the numerical approximations, provided that the regularization parameter α is selected correctly. Thus we obtain the last property, the shape, of the scatterer from ε_h, with as good accuracy as can reasonably be expected.

A critical step in the adaptive algorithm is the estimation of the approximation error in terms of the computed quantities. Such estimates are known as *a posteriori* error estimates. In Papers III and IV we have used an estimate for $L(\varepsilon, \mathbf{E}_\varepsilon, \boldsymbol{\lambda}_\varepsilon) - L(\varepsilon_h, \mathbf{E}_h, \boldsymbol{\lambda}_h)$ from [3]. Such estimates for the Lagrangian represent only an indirect indicator of the main error of interest, $\varepsilon_h - \varepsilon$. In Paper II we give a direct estimate for that error.

3.1. The nature of the estimates. We conclude this section by giving a short review of the a posteriori error estimates and the techniques used to derive them. For the details, see Papers I and II.

Our main tools are linearization (neglecting terms of higher order with respect to the errors, which will be small compared to terms of lower order), optimality of the solutions (which in the terminology of finite elements can be viewed as Galerkin orthogonalities), and the strong convexity of the Tikhonov functional.

Mathematically, the optimality (or Galerkin orthogonality) can be expressed as follows: Let $\mathbf{u} := (\varepsilon, \mathbf{E}_\varepsilon, \boldsymbol{\lambda}_\varepsilon)$ denote the minimizer of the Lagrangian, that is, ε minimizes the Tikhonov functional, and let $\mathbf{u}_h := (\varepsilon_h, \mathbf{E}_h, \boldsymbol{\lambda}_h)$ denote the finite element approximation of $\mathbf{u}$. Then

$$L'(\mathbf{u}; \mathbf{v}) = 0 \quad \forall \mathbf{v} \in V, \tag{3.3}$$

where V is an appropriate function space, and

$$L'(\mathbf{u}_h; \mathbf{v}_h) = 0 \quad \forall \mathbf{v}_h \in V_h, \tag{3.4}$$

where V_h is the subspace of V in which the finite element approximations are sought. Specifically, (3.3) implies that

$$F'_\alpha(\varepsilon;\, \bar{\varepsilon}) = 0 \tag{3.5}$$

for any $\bar{\varepsilon}$ from the space containing the admissible coefficients.

The strong convexity of the Tikhonov functional implies the following inequality, which is critical to the estimate for $\varepsilon - \varepsilon_h$,

$$\|\varepsilon_1 - \varepsilon_2\|^2 \le C\left(F'_\alpha(\varepsilon_1;\, \varepsilon_1 - \varepsilon_2) - F'_\alpha(\varepsilon_2;\, \varepsilon_1 - \varepsilon_2)\right) \tag{3.6}$$

for any ε_1 and ε_2 in a neigbourhood of $\varepsilon_{\text{glob}}$, and some constant C. Here and throughout the rest of the section $\|\cdot\|$ should be interpreted as "some appropriate norm", which may vary depending on the quantity being normed by $\|\cdot\|$.

The error estimate for the Lagrangian is derived as follows, starting by linearization:

$$L(\mathbf{u}) - L(\mathbf{u}_h) \approx L'(\mathbf{u}_h;\, \mathbf{u} - \mathbf{u}_h) = L'(\mathbf{u}_h;\, \mathbf{u}) - L'(\mathbf{u}_h;\, \mathbf{u}_h).$$

Since $\mathbf{u}_h \in V_h$ we may drop the last term, in view of (3.4). This will leave us with only the first term, containing the unknown quantity $\mathbf{u}$. Thus this does not give an a posteriori estimate. However, we can instead replace $L'(\mathbf{u}_h;\, \mathbf{u}_h)$ by $L'(\mathbf{u}_h;\, \Pi_h\mathbf{u})$ where $\Pi_h\mathbf{u}$ is an *interpolant* of $\mathbf{u}$ in V_h. This gives

$$\begin{aligned} L(\mathbf{u}) - L(\mathbf{u}_h) &\approx L'(\mathbf{u}_h;\, \mathbf{u}) - L'(\mathbf{u}_h;\, \Pi_h\mathbf{u}) \\ &= L'(\mathbf{u}_h;\, \mathbf{u} - \Pi_h\mathbf{u}) \\ &\le \left(\left|L'(\mathbf{u}_h)\right|,\, |\mathbf{u} - \Pi_h\mathbf{u}|\right) \end{aligned}$$

where $(\cdot,\, \cdot)$ is an inner product. Here $|L'(\mathbf{u}_h)|$ contains no unknown quantities, and $|\mathbf{u} - \Pi_h\mathbf{u}|$ can be estimated by standard interpolation methods as

$$|\mathbf{u} - \Pi_h\mathbf{u}| \le C\left|h^2 D_{\mathbf{x}}^2\mathbf{u} + \tau^2\frac{\partial^2\mathbf{u}}{\partial t^2}\right| \approx C\left|h[D_{\mathbf{x}}\mathbf{u}_h] + \tau\left[\frac{\partial\mathbf{u}_h}{\partial t}\right]\right|.$$

Here C is some constant, h is the size of the elements (subregions) in the spatial discretization, τ is the length of the subintervals in the time discretization, $D_{\mathbf{x}}$ and $D_{\mathbf{x}}^2$ denotes derivatives with respect to $\mathbf{x}$ of first and second order, respectively, and $[\cdot]$ denotes "jumps" in the functions across the edges of the elements in space or nodes in time. This leaves us with no unknown terms, hence an a posteriori estimate. Moreover, since

the inner product can be computed in terms of its local contribution on each subregion as

$$\|\cdot\| = \sum_{\{K\}} \|(\cdot)|_K\|_K \,,$$

where $\{K\}$ is the collection of subregions and $\|\cdot\|_K$ is the norm on K, we can localize the error estimate as required for the adaptive algorithm.

For the estimate for the coefficient, we start by using convexity (3.6) and optimality (3.5) to get

$$\begin{aligned} \|\varepsilon - \varepsilon_h\|^2 &\leq C \left| F'_\alpha(\varepsilon_h;\, \varepsilon - \varepsilon_h) \right| \\ &= C \left| \frac{\partial L}{\partial \varepsilon}(\tilde{\mathbf{u}};\, \varepsilon - \varepsilon_h) \right| \\ &\leq C \left\| \frac{\partial L}{\partial \varepsilon}(\tilde{\mathbf{u}}) \right\| \|\varepsilon - \varepsilon_h\| \,, \end{aligned}$$

thus obtaining an estimate for $\|\varepsilon - \varepsilon_h\|$ in terms of $\left\|\frac{\partial L}{\partial \varepsilon}(\tilde{\mathbf{u}})\right\|$, where we use the notation $\tilde{\mathbf{u}} \coloneqq (\varepsilon_h,\, \mathbf{E}_{\varepsilon_h},\, \boldsymbol{\lambda}_{\varepsilon_h})$. Although $\tilde{\mathbf{u}}$ contains unknown exact solutions $\mathbf{E}_{\varepsilon_h}$ and $\boldsymbol{\lambda}_{\varepsilon_h}$ corresponding to the approximate coefficient ε_h, we can split

$$\left\| \frac{\partial L}{\partial \varepsilon}(\tilde{\mathbf{u}}) \right\| \leq \left\| \frac{\partial L}{\partial \varepsilon}(\tilde{\mathbf{u}}) - \frac{\partial L}{\partial \varepsilon}(\mathbf{u}_h) \right\| + \left\| \frac{\partial L}{\partial \varepsilon}(\mathbf{u}_h) \right\|$$

and estimate the first term via linearization and Galerkin orthogonality, to obtain an a posteriori estimate for $\|\varepsilon - \varepsilon_h\|$. An estimate for $F_\alpha(\varepsilon) - F_\alpha(\varepsilon_h)$ follows via linearization.

4. Summary of included papers

Papers I and II are of a theoretical nature and are concerned with a posteriori error estimation in the adaptive stage for the case when (1.10) is used to describe the electric field. The arguments used could easily be adapted also to the case where (1.11) is employed. In Paper I we focus on the differentiation of the Lagrangian and sketch the proof of the a posteriori error estimate for the Lagrangian when the model problem uses (1.10). In Paper II we obtain a posteriori error estimates, as briefly outlined in the previous section, for three quantities: the Lagrangian ($L(\varepsilon,\, \mathbf{E}_\varepsilon,\, \boldsymbol{\lambda}_\varepsilon) - L(\varepsilon_h,\, \mathbf{E}_h,\, \boldsymbol{\lambda}_h)$, here with a detailed proof), the Tikhonov functional ($F_\alpha(\varepsilon) - F_\alpha(\varepsilon_h)$), and the coefficient ($\varepsilon - \varepsilon_h$). We show that each of the three estimates depend strongly on a certain residual, essentially

a discrete analogue to F'_α at ε_h. This justifies the use of such an error estimate in Papers III and IV.

Papers III and IV are co-authored with Larisa Beilina, Nguyen Trung Thành, and Michael V. Klibanov. Both papers present results of the adaptive stage of Section 3, applied to experimental data which were gathered at a scattering facility at the University of North Carolina at Charlotte, USA. For results of the approximately globally convergent algorithm, see references within those papers.

In Paper III the experimental data were collected for scatterers placed in air. Dielectric, metallic, and heterogeneous (partly metallic and partly dielectric) scatterers were studied. Homogeneous scatterers were all correctly classified, while for heterogeneous scatterers only the metallic parts were detected. The reconstructions of shapes after adaptivity were improved compared to those given by the approximately globally convergent algorithm.

In Paper IV the scatterers were buried in dry sand. This makes the reconstruction procedure more challenging since the backscattered signals from the scatterers must be distinguished from the signals from the sand. For reference, the signal from dry sand without the presence of additional scatterers was used. Both dielectric and metallic scatterers were studied. In contrast to the case in Paper III, where all scatterers had a value of the dielectric permittivity strictly larger than the background (air), in Paper IV some scatterers had a higher value of ε than the surrounding sand (strong targets), while other scatterers had a value of ε lower than the sand (weak targets). In the latter case, accurate reconstructions were only obtained if the burial depth (that is, the distance from the buried scatterer to the surface of the sand) was not larger than $\sim$5 cm. This is not a severe restriction for applications, see Section 7 of Paper IV.

One notable result of Paper IV was that for one scatterer, *superresolution* was achieved. The scatterer consisted of two metallic prisms separated by 1 cm of sand. Since the wavelength of the signal was 4.5 cm, the diffraction limit was approximately 2.25 cm. Nevertheless, the metallic prisms were resolved as two separate objects.

5. Future work

As pointed out above, the arguments used in Paper II concerning the model (1.10) can easily be adapted to model (1.11) with analogous results. There is reason to believe that (1.10) and the discretization of Paper II

may produce better reconstructions than those of Papers III and IV, since they are more conforming to the regularity assumptions required by the theory. Numerical investigation of this issue and analysis of the possible gain in accuracy of reconstructions versus additional computational cost remains to be done.

In the studies of Papers III and IV, the regularization parameter α of the Tikhonov functional was selected by hand to obtain good reconstructions. Many numerical rules for automatic optimization of regularization parameters exist, but have not been tested for the problem we study. Since it is computationally expensive to find (an approximation of) the minimizer for F_α, requiring the solution of two partial differential equations for each evaluation of the gradient, iterative methods for selecting α as a part of the minimization procedure, see [2, 9], would be of particular interest.

The superresolution achieved for one pair of scatterers in the study of Paper IV has not yet been fully explained – though we make some remarks concerning possible causes for superresolution in the introduction to that paper.

In addition, several minor improvements are possible. For example, it would be necessary to include a (known) conductivity $\sigma = \sigma(\mathbf{x}) \not\equiv 0$ in order to treat the case of wet (hence conductive) sand, as opposed to the case of dry sand in Paper IV. A method for determination of an unknown conductivity in a manner similar to the method for permittivity described in Section 2, is suggested in [13].

References

[1] M. Asadzadeh and L. Beilina. A posteriori error analysis in a globally convergent numerical method for a hyperbolic coefficient inverse problem. *Inverse problems*, 26:115007, 2010.

[2] A.B. Bakushinsky, M.Yu. Kokurin, and A. Smirnova. *Iterative Methods for Ill-Posed Problems: An Introduction*. De Gruyter, Berlin, 2011.

[3] L. Beilina. Adaptive finite element method for a coefficient inverse problem for the Maxwell's system. *Appl. Anal.*, 90:1461–1479, 2011.

[4] L. Beilina and M.V. Klibanov. A globally convergent numerical method for a coefficient inverse problem. *SIAM J. Sci. Comput.*, 31(1):478–509, 2008.

[5] L. Beilina and M.V. Klibanov. *Approximate Global Convergence and Adaptivity for Coefficient Inverse Problems*. Springer, New York, 2012.

[6] L. Beilina and M.V. Klibanov. Globally strongly convex cost functional for a coefficient inverse problem. *Nonlinear Anal. Real World Appl.*, 22:272–288, 2015.

[7] L. Beilina, M.V. Klibanov, and M.Yu. Kokurin. Adaptivity with relaxation for ill-posed problems and global convergence for a coefficient inverse problem. *J. Math. Sci.*, 167:279–325, 2010.

[8] S.C. Brenner and L.R. Scott. *The Mathematical Theory of Finite Element Methods*, volume 15 of *Texts in Applied Mathematics*. Springer, New York, third edition, 2008.

[9] H.W. Engl, M. Hanke, and A. Neubauer. *Regularization of Inverse Problems*, volume 375 of *Mathematics and its Applications*. Kluwer Academic Publishers Group, Dordrecht, 1996.

[10] K. Eriksson, D. Estep, P. Hansbo, and C. Johnson. *Computational Differential Equations*. Studentlitteratur, Lund, 1996.

[11] M.V. Klibanov and A. Timonov. A unified framework for constructing globally convergent algorithms for multidimensional coefficient inverse problems. *Appl. Anal.*, 83(9):933–955, 2004.

[12] S. Larsson and V. Thomée. *Partial Differential Equations with Numerical Methods*, volume 45 of *Texts in Applied Mathematics*. Springer-Verlag, Berlin, 2009. Paperback reprint of the 2003 edition.

[13] J.B. Malmberg and L. Beilina. *Approximate globally convergent algorithm with applications in electrical prospecting*, volume 52 of *Springer Proceedings in Mathematics and Statistics*, pages 29–40. Springer, 2013.

[14] P. Monk. *Finite Element Methods for Maxwell's Equations*. Clarendon, Oxford, 2003.

[15] K.D. Poulsen and D.R. Lynch. Elimination of vector parasites in finite element Maxwell solutions. *IEEE Trans. Microwave Theory Techniques*, 39:395–404, 1991.

[16] M.I. Skolnik. 36 - radar. In Wendy M. MiddletonMac E. Valkenburg, editor, *Reference Data for Engineers (Ninth Edition)*, pages 1 – 22. Newnes, Woburn, ninth edition, 2002.

[17] A.N. Tikhonov, A.V. Goncharsky, V.V. Stepanov, and A.G. Yagola. *Numerical Methods for the Solution of Ill-Posed Problems*. Kluwer Academic Publishers, Dordrecht, 1995.

Part 2

Papers

Paper I

Reprinted from John Bondestam Malmberg, *A posteriori error estimate in the Lagrangian setting for an inverse problem based on a new formulation of Maxwell's system*, volume 120 of *Springer Proceedings in Mathematics and Statistics*, pages 42–53, Springer, 2015, with permission from the publisher.

A posteriori error estimate in the Lagrangian setting for an inverse problem based on a new formulation of Maxwell's system

John Bondestam Malmberg[1]

Abstract. In this paper we consider an inverse problem of determination of a dielectric permittivity function from a backscattered electromagnetic wave. The inverse problem is formulated as an optimal control problem for a certain partial differential equation derived from Maxwell's system. We study a solution method based on finite element approximation and provide an a posteriori error estimate for the use in an adaptive algorithm.

1. Introduction

In recent publications [7, 10, 11] it was demonstrated how to reconstruct the dielectric permittivity function $\varepsilon(x)$, $x \in \Omega \subset \mathbb{R}^3$, for a heterogeneous medium, using experimental measurements of a single backscattered electromagnetic wave. In [5, 7, 10, 11], the authors refer to the technique as an approximately globally convergent method, since it does not rely on any strong restrictions on the a priori information available on ε. This approach yields an approximate reconstruction which we will denote by ε_0.

Here, we consider a second processing step where ε_0 is used as an initial approximation for a classical Tikhonov regularization procedure. The underlying partial differential equation relating the permittivity ε to the electric field E as well as the permittivity function itself is approximated using adaptive finite elements.

To formulate a mathematical framework we introduce some notation. We assume that Ω is a bounded domain with piecewise smooth boundary Γ. Let $T > 0$ be a fixed, sufficiently large time and denote $\Omega \times (0,\, T) =: Q_T$ and $\Gamma \times (0,\, T) =: S_T$. For a set $X \subset \mathbb{R}^n$ we introduce the following inner product and norms: $\langle \cdot,\, \cdot \rangle_X = \langle \cdot,\, \cdot \rangle_{L_2(X)}$, $\|\cdot\|_X = \|\cdot\|_{L_2(X)}$, and $\|\cdot\|_{X,\,m} = \|\cdot\|_{H^m(X)}$. In this setting, the problem we consider is the

[1]Department of Mathematical Sciences, Chalmers University of Technology and University of Gothenburg, SE-412 96 Gothenburg, Sweden. E-mail: john.bondestam.malmberg@chalmers.se

minimization of the Tikhonov functional

$$\Phi(\varepsilon) := \Phi(\varepsilon,\, E(\varepsilon)) := \frac{1}{2}\left\|(E(\varepsilon)-F)z_\delta^{1/2}\right\|_{S_T}^2 + \frac{\alpha}{2}\left\|\varepsilon-\varepsilon_0\right\|_\Omega^2, \tag{1.1}$$

where $\alpha > 0$ is a regularization parameter and $F \in L_2(S_T)$ is the observed data obtained from measurements and, in the case of incomplete measurements, simulations. To ensure data compatibility for the adjoint problem to be presented in Section 3, we introduce in (1.1) the smooth function $z_\delta = z_\delta(t)$, that drops from a constant level of 1 to 0 inside the small interval $(T-\delta,\, T-\delta/2)$.

We assume that ε belongs to the set $U^\varepsilon \subset V^\varepsilon := H^3(\Omega)$ of admissible parameters, with

$$U^\varepsilon := \{v \in C(\mathbb{R}^3) : v|_\Omega \in H^3(\Omega),\ 1 \le v(x) \le M\ \forall x \in \Omega,\ v \equiv 1 \text{ in } \mathbb{R}^3 \setminus \Omega\} \tag{1.2}$$

for some upper bound $M > 1$. By the Sobolev embedding, this gives in particular $\varepsilon \in C^1(\bar{\Omega})$ which will be required for technical reasons (see Section 3).

In (1.1), $E(\varepsilon)$ denotes the solution of the following system of equations, the first of which will be derived from Maxwell's equations in Section 2,

$$\begin{aligned} &\varepsilon\partial_t^2 E - \Delta E - \nabla\left(\frac{1}{\varepsilon}\nabla\varepsilon\cdot E\right) = 0 && \text{in } Q_T,\\ &\partial_\nu E = P && \text{on } S_T,\\ &E(\cdot,\,0) = \partial_t E(\cdot,\,0) = 0 && \text{in } \Omega. \end{aligned} \tag{1.3}$$

Here, ∂_ν denotes the directional derivative along the outward normal ν, and the boundary data $P \in L_2(S_T)$ describes an incident plane wave. Since ε is known in $\mathbb{R}^3 \setminus \Omega$, P can be obtained from data F of (1.1) by computation in a sufficiently small neighborhood of Γ.

2. Derivation of the forward problem

Here we derive the forward problem for the electric field starting from the classical Maxwell's system (see for instance [9]).

Let Q_T be defined as above. Then we have Maxwell's equations over Q_T stating

$$\partial_t B + \nabla \times E = 0 \quad \text{in } Q_T, \tag{2.1}$$

$$\partial_t D - \nabla \times H = 0 \quad \text{in } Q_T, \tag{2.2}$$

$$\nabla \cdot B = \nabla \cdot D = 0 \quad \text{in } Q_T, \tag{2.3}$$

where B, D, H, and $E\colon Q_T \to \mathbb{R}^3$ are magnetic flux density, electric displacement, magnetic field, and electric field, respectively.

In addition to (2.1), (2.2), and (2.3), B, D, H and E also satisfy

$$B = \mu H \quad \text{and} \quad D = \varepsilon E, \tag{2.4}$$

where μ is the magnetic permeability and ε is the dielectric permittivity. We assume that μ is constant, scaled to unity, and that $\varepsilon \in U^\varepsilon$, with U^ε defined in (1.2).

We focus our study on the electric field E alone. To derive the equation for E, we eliminate B, D, and H from the above equations by using (2.4) in conjunction with the curl of (2.1) and the time derivative of (2.2), obtaining

$$\varepsilon \partial_t^2 E + \nabla \times (\nabla \times E) = 0, \quad \text{in } Q_T. \tag{2.5}$$

Having separated the dependence of the magnetic field, which we will not consider further, and the electric field, we are left with two conditions: equation (2.5), and the divergence free condition $\nabla \cdot (\varepsilon E) = 0$ from (2.3). For calculations we should take them both into account.

For this approach, various techniques are developed by several authors. One example is the edge element method of Nédélec (see for instance Chapter 8 of [12]) where the divergence free condition is incorporated into the numerical solution scheme. Another technique consists of inserting a penalty term $-\nabla(\nabla \cdot (\varepsilon E))$ on the left hand side of (2.5) (see [14, 15]). Here, we propose to include the divergence free condition directly in (2.5), without introducing additional terms.

To this end, we expand the second term in the left hand side of (2.5) as

$$\nabla \times (\nabla \times E) = -\Delta E + \nabla(\nabla \cdot E),$$

and then we use the following expansion of the divergence of the electric field:

$$\nabla \cdot E = \nabla \cdot \left(\frac{\varepsilon E}{\varepsilon} \right) = \frac{1}{\varepsilon} \nabla \cdot (\varepsilon E) - \frac{1}{\varepsilon} \nabla \varepsilon \cdot E = -\frac{1}{\varepsilon} \nabla \varepsilon \cdot E,$$

where the divergence free condition gives us the last equality. Combining these calculations with (2.5) and completing with boundary and initial conditions we obtain the system (1.3).

3. The Lagrangian formulation

With the forward problem as derived in the previous section, we here turn back to the inverse one. That is, we consider the minimization of the Tikhonov functional Φ defined in (1.1).

For this problem, following earlier works [1, 2, 4, 5], we introduce the Lagrangian corresponding to Φ where (1.3) is acting as a constraint,

$$L(\varepsilon,\, E,\, \lambda) \coloneqq \Phi(\varepsilon,\, E) + \left\langle \varepsilon\partial_t^2 E - \Delta E - \nabla\left(\tfrac{1}{\varepsilon}\nabla\varepsilon\cdot E\right),\, \lambda\right\rangle_{Q_T}. \tag{3.1}$$

When working with Maxwell's system, solutions are usually sought in spaces such as $H(\mathrm{curl}, \Omega)$ of square integrable fields with square integrable curl [14]. For our approach, using piecewise linear finite elements, we make instead the following assumptions (see [3]):

$$E \in V^E \coloneqq \{v \in [H^1(Q_T)]^3 : v(\cdot,\, 0) \equiv 0\},$$
$$\lambda \in V^\lambda \coloneqq \{v \in [H^1(Q_T)]^3 : v(\cdot,\, T) \equiv 0\}.$$

In addition, we write

$$u = (\varepsilon,\, E,\, \lambda) \in V \coloneqq V^\varepsilon \times V^E \times V^\lambda,$$

$$U \coloneqq U^\varepsilon \times V^E \times V^\lambda \subset V,$$

where U^ε was defined in (1.2) and $V^\varepsilon = H^3(\Omega)$ as above. This allows us to rewrite (3.1) on weak form as

$$\begin{aligned} L(u) = \Phi(\varepsilon,\, E) &- \langle \varepsilon\partial_t E,\, \partial_t\lambda\rangle_{Q_T} + \langle \nabla E,\, \nabla\lambda\rangle_{Q_T} \\ &+ \left\langle \tfrac{1}{\varepsilon}\nabla\varepsilon\cdot E,\, \nabla\cdot\lambda\right\rangle_{Q_T} - \langle P,\, \lambda\rangle_{S_T}, \end{aligned} \tag{3.2}$$

for every $u = (\varepsilon,\, E,\, \lambda) \in V$.

We can now find the minimizer of Φ over U^ε by finding a stationary point to the Lagrangian. That is, by solving the following more explicit problem:

(3.3) Find $u = (\varepsilon,\, E,\, \lambda) \in U$ such that $L'(u;\, \bar{u}) = 0$ for every $\bar{u} \in V$.

Here

$$L'(u;\, \bar{u}) = L'_\varepsilon(u;\, \bar{\varepsilon}) + L'_E(u;\, \bar{E}) + L'_\lambda(u;\, \bar{\lambda})$$

is the Fréchet derivative of L at the point u acting on $\bar{u}$, for which we will provide exact formulas in Proposition 1. But first we should make a remark concerning how to solve problem (3.3).

According to the theory of ill-posed problems, [16], the initial approximation ε_0 should belong to some sufficiently small neighborhood of the solution ε. The approximately globally convergent method of [5, 7, 10, 11] ensures this when the electric field E is described by the wave equation, and it was shown in [3] that the wave equation approximates Maxwell's system well for the type of problem we consider. Thus, we can assume that ε_0 obtained from the approximately globally convergent method is sufficiently close to the ideal solution for exact data. If the regularization parameter α is chosen appropriately, Lemma 2.1 and Theorem 3.1 of [6] then implies that ε_0 is close to ε and that the Tikhonov functional Φ is strongly convex in a neighborhood of ε_0. Hence it is reasonable to solve (3.3) with a gradient-based method, starting from ε_0.

With this remark made, we proceed with the formulas for the Fréchet derivative of the Lagrangian.

PROPOSITION 1. *Let $L(u) = L(\varepsilon, E, \lambda)$ be the Lagrangian defined in (3.2). Then its partial Fréchet derivatives at the point $u \in U$, acting on $\bar{\varepsilon} \in V^{\varepsilon}$, $\bar{E} \in V^{E}$ and $\bar{\lambda} \in V^{\lambda}$, respectively, are given by*

$$
\begin{aligned}
L'_{\varepsilon}(u;\, \bar{\varepsilon}) &= \alpha \left\langle \varepsilon - \varepsilon_0,\, \bar{\varepsilon} \right\rangle_{\Omega} - \left\langle \partial_t E \cdot \partial_t \lambda,\, \bar{\varepsilon} \right\rangle_{Q_T} + \left\langle (\nabla \cdot \lambda) E,\, \nabla \left(\tfrac{\bar{\varepsilon}}{\varepsilon} \right) \right\rangle_{Q_T}, \\
L'_{E}(u;\, \bar{E}) &= \left\langle (E - F) z_{\delta},\, \bar{E} \right\rangle_{S_T} - \left\langle \varepsilon \partial_t \lambda,\, \partial_t \bar{E} \right\rangle_{Q_T} \\
&\quad + \left\langle \nabla \lambda,\, \nabla \bar{E} \right\rangle_{Q_T} + \left\langle \tfrac{1}{\varepsilon} (\nabla \cdot \lambda) \nabla \varepsilon,\, \bar{E} \right\rangle_{Q_T}, \\
L'_{\lambda}(u;\, \bar{\lambda}) &= - \left\langle \varepsilon \partial_t E,\, \partial_t \bar{\lambda} \right\rangle_{Q_T} + \left\langle \nabla E,\, \nabla \bar{\lambda} \right\rangle_{Q_T} \\
&\quad + \left\langle \tfrac{1}{\varepsilon} \nabla \varepsilon \cdot E,\, \nabla \cdot \bar{\lambda} \right\rangle_{Q_T} - \left\langle P,\, \bar{\lambda} \right\rangle_{S_T}.
\end{aligned}
$$

PROOF. We should show that for every $u \in U$, and for $\eta = \varepsilon$, E, and λ, $L'_{\eta}(u;\, \cdot)$ defines a bounded linear functional such that for $\theta \in V^{\eta}$

$$
\lim_{\theta \to 0} \frac{d_{\eta}(\theta)}{\|\theta\|_{V^{\eta}}} \coloneqq \lim_{\theta \to 0} \frac{\left| L(u + \theta) - L(u) - L'_{\eta}(u;\, \theta) \right|}{\|\theta\|_{V^{\eta}}} = 0, \tag{3.4}
$$

with $\|\cdot\|_{V^{\eta}} = \|\cdot\|_{\Omega,\,3}$ if $\eta = \varepsilon$ and $\|\cdot\|_{V^{\eta}} = \|\cdot\|_{Q_T,\,1}$ if $\eta = E$ or λ.

It is trivial to see that the linearity holds for each η. Turning then to the boundedness, starting with $\eta = \varepsilon$, we easily obtain the estimate

$$\begin{aligned}\left|L'_\varepsilon(u;\,\bar\varepsilon)\right| &\le \alpha\,\|\varepsilon-\varepsilon_0\|_\Omega\,\|\bar\varepsilon\|_\Omega + \|\partial_t E\|_{Q_T}\,\|\partial_t\lambda\|_{Q_T}\,\|\bar\varepsilon\|_{C(\bar\Omega)}\\ &\quad + \|\nabla\cdot\lambda\|_{Q_T}\,\|E\|_{Q_T}\left\|\nabla\left(\tfrac{\bar\varepsilon}{\varepsilon}\right)\right\|_{C(\bar\Omega)}.\end{aligned}\tag{3.5}$$

From the Sobolev inequality we get

$$\|v\|_{C^n(\bar\Omega)} \le C\,\|v\|_{\Omega,\,2+n}\,,\quad v\in H^{2+n}(\Omega),\ n\in\mathbb{N}.\tag{3.6}$$

Here and throughout this proof, C denotes various positive constants which do not depend on either $\bar\varepsilon$, $\bar E$, $\bar\lambda$ or θ.

Now (3.5) and (3.6) together with the boundedness of $\varepsilon\in U^\varepsilon$ yields

$$\begin{aligned}\left|L'_\varepsilon(u;\,\bar\varepsilon)\right| &\le C\big(\,\|\varepsilon-\varepsilon_0\|_\Omega + \|\partial_t E\|_{Q_T}\,\|\partial_t\lambda\|_{Q_T}\\ &\quad + (1+\|\nabla\varepsilon\|_{C(\bar\Omega)})\,\|\nabla\cdot\lambda\|_{Q_T}\,\|E\|_{Q_T}\,\big)\,\|\bar\varepsilon\|_{\Omega,\,3}\,,\end{aligned}$$

where all the norms inside the parentheses are finite. Thus $L'_\varepsilon(u;\,\cdot)$ is bounded as required.

Similarly, for $\eta = E$, we have the estimate

$$\begin{aligned}\left|L'_E(u;\,\bar E)\right| &\le \|E-F\|_{S_T}\,\|z_\delta\|_{C([0,\,T])}\left\|\bar E\right\|_{S_T}\\ &\quad + \|\varepsilon\|_{C(\bar\Omega)}\,\|\partial_t\lambda\|_{Q_T}\left\|\partial_t\bar E\right\|_{Q_T} + \|\nabla\lambda\|_{Q_T}\left\|\nabla\bar E\right\|_{Q_T}\\ &\quad + \left\|\tfrac{1}{\varepsilon}\right\|_{C(\bar\Omega)}\,\|\nabla\varepsilon\|_{C(\bar\Omega)}\,\|\nabla\cdot\lambda\|_{Q_T}\cdot\left\|\bar E\right\|_{Q_T}.\end{aligned}$$

We can now use the trace inequality

$$\|v\|_{S_T} \le C\,\|v\|_{Q_T,\,1}\,,\quad v\in H^1(Q_T),\tag{3.7}$$

and the boundedness of ε and z_δ to obtain

$$\begin{aligned}\left|L'_E(u;\,\bar E)\right| &\le C\big(\,\|E\|_{Q_T,\,1} + \|F\|_{S_T} + M\,\|\partial_t\lambda\|_{Q_T}\\ &\quad + \|\nabla\lambda\|_{Q_T} + \|\nabla\varepsilon\|_{C(\bar\Omega)}\,\|\nabla\cdot\lambda\|_{Q_T}\,\big)\,\left\|\bar E\right\|_{Q_T,\,1}.\end{aligned}$$

Again, all norms inside the parentheses are finite and so $L'_E(u;\,\cdot)$ is bounded.

For $\eta = \lambda$ we use (3.7) and obtain boundedness from the estimate

$$\begin{aligned}\left|L'_\lambda(u;\,\bar\lambda)\right| &\le \|\varepsilon\|_{C(\bar\Omega)}\,\|\partial_t E\|_{Q_T}\left\|\partial_t\bar\lambda\right\|_{Q_T} + \|\nabla E\|_{Q_T}\left\|\nabla\bar\lambda\right\|_{Q_T}\\ &\quad + \left\|\tfrac{1}{\varepsilon}\right\|_{C(\bar\Omega)}\,\|\nabla\varepsilon\|_{C(\bar\Omega)}\,\|E\|_{Q_T}\left\|\nabla\cdot\bar\lambda\right\|_{Q_T} + \|P\|_{S_T}\left\|\bar\lambda\right\|_{S_T}\\ &\le \big(M\,\|\partial_t E\|_{Q_T} + \|\nabla E\|_{Q_T}\\ &\quad + \|\nabla\varepsilon\|_{C(\bar\Omega)}\,\|E\|_{Q_T} + \|P\|_{S_T}\,\big)\,\left\|\bar\lambda\right\|_{Q_T,\,1}.\end{aligned}$$

It remains to show that (3.4) holds for $\eta = \varepsilon$, E, and λ. For $\eta = \varepsilon$ we get the estimate

$$\begin{aligned} d_\varepsilon(\theta) &= \left| \frac{\alpha}{2} \|\theta\|_\Omega^2 + \left\langle \tfrac{\theta}{\varepsilon+\theta} \nabla \left(\tfrac{\theta}{\varepsilon}\right), (\nabla \cdot \lambda) E \right\rangle_{Q_T} \right| \\ &\le \frac{\alpha}{2} \|\theta\|_\Omega^2 + \left\| \tfrac{1}{\varepsilon+\theta} \right\|_{C(\bar\Omega)} \|\theta\|_{C(\bar\Omega)} \left\| \nabla \left(\tfrac{\theta}{\varepsilon}\right) \right\|_{C(\bar\Omega)} \|\nabla \cdot \lambda\|_{Q_T} \|E\|_{Q_T} \\ &\le \left(\frac{\alpha}{2} + \left\| \tfrac{1}{\varepsilon+\theta} \right\|_{C(\bar\Omega)} \|\nabla \cdot \lambda\|_{Q_T} \|E\|_{Q_T} (1 + \|\nabla \varepsilon\|_{C(\bar\Omega)}) \right) \|\theta\|_{\Omega,3}^2 , \end{aligned}$$

where in the last line we have used (3.6). Since $\left\| \tfrac{1}{\varepsilon+\theta} \right\|_{C(\bar\Omega)} \to \left\| \tfrac{1}{\varepsilon} \right\|_{C(\bar\Omega)} = 1$ as $\theta \to 0$ in $H^3(\Omega)$, this is sufficient to prove that (3.4) holds for $\eta = \varepsilon$.

Next we consider (3.4) in the case $\eta = E$, where using (3.7) we obtain

$$\frac{d_E(\theta)}{\|\theta\|_{Q_T,1}} = \frac{\|z_\delta\|_{C([0,T])} \|\theta\|_{S_T}^2}{2 \|\theta\|_{Q_T,1}} \le C \|\theta\|_{Q_T,1} \to 0$$

as $\theta \to 0$. Finally, for $\eta = \lambda$ we have $d_\lambda(\theta) = 0$ for every $\theta \in V^\lambda$, and thus the proof is complete. □

For the solution $u = (\varepsilon, E, \lambda)$ of (3.3), we have in particular $L'_\lambda(u, \bar\lambda) = 0$ for each $\bar\lambda \in V^\lambda$ and $L'_E(u; \bar E) = 0$ for each $\bar E \in V^E$. It follows from Proposition 1 that this implies that E satisfies a weak formulation of the problem (1.3) and that λ satisfies a weak formulation of the corresponding adjoint problem:

$$\begin{aligned} &\varepsilon \partial_t^2 \lambda - \Delta \lambda + \frac{\nabla \cdot \lambda}{\varepsilon} \nabla \varepsilon = 0 && \text{in } Q_T, \\ &\partial_\nu \lambda = -(E - F) z_\delta && \text{on } S_T, \\ &\lambda(\cdot, T) = \partial_t \lambda(\cdot, T) = 0 && \text{in } \Omega. \end{aligned}$$

We conclude this section by stating a finite element formulation corresponding to the problem (3.3). For this purpose, similarly with [8], we introduce a triangulation $K_h = \{K\}$ of $\bar\Omega$ and a partition $I_\tau = \{(t_{n-1}, t_n]\}_{n=1}^{N_\tau}$, $0 = t_0 < t_1 < \ldots < t_{N_\tau} = T$, of $[0, T]$. With K_h we associate a mesh function h such that $h(x) = \operatorname{diam}(K)$ for $x \in K \in K_h$ and with I_τ we associate the mesh function τ such that $\tau(t) = t_n - t_{n-1}$

for $t \in (t_{n-1}, t_n]$. On these partitions we define the following finite dimensional spaces and subsets thereof:

$$V_h^\varepsilon \coloneqq \{v \in H^1(\Omega) : v|_K \in P^1(K) \,\forall\, K \in K_h\},$$
$$U_h^\varepsilon \coloneqq \{v \in V_h^\varepsilon : 1 \le v(x) \le M \;\forall x \in \bar{\Omega}, v(x) = 1 \;\forall x \in \partial\Omega\},$$
$$V_h^E \coloneqq \{v \in V^E : v|_{K\times I_n} \in [P^1(K)]^3 \times P^1(I_n)] \,\forall\, K \in K_h \;\forall I_n \in I_\tau\},$$
$$V_h^\lambda \coloneqq \{v \in V^\lambda : v|_{K\times I_n} \in [P^1(K)]^3 \times P^1(I_n) \,\forall\, K \in K_h \;\forall I_n \in I_\tau\},$$
$$V_h \coloneqq V_h^\varepsilon \times V_h^E \times V_h^\lambda,$$
$$U_h \coloneqq U_h^\varepsilon \times V_h^E \times V_h^\lambda.$$

Here $P^1(X)$ is the space of polynomials of degree no greater than 1 over X.

The finite dimensional formulation is now:

(3.8)

Find $u_h = (\varepsilon_h, E_h, \lambda_h) \in U_h$ such that $L'(u_h; \bar{u}) = 0$ for every $\bar{u} \in V_h$.

We note that in this finite dimensional problem, we seek $\varepsilon_h \in U_h^\varepsilon \subset V_h^\varepsilon$, a space of piecewise linear functions, while we originally assume that $\varepsilon \in U \subset H^3(\Omega)$ is in particular continuous and once continuously differentiable. Hence V_h^ε is not a subspace of V^ε. In spite of this discrepancy in regularity between the two formulations we will keep the formulation (3.8), as numerical experiments have shown good results in analogous situations, see [2, 4, 5].

4. A posteriori error estimate

In order to use adaptive techniques to efficiently refine the partition K_h (and if necessary for the Courant-Friedrichs-Lewy condition, also I_τ) we need to estimate the local contributions to the global error resulting from the finite dimensional approximation described at the end of the previous section. To this end, we here derive an a posteriori error estimate for the difference between u and u_h in the Lagrangian setting.

We start by introducing some additional notation. For $\eta = \varepsilon$, E, and λ, with $v \in V^\eta$ (or V), let $I_h v \in V_h^\eta$ (or V_h) denote the nodal interpolant of v. We then define the interpolation residual r_h by

$$r_h v \coloneqq v - I_h v.$$

Given meshes K_h and I_τ, we let $\{v\}_x$ denote the jump of v across the edges of the elements of K_h and $\{v\}_t$ denote the jump of v in time at

the endpoints of the intervals of I_τ. Moreover, we introduce $[v]_x$ as the piecewise constant function on K_h taking the average of $\{v\}_x$ over the edges ∂K as value on $K \in K_h$, as well as $[v]_t$ defined analogously to $[v]_x$. Finally, for $K \in K_h$ we denote by K_T the set $K \times (0, T)$ and by k_T the set $(\partial K \setminus \Gamma) \times (0, T)$.

Using this notation we can give an error representation formula and a corresponding estimate as follows:

PROPOSITION 2. *Let $u \in U$ be the solution to (3.3) and $u_h \in U_h$ be the solution to (3.8) on meshes K_h and I_τ. Then the error $e_{\mathrm{L}} := L(u) - L(u_h)$ in the Lagrangian setting can be expressed as*

$$\begin{aligned} e_{\mathrm{L}} &= L'(u_h;\, r_h u) + o(\|u - u_h\|_V) \\ &= L'_\varepsilon(u_h;\, r_h\varepsilon) + L'_E(u_h;\, r_h E) + L'_\lambda(u_h;\, r_h\lambda) + o(\|u - u_h\|_V), \end{aligned} \tag{4.1}$$

where $\|\cdot\|_V$ denotes the norm on $V = V^\varepsilon \times V^E \times V^\lambda$ and

$$\begin{aligned} L'_\varepsilon(u_h;\, r_h\varepsilon) = \alpha \langle \varepsilon_h - \varepsilon_0,\, r_h\varepsilon\rangle_\Omega &- \langle \partial_t E_h \cdot \partial_t \lambda_h,\, r_h\varepsilon\rangle_{Q_T} \\ &- \left\langle \tfrac{1}{\varepsilon}(\nabla \cdot E_h)(\nabla \cdot \lambda_h),\, r_h\varepsilon \right\rangle_{Q_T} \\ &+ \frac{1}{2} \sum_{K \in K_h} \left\langle \tfrac{1}{\varepsilon_h} \{(\nabla \cdot \lambda_h)\nu\}_x \cdot E_h,\, r_h\varepsilon \right\rangle_{k_T}, \end{aligned} \tag{4.2}$$

$$\begin{aligned} L'_E(u_h;\, r_h E) = &\\ &- \langle \lambda_h - (E_h - F) z_\delta,\, r_h E\rangle_{S_T} - \sum_{n=1}^{N_\tau - 1} \langle \varepsilon_h \{\partial_t \lambda_h\}_t,\, r_h E\rangle_\Omega \big|_{t=t_n} \\ &+ \frac{1}{2} \sum_{K \in K_h} \langle \{\partial_\nu \lambda_h\}_x,\, r_h E\rangle_{k_T} + \left\langle \tfrac{1}{\varepsilon_h}(\nabla \cdot \lambda_h)\nabla\varepsilon_h,\, r_h E \right\rangle_{Q_T}, \end{aligned} \tag{4.3}$$

$$\begin{aligned} L'_\lambda(u_h;\, r_h\lambda) = &\\ &- \sum_{n=1}^{N_\tau - 1} \langle \varepsilon_h \{\partial_t E_h\}_t,\, r_h\lambda\rangle_\Omega \big|_{t=t_n} + \frac{1}{2} \sum_{K \in K_h} \langle \{\partial_\nu E_h\}_x,\, r_h\lambda\rangle_{k_T} \\ &- \left\langle \tfrac{1}{\varepsilon_h} \nabla\varepsilon_h \cdot \nabla E_h - \tfrac{1}{\varepsilon_h^2}(\nabla\varepsilon_h \cdot E_h)\nabla\varepsilon_h,\, r_h\lambda \right\rangle_{Q_T} \\ &+ \frac{1}{2} \sum_{K \in K_h} \left\langle \tfrac{1}{\varepsilon_h} \{(E_h \cdot \nabla\varepsilon_h)\nu\}_x,\, r_h\lambda \right\rangle_{k_T} + \langle E_h - P,\, r_h\lambda\rangle_{S_T} \end{aligned} \tag{4.4}$$

Moreover, we can approximately estimate[2] *the above terms as*

$$\left|L'_\varepsilon(u_h;\, r_h\varepsilon)\right| \lesssim \langle |R_\varepsilon|,\, h\,|[\partial_\nu \varepsilon_h]_x|\rangle_\Omega\,, \tag{4.5}$$

$$\begin{aligned}\left|L'_E(u_h;\, r_h E)\right| \lesssim{}& \langle |R_{\lambda,1}|,\, h\,|[\partial_\nu E_h]_x| + \tau\,|[\partial_t E_h]_t|\rangle_{Q_T} \\ &+ \langle |R_{\lambda,2}|,\, h\,|[\partial_\nu E_h]_x| + \tau\,|[\partial_t E_h]_t|\rangle_{S_T}\,,\end{aligned} \tag{4.6}$$

$$\begin{aligned}\left|L'_\lambda(u_h;\, r_h\lambda)\right| \lesssim{}& \langle |R_{E,1}|,\, h\,|[\partial_\nu \lambda_h]_x| + \tau\,|[\partial_t \lambda_h]_t|\rangle_{Q_T} \\ &+ \langle |R_{E,2}|,\, h\,|[\partial_\nu \lambda_h]_x| + \tau\,|[\partial_t \lambda_h]_t|\rangle_{S_T}\,,\end{aligned} \tag{4.7}$$

where

$$\begin{aligned}R_\varepsilon &= \alpha(\varepsilon_h - \varepsilon_0) - \int_0^T \partial_t E_h \cdot \partial_t \lambda_h \,\mathrm{d}t - \frac{1}{\varepsilon_h}\int_0^T (\nabla\cdot E_h)(\nabla\cdot\lambda_h)\,\mathrm{d}t \\ &\quad + \frac{1}{\varepsilon_h}\int_0^T \frac{[(\nabla\cdot\lambda_h)(\nu\cdot E_h)]_x}{h}\,\mathrm{d}t, \\ R_{\lambda,1} &= -\varepsilon_h \frac{[\partial_t\lambda_h]_t}{\tau} + \frac{1}{2}\frac{[\partial_\nu\lambda_h]_x}{h} + \frac{\nabla\cdot\lambda_h}{\varepsilon_h}\nabla\varepsilon_h, \\ R_{\lambda,2} &= \partial_\nu\lambda_h + (E_h - F)z_\delta, \\ R_{E,1} &= -\varepsilon_h\frac{[\partial_t E_h]_t}{\tau} + \frac{1}{2}\frac{[\partial_\nu E_h]_x}{h} + \frac{\nabla\varepsilon_h\cdot E_h}{\varepsilon_h^2}\nabla\varepsilon_h - \frac{\nabla\varepsilon_h\cdot\nabla E_h}{\varepsilon_h} \\ &\quad + \frac{1}{2\varepsilon_h}\frac{[(\nabla\varepsilon_h\cdot E_h)\nu]_x}{h}, \\ R_{E,2} &= \partial_\nu E_h - P.\end{aligned}$$

For the sake of brevity, the amount of detail in the following proof has been kept to a minimum. Full details will be provided in a forthcoming paper.

Proof. From the definition and linearity of the Fréchet derivative we get

$$\begin{aligned}e_{\mathrm{L}} &= L(u) - L(u_h) \\ &= L(u_h) + L'(u_h;\, u - u_h) + o(\|u - u_h\|_V) - L(u_h) \\ &= L'(u_h;\, r_h u) + L'(u_h;\, I_h u - u_h) + o(\|u - u_h\|_V),\end{aligned}$$

[2]Throughout the remaining part of the text we will use '$\lesssim$' to indicate approximate estimation in the following sense: $a \lesssim b$ if and only if there exists a constant $C > 0$ and some $b^* \approx b$ such that $a \le Cb^*$.

where in the last line we have used the split $u - u_h = r_h u + (I_h u - u_h)$. The term $L'(u_h;\, I_h u - u_h)$ vanishes in view of (3.8) because $I_h u - u_h \in V_h$, which gives the first equality in (4.1). The second equality in (4.1) follows immediately.

To obtain (4.2), (4.3) and (4.4) we use the Proposition 1 to express the Fréchet derivatives of L, integrating by parts in time or space to lift derivatives from the interpolation residual when applicable. Thus, for $L'_\varepsilon(u_h;\, r_h u)$ we perform the following calculation:

$$
\begin{aligned}
&\Big\langle (\nabla\cdot\lambda_h)E_h,\, \nabla(\tfrac{r_h\varepsilon}{\varepsilon_h})\Big\rangle_{Q_T} = \sum_{K\in K_h}\Big\langle (\nabla\cdot\lambda_h)E_h,\, \nabla(\tfrac{r_h\varepsilon}{\varepsilon_h})\Big\rangle_{K_T}\\
&\quad= \sum_{K\in K_h}\Big(-\Big\langle \nabla\cdot\big((\nabla\cdot\lambda_h)E_h\big),\, \tfrac{r_h\varepsilon}{\varepsilon_h}\Big\rangle_{K_T} + \Big\langle \nu\cdot\big((\nabla\cdot\lambda_h)E_h\big),\, \tfrac{r_h\varepsilon}{\varepsilon_h}\Big\rangle_{\partial K\times(0,\,T)}\Big)\\
&\quad= -\sum_{K\in K_h}\Big\langle \tfrac{1}{\varepsilon_h}\big(\nabla(\nabla\cdot\lambda_h)\big)E_h,\, r_h\varepsilon\Big\rangle_{K_T} - \sum_{K\in K_h}\Big\langle \tfrac{1}{\varepsilon_h}(\nabla\cdot\lambda_h)(\nabla\cdot E_h),\, r_h\varepsilon\Big\rangle_{K_T}\\
&\qquad+ \sum_{K\in K_h}\Big\langle \tfrac{1}{\varepsilon_h}(\nabla\cdot\lambda_h)(\nu\cdot E_h),\, r_h\varepsilon\Big\rangle_{k_T} + \Big\langle \tfrac{1}{\varepsilon_h}(\nabla\cdot\lambda_h)(\nu\cdot E_h),\, r_h\varepsilon\Big\rangle_{S_T}\\
&\quad= -\Big\langle \tfrac{1}{\varepsilon_h}(\nabla\cdot E_h)(\nabla\cdot\lambda_h),\, r_h\varepsilon\Big\rangle_{Q_T} + \frac{1}{2}\sum_{K\in K_h}\Big\langle \tfrac{1}{\varepsilon_h}\{(\nabla\cdot\lambda_h)(\nu\cdot E_h)\}_x,\, r_h\varepsilon\Big\rangle_{k_T},
\end{aligned}
$$

where we have used the facts that second derivatives of λ_h are identically zero inside the elements $K \in K_h$, and that $\varepsilon \equiv 1$ on Γ so that $r_h\varepsilon \equiv 0$ on Γ. The factor $\frac{1}{2}$ appears as every jump is counted exactly twice in the sum over all elements $K \in K_h$. This yields (4.2).

For (4.3), we have

$$
\begin{aligned}
-\langle \varepsilon_h\partial_t\lambda_h,\, \partial_t r_h E\rangle_{Q_T} &= \sum_{n=1}^{N_\tau}\int_{t_{n-1}}^{t_n}\big\langle \varepsilon_h\partial_t^2\lambda_h,\, r_h E\big\rangle_\Omega\,\mathrm{d}t\\
&\quad- \sum_{n=1}^{N_\tau-1}\langle \varepsilon_h\{\partial_t\lambda_h\}_t,\, r_h E\rangle_\Omega|_{t=t_n},
\end{aligned}
$$

where the first sum vanishes since second derivatives of the piecewise linear function λ_h are identically zero inside elements of I_τ.

Now calculations of the above two types yield the remaining part of (4.3) as well as (4.4).

To derive the approximate estimates (4.5), (4.6) and (4.7), we use two main principles. First we approximate integrals over boundaries by

integrals over elements (see for instance [8]) using the formulas

$$\int_{\partial K} f(x)\,\mathrm{d}s \approx \frac{1}{h_K}\int_K f(x)\,\mathrm{d}x, \quad \text{and} \quad f(t_n) \approx \frac{1}{t_n - t_{n-1}}\int_{t_{n-1}}^{t_n} f(t)\,\mathrm{d}t,$$

thus after some elementary manipulations obtaining

$$\begin{aligned} L'_\varepsilon(u_h;\, r_h\varepsilon) &\approx \langle R_\varepsilon,\, r_h\varepsilon\rangle_\Omega\,, \\ L'_E(u_h;\, r_h E) &\approx \langle R_{\lambda,1},\, r_h E\rangle_{Q_T} + \langle R_{\lambda,2},\, r_h E\rangle_{S_T}\,, \\ L'_\lambda(u_h;\, r_h\lambda) &\approx \langle R_{E,1},\, r_h\lambda\rangle_{Q_T} + \langle R_{E,2},\, r_h\lambda\rangle_{S_T}\,. \end{aligned}$$

Then we apply the following interpolation error estimates (see [13]):

$$|r_h\varepsilon| \le c_{\mathrm{i}} h^2 \left|D^2\varepsilon\right| \approx c_{\mathrm{i}} h\,|[\partial_\nu \varepsilon_h]_x| \implies |r_h\varepsilon| \lesssim h\,|[\partial_\nu\varepsilon_h]_x|\,,$$

for some interpolation constant c_{i} and with D^2 denoting derivatives of second order, and analogous estimates

$$|r_h\eta| \lesssim h\,|[\partial_\nu\eta_h]_x| + \tau\,|[\partial_t\eta_h]|\,, \quad \eta = E,\,\lambda.$$

This yields (4.5), (4.6) and (4.7). □

5. Conclusions

In Proposition 2 we have provided an a posteriori error estimate for a finite element approximation procedure for the inverse problem described in Section 1. The estimate contains three terms estimating $|L'_\varepsilon(u_h;\, r_h\varepsilon)|$, $|L'_E(u_h;\, r_h E)|$, and $|L'_\lambda(u_h;\, r_h\lambda)|$, as well as some higher order (and, we postulate, usually small) term $o(\|u - u_h\|_V)$.

The terms $|L'_E(u_h;\, r_h E)|$ and $|L'_\lambda(u_h;\, r_h\lambda)|$ correspond essentially to the accuracy of the finite element approximations E_h and λ_h the true weak solutions to the forward and adjoint problems, respectively, with $\varepsilon = \varepsilon_h$. Thus, if these approximations can be expected to be relatively accurate, we can focus on the term $|L'_\varepsilon(u_h;\, r_h\varepsilon)|$. This, by Proposition 2, corresponds to taking the residual R_ε as the indicator of the local contribution to the global error. Hence, refining meshes where the value of R_ε is close to its maximum will provide an efficient way of obtaining desired accuracy.

The error estimate we have given here is in the Lagrangian setting, and the Lagrangian was initially introduced as a tool for minimizing the Tikhonov functional Φ. Thus it is also of interest to estimate the error in the Tikhonov functional setting, that is, given ε and ε_h as above, to estimate $|\Phi(\varepsilon) - \Phi(\varepsilon_h)|$.

Finally, we note that the errors in the Tikhonov functional setting as well as in the Lagrangian both are of secondary importance in comparison to the error in the dielectric permittivity function itself, $\varepsilon - \varepsilon_h$. Thus, ultimately, we should provide an estimate for that error. Such an estimate, as well as an estimate for the error in the Tikhonov functional setting, as discussed above, will be the subject of forthcoming papers.

Acknowledgement

The author would like to express his gratitude to his supervisor Larisa Beilina for many good suggestions and advice, and to Mohammad Asadzadeh for many improved formulations.

This research was supported by the Swedish Research Council and by the Swedish Institute, Visby Program.

References

[1] Becker, R., Kapp, H., Rannacher, R.: Adaptive Finite Element Methods for Optimal Control of Partial Differential Equations: Basic Concept. SIAM J. Control Optim. **39** (2000)

[2] Beilina, L.: Adaptive hybrid finite element/difference methods: applications to inverse elastic scattering. J. Inverse Ill-posed probl. **11** (2003)

[3] Beilina, L.: Energy estimates and numerical verification of the stabilized Domain Decomposition Finite Element/Finite Difference approach for time-dependent Maxwell's system. Cent. Eur. J. Math. **11** (2013)

[4] Beilina, L., Johnson, C.: A posteriori error estimation in computational inverse scattering. Math. Models Methods Appl. Sci. **15** (2005)

[5] Beilina, L., Klibanov, M.V.: Approximate global convergence and adaptivity for Coefficient Inverse Problems. Springer, New York (2012)

[6] Beilina, L., Klibanov, M.V:, Kokurin, M.Yu.: Adaptivity with relaxation for ill-posed problems and global convergence for a coefficient inverse problem. J. Math. Sci. **3** (2010)

[7] Beilina, L., Thành, N.T., Klibanov, M.V., Fiddy, M.A.: Reconstruction from blind experimental data for an inverse problem for a hyperbolic equation. Inv. Probl. **30** (2014)

[8] Eriksson, K., Estep, D., Hansbo, P., Johnson, C.: Computational Differential Equations. Studentlitteratur, Lund (1996)

[9] Hammond, P., Sykulski, J.K.: Engineering Electromagnetism: Physical Processes and Computation. Oxford University Press, Oxford (1994)

[10] Klibanov, M.V., Fiddy, M.A., Beilina, L., Pantong, N., Schenk, J.: Picosecond scale experimental verification of a globally convergent numerical method for a coefficient inverse problem. Inv. Probl. **26**, 045003 (2010)

[11] Kuzhuget, A.V., Beilina, L., Klibanov, M.V., Sullivan, A., Nguyen, L., Fiddy, M.A.: Quantitative image recovery from measured blind backscattered data using a globally convergent inverse method. IEEE Trans. Geoscience and Remote Sensing. **51** (2013)

[12] Jin, J.: The finite element method in electromagnetics. John Wiley & Sons, New York (2002)

[13] Johnson, C., Szepessy, A.: Adaptive Finite Element Methods for Conservation Laws Based on a posteriori Error Estimates. Comm. Pure Appl. Math. **48** (1995)

[14] Monk, P.: Finite element methods for Maxwell's equations. Clarendon, Oxford (2003)

[15] Poulsen, K.D., Lynch, D.R.: Elimination of Vector Parasites in Finite Element Maxwell Solutions. IEEE Trans. Microwave Theory and Techniques. **39** (1991)

[16] Tikhonov, A.N., Goncharsky, A.V., Stepanov, V.V., Yagola, A.G.: Numerical Methods for the Solution of Ill-Posed Problems. Kluwer Academic Publishers, Dordrecht. (1995)

Paper II

John Bondestam Malmberg. *A posteriori error estimation in a finite element method for reconstruction of dielectric permittivity.* Preprint.

A posteriori error estimation in a finite element method for reconstruction of dielectric permittivity

John Bondestam Malmberg[1]

Abstract. We present a posteriori error estimates for finite element approximations in a minimization approach to a coefficient inverse problem. The problem is that of reconstructing the dielectric permittivity $\varepsilon = \varepsilon(\mathbf{x})$, $\mathbf{x} \in \Omega \subset \mathbb{R}^3$, from boundary measurements of the electric field. The electric field is related to the permittivity via Maxwell's equations. The reconstruction procedure is based on minimization of a Tikhonov functional where the permittivity, the electric field and a Lagrangian multiplier function are approximated by peicewise polynomials. Our main result is an estimate for the difference between the computed coefficient ε_h and the true minimizer ε, in terms of the computed functions.

1. Introduction

In this note we study an adaptive finite element method for the reconstruction of a dielectric permittivity function $\varepsilon = \varepsilon(\mathbf{x})$, $\mathbf{x} \in \Omega$, where $\Omega \subset \mathbb{R}^3$ is a bounded domain with (piecewise) smooth boundary Γ. This is a coefficient inverse problem (CIP) for Maxwell's equations, where the dielectric permittivity function ε, acting as the coefficient in the equations, characterizes an inhomogeneous, isotropic, non-magnetic, non-conductive medium in Ω. Possible applications include detection of explosives in airport security and detection of land mines.

The method studied is based on minimization of a Tikhonov functional, where the functions involved are approximated by piecewise polynomials. It is intended as a second stage in a two-stage numerical procedure for the reconstruction of a dielectric permittivity. On the first stage, described in [5, 6], a good initial approximation ε_0 of the dielectric permittivity function is obtained by a globally convergent method. This initial approximation is then refined on the second stage.

The version of the second stage considered here was introduced in [19]. Another version was studied theoretically and numerically in [3, 4,

[1]Department of Mathematical Sciences, Chalmers University of Technology and University of Gothenburg, SE-412 96 Gothenburg, Sweden. E-mail: john.bondestam.malmberg@chalmers.se

7–9]. There were two main reasons for introducing the new version of the second stage in [19]. The first reason was to handle a discrepancy between theory and implementation which was present in the previous version. This discrepancy was primarily due to the fact that the dielectric permittivity was approximated by a piecewise constant function, while the theory required higher regularity. In spite of that discrepancy, reasonable reconstructions were obtained, but it remained to be seen whether the new version of [19] could produce even more accurate reconstructions.

The second reason to introduce the version of [19] was to incorporate the divergence free condition for the electric displacement directly into the differential equation, without having to introduce an additional stabilizing penalty term as was done in [3, 4, 7–9].

In [3], an a posteriori error estimate for a Lagrangian functional was derived. A similar estimate was given in [19], but there the amount of detail provided in the proof was, for the sake of brevity, kept to a minimum. Here we give the fully detailed proof of that estimate. Moreover, we extend the error analysis also to include a posteriori error estimation for the Tikhonov functional, as well as for the permittivity function itself. The arguments which we use here could easily be adapted to obtain such estimates also for the original version of the second stage considered in [3, 4, 7–9].

The remaining part of this note is structured as follows: In the next section we present the mathematical formulations of the direct and inverse problems and present the basic results prior to discretization of the problems. In Section 3 we state the finite element formulations and perform the error analysis. Some concluding remarks are given in Section 4.

2. The direct and inverse problems

Before proceeding with the mathematical statement of the problem, we introduce some notation. For the bounded domain $\Omega \subset \mathbb{R}^3$ with boundary Γ, we write $\Omega_T := \Omega \times (0, T)$ and $\Gamma_T := \Gamma \times (0, T)$, where $T > 0$ is a (sufficiently large) fixed time. If $X \subset \mathbb{R}^n$, $n \in \mathbb{N}$, is a domain, we define the norm $\|\cdot\|_{X,m} := \|\cdot\|_{H^m(X)}$ and corresponding inner product $\langle \cdot, \cdot \rangle_{X,m} := \langle \cdot, \cdot \rangle_{H^m(X)}$, where $H^m(X)$ is the L_2-based Sobolev space of order m over X, with respect to the usual Lebesgue measure. To simplify notation, we will drop the index m whenever it is zero.

Let $V^\varepsilon := H^3(\Omega)$. We define the set of admissible dielectric permittivity functions

$$U^\varepsilon := \{v \in V^\varepsilon : 1 \le v(\mathbf{x}) \le \varepsilon_{\max}\ \forall \mathbf{x} \in \Omega,\ v|_\Gamma \equiv 1,\ \nabla v|_\Gamma \equiv 0\} \tag{2.1}$$

for some known but not necessarily small upper bound $\varepsilon_{\max}$. The set U^ε is defined to describe a heterogeneous medium in Ω, immersed in a constant background with permittivity 1 in $\mathbb{R}^3 \setminus \Omega$.

Under the assumption that $\varepsilon \in U^\varepsilon$ we consider Maxwell's equations for an isotropic, non-magnetic, non-conductive medium in Ω:

$$\frac{\partial(\mu\mathbf{H})}{\partial t} + \nabla \times \mathbf{E} = 0 \qquad \text{in } \Omega_T, \tag{2.2}$$

$$\frac{\partial(\varepsilon\mathbf{E})}{\partial t} - \nabla \times \mathbf{H} = 0 \qquad \text{in } \Omega_T, \tag{2.3}$$

$$\nabla \cdot (\mu\mathbf{H}) = \nabla \cdot (\varepsilon\mathbf{E}) = 0 \qquad \text{in } \Omega_T, \tag{2.4}$$

where $\mathbf{H} = \mathbf{H}(\mathbf{x}, t)$ and $\mathbf{E} = \mathbf{E}(\mathbf{x}, t)$, $(\mathbf{x}, t) \in \Omega_T$, denote the magnetic and electric fields, respectively, and $\mu > 0$ is the constant magnetic permeability. By scaling, we may assume that $\mu = 1$.

To obtain an equation involving only ε and $\mathbf{E}$, we combine the curl of (2.2) and derivative of (2.3) with respect to t to obtain the second order equation

$$\varepsilon\frac{\partial^2\mathbf{E}}{\partial t^2} + \nabla \times (\nabla \times \mathbf{E}) = 0 \qquad \text{in } \Omega_T.$$

To incorporate (2.4) we proceed as in [19] to expand $\nabla \times (\nabla \times \mathbf{E}) = -\Delta\mathbf{E} + \nabla(\nabla \cdot \mathbf{E})$ and use

$$\nabla \cdot \mathbf{E} = \nabla \cdot \left(\frac{\varepsilon\mathbf{E}}{\varepsilon}\right) = \frac{\nabla \cdot (\varepsilon\mathbf{E})}{\varepsilon} - \frac{\nabla\varepsilon \cdot \mathbf{E}}{\varepsilon},$$

where the term $\nabla \cdot (\varepsilon\mathbf{E})/\varepsilon$ vanishes in view of (2.4).

Thus, after completing with boundary and initial conditions, we obtain the system

$$\begin{aligned}
&\varepsilon\frac{\partial^2\mathbf{E}}{\partial t^2} - \Delta\mathbf{E} - \nabla\left(\frac{\nabla\varepsilon \cdot \mathbf{E}}{\varepsilon}\right) = 0 \quad \text{in } \Omega_T,\\
&\frac{\partial\mathbf{E}}{\partial\boldsymbol{\nu}} = \mathbf{P} \qquad \text{on } \Gamma_T,\\
&\mathbf{E}(\cdot, 0) = \frac{\partial\mathbf{E}}{\partial t}(\cdot, 0) = 0 \qquad \text{in } \Omega,
\end{aligned} \tag{2.5}$$

where $\frac{\partial}{\partial \boldsymbol{\nu}} = \boldsymbol{\nu} \cdot \nabla$, $\boldsymbol{\nu}$ denotes the outward unit normal on Γ, and $\mathbf{P} \in [L_2(\Gamma_T)]^3$ is given Neumann data (see Section 4 of [8] for details). For well-posedness of problems of this class, we refer to [16].

The mathematical statement of the coefficient inverse problem is:

PROBLEM 1. *Given time-resolved boundary observations*

$$\mathbf{G} \in [L_2(\Gamma_T)]^3$$

of the electric field, determine $\varepsilon \in U^{\varepsilon}$ *such that* $\mathbf{E} = \mathbf{G}$ *on* Γ_T.

The observations $\mathbf{G}$ represents either experimental or (partially) simulated data, see [8].

Uniqueness of the solution of coefficient inverse problems of this type is typically obtained via the method of Carleman estimates [11]. Examples where this method is applied to inverse problems for Maxwell's equations can be found in, for example, [14], [10] for simultaneous reconstruction of two coefficients, and [17, 18] for bi-isotropic and anisotropic media. However, this technique requires non-vanishing initial conditions for the underlying partial differential equation, which is not the case here. Thus, currently, uniqueness of the solution for the problem we study is not known. For the purpose of this work, we will assume that uniqueness holds. This assumption is justified by the numerical results presented in [8, 9].

We introduce the space $V^{\mathrm{dir}} := \{\mathbf{v} \in [H^1(\Omega_T)]^3 : \mathbf{v}(\cdot, 0) = 0\}$ for solutions to the direct problem, and $V^{\mathrm{adj}} := \{\mathbf{v} \in [H^1(\Omega_T)]^3 : \mathbf{v}(\cdot, T) = 0\}$ for adjoint solutions. Both spaces are equipped with the usual norm and inner product on $[H^1(\Omega_T)]^3$. Then, by multiplying the first equation in (2.5) by a test function $\boldsymbol{\phi} \in V^{\mathrm{adj}}$ and integration over Ω_T, we obtain, after integration by parts,

(2.6)

$$\begin{aligned}
0 &= -\left\langle \varepsilon \tfrac{\partial \mathbf{E}}{\partial t}, \tfrac{\partial \boldsymbol{\phi}}{\partial t} \right\rangle_{\Omega_T} + \left\langle \varepsilon \tfrac{\partial \mathbf{E}}{\partial t}(\cdot, T), \boldsymbol{\phi}(\cdot, T) \right\rangle_{\Omega} - \left\langle \varepsilon \tfrac{\partial \mathbf{E}}{\partial t}(\cdot, 0), \boldsymbol{\phi}(\cdot, 0) \right\rangle_{\Omega} \\
&\quad + \langle \nabla \mathbf{E}, \nabla \boldsymbol{\phi} \rangle_{\Omega_T} - \left\langle \tfrac{\partial \mathbf{E}}{\partial \boldsymbol{\nu}}, \boldsymbol{\phi} \right\rangle_{\Gamma_T} + \left\langle \tfrac{\nabla \varepsilon \cdot \mathbf{E}}{\varepsilon}, \nabla \cdot \boldsymbol{\phi} \right\rangle_{\Omega_T} - \left\langle \tfrac{\nabla \varepsilon \cdot \mathbf{E}}{\varepsilon}, \boldsymbol{\nu} \cdot \boldsymbol{\phi} \right\rangle_{\Gamma_T} \\
&= -\left\langle \varepsilon \tfrac{\partial \mathbf{E}}{\partial t}, \tfrac{\partial \boldsymbol{\phi}}{\partial t} \right\rangle_{\Omega_T} + \langle \nabla \mathbf{E}, \nabla \boldsymbol{\phi} \rangle_{\Omega_T} + \left\langle \tfrac{\nabla \varepsilon \cdot \mathbf{E}}{\varepsilon}, \nabla \cdot \boldsymbol{\phi} \right\rangle_{\Omega_T} - \langle \mathbf{P}, \boldsymbol{\phi} \rangle_{\Gamma_T} \\
&=: \mathscr{D}(\varepsilon, \mathbf{E}, \boldsymbol{\phi}),
\end{aligned}$$

where the second equality holds because $\boldsymbol{\phi}(\cdot, T) = 0$, $\frac{\partial \mathbf{E}}{\partial t}(\cdot, 0) = 0$, $\frac{\partial \mathbf{E}}{\partial \boldsymbol{\nu}} = \mathbf{P}$ on Γ_T, and $\nabla \varepsilon = 0$ on Γ_T. This leads to the following weak description of the electric field:

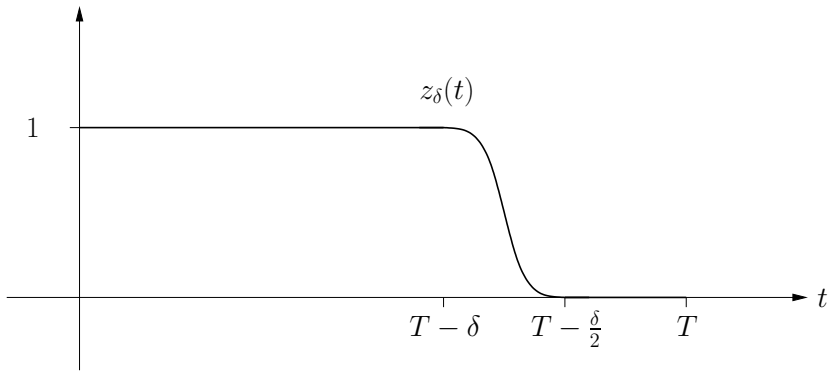

FIGURE 1. Schematic illustration of the cut-off function z_δ appearing in the Tikhonov functional (2.7).

PROBLEM 2. *Given $\varepsilon \in U^\varepsilon$, determine $\mathbf{E} \in V^{\mathrm{dir}}$ such that*

$$\mathscr{D}(\varepsilon, \mathbf{E}, \boldsymbol{\phi}) = 0$$

for every $\boldsymbol{\phi} \in V^{\mathrm{adj}}$.

Let $\mathbf{E}_\varepsilon \in V^{\mathrm{dir}}$ denote the solution to Problem 2 for a given $\varepsilon \in U^\varepsilon$. We can then define the Tikhonov functional $F\colon U^\varepsilon \to \mathbb{R}_+$,

$$F(\varepsilon) = F(\varepsilon, \mathbf{E}_\varepsilon) \coloneqq \frac{1}{2} \|(\mathbf{E}_\varepsilon - \mathbf{G}) z_\delta\|^2_{\Gamma_T} + \frac{\alpha}{2} \|\varepsilon - \varepsilon_0\|^2_\Omega \,, \tag{2.7}$$

where $\alpha > 0$ is a regularization parameter and $z_\delta = z_\delta(t) \in C^\infty([0, T])$ is a cut-off function for the data, dropping from a constant level of 1 to a constant level of 0 within the small interval $(T-\delta, T-\delta/2)$, $0 < \delta \ll T$, as schematically shown in Figure 1. The function z_δ is introduced to ensure data compatibility in the adjoint problem arising in the minimization of (2.7).

How to choose the regularization parameter α with respect to the level of noise in the data is a widely studied topic. Several methods exist, examples are the (generalized) discrepancy principle [20] and iterative methods [1]. For the results presented here, we regard α as a fixed parameter.

As remarked before, the initial approximation ε_0 is obtained using the globally convergent method, as described in, for instance [6]. This means in particular that if ε_0 is sufficiently close to an ideal solution ε^*,

corresponding to noiseless data $\mathbf{G}^*$, and if the regularization parameter α is chosen appropriately with respect to the level of noise in the data $\mathbf{G}$, then by Theorem 3.1 of [7], the Tikhonov functional F is strongly convex in a neighborhood $\mathcal{N} \subset V^\varepsilon$ of ε_0. If so, then in particular there exists a constant $c > 0$ such that for every $\varepsilon_1, \varepsilon_2 \in \mathcal{N} \cap U^\varepsilon$,

$$c \|\varepsilon_1 - \varepsilon_2\|_{V^\varepsilon}^2 \leq F'(\varepsilon_1; \varepsilon_1 - \varepsilon_2) - F'(\varepsilon_2; \varepsilon_1 - \varepsilon_2), \tag{2.8}$$

where $F'(\varepsilon; \bar{\varepsilon})$ denotes the Fréchet derivative of F at ε, acting on $\bar{\varepsilon}$.

Throughout the remaining part of this text we will assume that the hypothesis of Theorem 3.1 of [7], and hence strong convexity, holds. Then we may seek a minimizer $\varepsilon \in U^\varepsilon$ of F by applying any gradient based method (such as steepest descent, quasi-Newton, or conjugate gradient), starting from ε_0.

Such an approach requires that we compute the Fréchet derivative of F, which is complicated since it involves the implicit dependence of $\mathbf{E}_\varepsilon$ upon ε. To simplify the analysis, in the spirit of optimal control (see for example [2, 15] for the general theory and some specific examples), we introduce the Lagrangian

$$L(u) \coloneqq F(\varepsilon, \mathbf{E}) + \mathscr{D}(\varepsilon, \mathbf{E}, \boldsymbol{\lambda}),$$

where $u = (\varepsilon, \mathbf{E}, \boldsymbol{\lambda}) \in U \coloneqq U^\varepsilon \times V^{\mathrm{dir}} \times V^{\mathrm{adj}} \subset V \coloneqq V^\varepsilon \times V^{\mathrm{dir}} \times V^{\mathrm{adj}}$, $F(\varepsilon, \mathbf{E})$ was defined in (2.7), and $\mathscr{D}(\varepsilon, \mathbf{E}, \boldsymbol{\lambda})$ was defined in (2.6).

We can now minimize F over U^ε by minimizing L over U. With the strong convexity as above, this would imply that we solve

PROBLEM 3. *Find $u \in U$ such that $L'(u; v) = 0$ for every $v \in V$.*

Again we use the notation $L'(u; v)$ for the Fréchet derivative of L at u, acting on v. It can be shown (see Proposition 1 of [19]) that

$$L'(u; v) = \frac{\partial L}{\partial \varepsilon}(u; \bar{\varepsilon}) + \frac{\partial L}{\partial \mathbf{E}}(u; \bar{\mathbf{E}}) + \frac{\partial L}{\partial \boldsymbol{\lambda}}(u; \bar{\boldsymbol{\lambda}}),$$

where $u = (\varepsilon,\, \mathbf{E},\, \boldsymbol{\lambda}) \in U$, $v = (\bar{\varepsilon},\, \bar{\mathbf{E}},\, \bar{\boldsymbol{\lambda}}) \in V$, and

(2.9)

$$\frac{\partial L}{\partial \varepsilon}(u;\, \bar{\varepsilon}) \coloneqq \alpha \left\langle \varepsilon - \varepsilon_0,\, \bar{\varepsilon} \right\rangle_{\Omega} - \left\langle \tfrac{\partial \mathbf{E}}{\partial t} \cdot \tfrac{\partial \boldsymbol{\lambda}}{\partial t},\, \bar{\varepsilon} \right\rangle_{\Omega_T} + \left\langle (\nabla \cdot \boldsymbol{\lambda})\mathbf{E},\, \nabla \left(\tfrac{\bar{\varepsilon}}{\varepsilon} \right) \right\rangle_{\Omega_T},$$

$$\frac{\partial L}{\partial \mathbf{E}}(u;\, \bar{\mathbf{E}}) \coloneqq \left\langle (\mathbf{E} - \mathbf{G}) z_\delta^2,\, \bar{\mathbf{E}} \right\rangle_{\Gamma_T} - \left\langle \varepsilon \tfrac{\partial \boldsymbol{\lambda}}{\partial t},\, \tfrac{\partial \bar{\mathbf{E}}}{\partial t} \right\rangle_{\Omega_T} + \left\langle \nabla \boldsymbol{\lambda},\, \nabla \bar{\mathbf{E}} \right\rangle_{\Omega_T}$$
$$+ \left\langle \tfrac{\nabla \cdot \boldsymbol{\lambda}}{\varepsilon} \nabla \varepsilon,\, \bar{\mathbf{E}} \right\rangle_{\Omega_T} =: \mathscr{A}(\varepsilon,\, \boldsymbol{\lambda},\, \bar{\mathbf{E}}),$$

$$\frac{\partial L}{\partial \boldsymbol{\lambda}}(u;\, \bar{\boldsymbol{\lambda}}) = \mathscr{D}(\varepsilon,\, \mathbf{E},\, \bar{\boldsymbol{\lambda}}).$$

In particular, we note that the solution $u = (\varepsilon,\, \mathbf{E},\, \boldsymbol{\lambda})$ to Problem 3 must satisfy $\mathscr{D}(\varepsilon,\, \mathbf{E},\, \bar{\boldsymbol{\lambda}}) = 0$ for every $\bar{\boldsymbol{\lambda}} \in V^{\mathrm{adj}}$ and $\mathscr{A}(\varepsilon,\, \boldsymbol{\lambda},\, \bar{\mathbf{E}}) = 0$ for every $\bar{\mathbf{E}} \in V^{\mathrm{dir}}$. The former means that $\mathbf{E}$ solves Problem 2 and the latter that $\boldsymbol{\lambda}$ solves the following adjoint problem:

PROBLEM 4. *Given $\varepsilon \in U^{\varepsilon}$, determine $\boldsymbol{\lambda} \in V^{\mathrm{adj}}$ such that*

$$\mathscr{A}(\varepsilon,\, \boldsymbol{\lambda},\, \boldsymbol{\phi}) = 0$$

for every $\boldsymbol{\phi} \in V^{\mathrm{dir}}$.

The functional $\mathscr{A}$ in Problem 4 was defined in (2.9). The problem can be seen as a weak analogue of the following system, adjoint to (2.5):

$$\begin{aligned}
&\varepsilon \frac{\partial^2 \boldsymbol{\lambda}}{\partial t^2} - \Delta \boldsymbol{\lambda} - \frac{\nabla \cdot \boldsymbol{\lambda}}{\varepsilon} \nabla \varepsilon = 0 && \text{in } \Omega_T, \\
&\frac{\partial \boldsymbol{\lambda}}{\partial \boldsymbol{\nu}} = -(\mathbf{E} - \mathbf{G}) z_\delta^2 && \text{on } \Gamma_T, \\
&\boldsymbol{\lambda}(\cdot,\, T) = \frac{\partial \boldsymbol{\lambda}}{\partial t}(\cdot,\, T) = 0 && \text{in } \Omega.
\end{aligned}$$

These observations will be used in the error analysis to be described below. But first we shall make some remarks concerning the relation between the Fréchet derivative of Tikhonov functional and that of the Lagrangian.

Let $u_\varepsilon = (\varepsilon,\, \mathbf{E}_\varepsilon,\, \boldsymbol{\lambda}_\varepsilon)$ be the element of U obtained by taking $\mathbf{E}_\varepsilon$ as the solution to Problem 2 and $\boldsymbol{\lambda}_\varepsilon$ as the solution to Problem 4 for the given $\varepsilon \in U^{\varepsilon}$. Then, under assumption of sufficient stability of the weak solutions $\mathbf{E}_\varepsilon$ and $\boldsymbol{\lambda}_\varepsilon$ with respect to ε, the observation that

$$F(\varepsilon) = F(\varepsilon,\, \mathbf{E}_\varepsilon) = F(\varepsilon,\, \mathbf{E}_\varepsilon) + \mathscr{D}(\varepsilon,\, \mathbf{E}_\varepsilon,\, \boldsymbol{\lambda}_\varepsilon) = L(u_\varepsilon),$$

(as $\mathscr{D}(\varepsilon, \mathbf{E}_\varepsilon, \boldsymbol{\lambda}_\varepsilon) = 0$) leads to

$$F'(\varepsilon; \cdot) = \frac{\partial L}{\partial \varepsilon}(u_\varepsilon; \cdot). \tag{2.10}$$

Estimate (2.8) and identity (2.10) will play an important role in the error analysis for the Tikhonov functional and for the coefficient.

3. Finite element formulations and error analysis

In this section we will give finite element formulations for discretizing Problems 2, 3 and 4. After that we will turn to the error analysis. We begin by defining finite-dimensional analogues of the spaces V^ε, V^{dir}, V^{adj}, and V, as well as subsets corresponding to U^ε and U.

Let $\mathcal{T}_h \coloneqq \{K\}$ be a triangulation of Ω and let $\mathcal{I}_\tau$ be a uniform partition of $(0, T)$ into subintervals $(t_k, t_{k+1}]$, $t_k = k\tau$, $k = 0, \ldots, N_\tau$, of length $\tau = T/N_\tau$. With $\mathcal{T}_h$ we associate a mesh-function $h = h(\mathbf{x})$ such that $h(\mathbf{x}) = \operatorname{diam}(K)$ for $\mathbf{x} \in K \in \mathcal{T}_h$. On these meshes we define[2]

$$\begin{aligned}
V_h^\varepsilon &\coloneqq \{v \in V^\varepsilon : v|_K \in P^q(K)\ \forall K \in \mathcal{T}_h\},\\
U_h^\varepsilon &\coloneqq V_h^\varepsilon \cap U^\varepsilon,\\
V_h^{\mathrm{dir}} &\coloneqq \{v \in V^{\mathrm{dir}} : v|_{K\times I} \in [P^1(K)]^3 \times P^1(I)\ \forall K \in \mathcal{T}_h\ \forall I \in \mathcal{I}_\tau\},\\
V_h^{\mathrm{adj}} &\coloneqq \{v \in V^{\mathrm{adj}} : v|_{K\times I} \in [P^1(K)]^3 \times P^1(I)\ \forall K \in \mathcal{T}_h\ \forall I \in \mathcal{I}_\tau\},\\
V_h &\coloneqq V_h^\varepsilon \times V_h^{\mathrm{dir}} \times V_h^{\mathrm{adj}},\\
U_h &\coloneqq U_h^\varepsilon \times V_h^{\mathrm{dir}} \times V_h^{\mathrm{adj}},
\end{aligned}$$

where $P^n(X)$ denotes the space of polynomials of degree at most $n \in \mathbb{N}$ over X, and the degree q used in the finite-dimensional analogue V_h^ε of V^ε is at least 1.

Using these spaces we can state finite element versions of Problems 2 and 4 as Problem 5 and Problem 6, respectively, as follows:

PROBLEM 5. *Given $\varepsilon \in U^\varepsilon$, determine $\mathbf{E}_h \in V_h^{\mathrm{dir}}$ such that*

$$\mathscr{D}(\varepsilon, \mathbf{E}_h, \boldsymbol{\phi}_h) = 0$$

for every $\boldsymbol{\phi}_h \in V_h^{\mathrm{adj}}$.

[2]Observe that the dependence on the step size τ in time is not explicitly included in the notation for the finite-dimensional spaces. This is justified by the fact that τ should be selected with regard to h in accordance with the Courant-Friedrichs-Lewy condition.

PROBLEM 6. *Given $\varepsilon \in U^{\varepsilon}$, determine $\boldsymbol{\lambda}_h \in V_h^{\mathrm{adj}}$ such that*

$$\mathscr{A}(\varepsilon,\, \boldsymbol{\lambda}_h,\, \boldsymbol{\phi}_h) = 0$$

for every $\boldsymbol{\phi} \in V_h^{\mathrm{dir}}$.

The finite-dimensional analogue for Problem 3 is:

PROBLEM 7. *Find $u_h = (\varepsilon_h,\, \mathbf{E}_h,\, \boldsymbol{\lambda}_h) \in U_h$ such that $L'(u_h,\, v) = 0$ for every $v \in V_h$.*

The same remark that was made in conjunction with Problem 3 is also valid here: it holds that $\mathbf{E}_h$ solves Problem 5 and $\boldsymbol{\lambda}_h$ solves Problem 6 for $\varepsilon = \varepsilon_h$.

We will now focus on estimations of the difference between the solution to Problem 3 and Problem 7. We begin by introducing some additional notation. For $v = (\varepsilon,\, \mathbf{E},\, \boldsymbol{\lambda}) \in V$ we denote (with some slight abuse of notation) its interpolant in V_h by

$$\Pi_h v = (\Pi_h \varepsilon,\, \Pi_h \mathbf{E},\, \Pi_h \boldsymbol{\lambda}),$$

and the interpolation error by

$$r_h v = v - \Pi_h v = (r_h \varepsilon,\, r_h \mathbf{E},\, r_h \boldsymbol{\lambda}).$$

We will also need to consider jumps of discontinuous functions over $\mathcal{T}_h$ and $\mathcal{I}_\tau$. Let $K_1,\, K_2 \in \mathcal{T}_h$ such that $\partial K_1 \cap \partial K_2 = e \neq \varnothing$. For $\mathbf{x} \in e$ we define

$$\{v\}_{\mathrm{s}}(\mathbf{x}) \coloneqq \lim_{\mathbf{y} \to \mathbf{x},\, \mathbf{y} \in K_1} v(\mathbf{y}) + \lim_{\mathbf{y} \to \mathbf{x},\, \mathbf{y} \in K_2} v(\mathbf{y}),$$

so that in particular if $v = w\boldsymbol{\nu}$, where w is piecewise constant on $\mathcal{T}_h$ and $\boldsymbol{\nu}$ is the outward unit normal, then $\{v\}_{\mathrm{s}} = \{w\boldsymbol{\nu}\}_{\mathrm{s}} = (w\boldsymbol{\nu})|_{K_1} + (w\boldsymbol{\nu})|_{K_2}$ is the normal jump across e. We extend $\{\cdot\}_{\mathrm{s}}$ to every edge in $\mathcal{T}_h$ by defining $\{v\}_{\mathrm{s}}(\mathbf{x}) = 0$ for $\mathbf{x} \in K \cap \Gamma$, $K \in \mathcal{T}_h$. The corresponding maximal jump is defined by

$$[v]_{\mathrm{s}}(\mathbf{x}) \coloneqq \max_{\mathbf{y} \in \partial K} |\{v\}_{\mathrm{s}}(\mathbf{y})|, \quad \mathbf{x} \in K \in \mathcal{T}_h.$$

For jumps in time, we define

$$\{v\}_{\mathrm{t}}(t_k) \coloneqq \begin{cases} \lim\limits_{s \to 0+} \big(v(t_k + s) - v(t_k - s)\big), & k = 1,\, \ldots,\, N_\tau - 1, \\ 0 & k = 0,\, N_\tau, \end{cases}$$

and

$$[v]_{\mathrm{t}}(t) \coloneqq \max\{|\{v\}_{\mathrm{t}}(t_k)|,\, |\{v\}_{\mathrm{t}}(t_{k+1})|\} \quad t \in (t_k,\, t_{k+1}).$$

In the theorems and proofs to be presented, we will frequently use the symbols $\approx$ and $\lesssim$ to denote approximate equality and inequality, respectively, where higher order terms (with respect to mesh-size or errors) are neglected.

We are now ready to present the first a posteriori error estimate, an estimate for the Lagrangian. The theorem was first presented in [19], but with only a very brief proof. We will here give the full details of the proof. Let us start by recalling the theorem:

THEOREM 3.1. *(A posteriori error estimate for the Lagrangian.) Let $u = (\varepsilon, \mathbf{E}, \boldsymbol{\lambda}) \in U$ be the solution to Problem 3 and $u_h = (\varepsilon_h, \mathbf{E}_h, \boldsymbol{\lambda}_h) \in U_h$ be the solution to Problem 7. Then there exists a constant C, which does not depend on u, u_h, h, or τ, such that*

$$
\begin{aligned}
|L(u) - L(u_h)| \lesssim C \Big(& \Big\langle |R_\varepsilon|, \, h \left| \left[\tfrac{\partial \varepsilon_h}{\partial \boldsymbol{\nu}} \right]_{\mathrm{s}} \right| \Big\rangle_{\Omega} \\
& + \left\langle R_{\boldsymbol{\lambda},\Omega}, \, \tau \left| \left[\tfrac{\partial \mathbf{E}_h}{\partial t} \right]_{\mathrm{t}} \right| + h \left| \left[\tfrac{\partial \mathbf{E}_h}{\partial \boldsymbol{\nu}} \right]_{\mathrm{s}} \right| \right\rangle_{\Omega_T} \\
& + \left\langle R_{\boldsymbol{\lambda},\Gamma}, \, \tau \left| \left[\tfrac{\partial \mathbf{E}_h}{\partial t} \right]_{\mathrm{t}} \right| + h \left| \left[\tfrac{\partial \mathbf{E}_h}{\partial \boldsymbol{\nu}} \right]_{\mathrm{s}} \right| \right\rangle_{\Gamma_T} \\
& + \left\langle R_{\mathbf{E},\Omega}, \, \tau \left| \left[\tfrac{\partial \boldsymbol{\lambda}_h}{\partial t} \right]_{\mathrm{t}} \right| + h \left| \left[\tfrac{\partial \boldsymbol{\lambda}_h}{\partial \boldsymbol{\nu}} \right]_{\mathrm{s}} \right| \right\rangle_{\Omega_T} \\
& + \left\langle R_{\mathbf{E},\Gamma}, \, \tau \left| \left[\tfrac{\partial \boldsymbol{\lambda}_h}{\partial t} \right]_{\mathrm{t}} \right| + h \left| \left[\tfrac{\partial \boldsymbol{\lambda}_h}{\partial \boldsymbol{\nu}} \right]_{\mathrm{s}} \right| \right\rangle_{\Gamma_T} \Big),
\end{aligned}
$$

where

$$
\begin{aligned}
R_\varepsilon &= \alpha(\varepsilon_h - \varepsilon_0) - \int_0^T \frac{\partial \mathbf{E}_h}{\partial t}(\cdot, t) \cdot \frac{\partial \boldsymbol{\lambda}_h}{\partial t}(\cdot, t) \, \mathrm{d}t \\
&\quad - \int_0^T \frac{\nabla \cdot \mathbf{E}_h(\cdot, t) \nabla \cdot \boldsymbol{\lambda}_h(\cdot, t)}{\varepsilon_h} \, \mathrm{d}t + \int_0^T \frac{[(\boldsymbol{\nu} \cdot \mathbf{E}_h)(\nabla \cdot \boldsymbol{\lambda}_h)]_{\mathrm{s}}}{h \varepsilon_h} \, \mathrm{d}t, \\
R_{\boldsymbol{\lambda},\Omega} &= -\varepsilon_h \frac{\left[\frac{\partial \boldsymbol{\lambda}_h}{\partial t} \right]_{\mathrm{t}}}{\tau} + \frac{\left[\frac{\partial \boldsymbol{\lambda}}{\partial \boldsymbol{\nu}} \right]_{\mathrm{s}}}{2h} + \frac{\nabla \cdot \boldsymbol{\lambda}_h}{\varepsilon_h} \nabla \varepsilon_h, \\
R_{\boldsymbol{\lambda},\Gamma} &= \frac{\partial \boldsymbol{\lambda}_h}{\partial \boldsymbol{\nu}} + (\mathbf{E}_h - \mathbf{G}) z_\delta^2,
\end{aligned}
$$

$$R_{\mathbf{E},\,\Omega} = -\varepsilon_h \frac{\left[\frac{\partial \mathbf{E}_h}{\partial t}\right]_{\mathrm{t}}}{\tau} + \frac{\left[\frac{\partial \mathbf{E}_h}{\partial \boldsymbol{\nu}}\right]_{\mathrm{s}}}{2h} + \frac{\nabla\varepsilon_h \cdot \mathbf{E}_h}{\varepsilon_h^2}\nabla\varepsilon_h - \frac{J_{\nabla\varepsilon_h}^{\mathsf{T}}\mathbf{E}_h + J_{\mathbf{E}_h}^{\mathsf{T}}\nabla\varepsilon_h}{\varepsilon_h} + \frac{[(\nabla\varepsilon_h \cdot \mathbf{E}_h)\boldsymbol{\nu}]_{\mathrm{s}}}{2h\varepsilon_h},$$

$$R_{\mathbf{E},\,\Gamma} = \frac{\partial \mathbf{E}_h}{\partial \boldsymbol{\nu}} - \mathbf{P}.$$

Here $J_{\nabla\varepsilon_h}$ and $J_{\mathbf{E}_h}$ denotes the Jacobi matrices of $\nabla\varepsilon_h$ and $\mathbf{E}_h$, respectively, and $(\cdot)^{\mathsf{T}}$ denotes matrix transpose.

Note that if ε_h is piecewise linear, $J_{\nabla\varepsilon_h}|_K \equiv 0$ for every $K \in \mathcal{T}_h$, hence the corresponding term in $R_{\mathbf{E},\,\Omega}$ vanishes in that case.

In the following proof, and thereafter, C is used to denote various constants of moderate size which do not depend on u, u_h, h, or τ.

Proof. Using the definition of the Fréchet derivative we get

$$L(u) - L(u_h) = L'(u_h;\, u - u_h) + o(\|u - u_h\|_V)$$

The split $u - u_h = (u - \Pi_h u) + (\Pi_h u - u_h) = r_h u + (\Pi_h u - u_h)$ now gives

$$\begin{aligned} L(u) - L(u_h) &= L'(u_h;\, r_h u + (\Pi_h u - u_h)) + o(\|u - u_h\|_V) \\ &= L'(u_h;\, r_h u) + L'(u_h;\, \Pi_h u - u_h) + o(\|u - u_h\|_V). \end{aligned}$$

The second term vanishes since $\Pi_h u - u_h \in V_h$ and u_h solves Problem 7, and we neglect the remainder term $o(\|u - u_h\|_V)$ since it is of higher order with respect to the error. We are then left with

$$L(u) - L(u_h) \approx L'(u_h;\, r_h u) = \frac{\partial L}{\partial \varepsilon}(u_h;\, r_h\varepsilon) + \frac{\partial L}{\partial \mathbf{E}}(u_h;\, r_h\mathbf{E}) + \frac{\partial L}{\partial \boldsymbol{\lambda}}(u_h;\, r_h\boldsymbol{\lambda}),$$

and individual estimation of these three terms will give the stated result.

Starting with the first term, we observe that

$$\frac{\partial L}{\partial \varepsilon}(u_h;\, r_h\varepsilon) = \alpha\,\langle \varepsilon_h - \varepsilon_0,\, r_h\varepsilon\rangle_\Omega - \left\langle \tfrac{\partial \mathbf{E}_h}{\partial t} \cdot \tfrac{\partial \boldsymbol{\lambda}_h}{\partial t},\, r_h\varepsilon \right\rangle_{\Omega_T} + \left\langle (\nabla \cdot \boldsymbol{\lambda}_h)\mathbf{E}_h,\, \nabla\left(\tfrac{r_h\varepsilon}{\varepsilon_h}\right)\right\rangle_{\Omega_T}.$$

We aim at lifting all derivatives from the interpolation errors, thus we split the inner product over Ω_T in the last term above into the sum of inner products over $K_T \coloneqq K \times (0,\, T)$, $K \in \mathcal{T}_h$:

$$\left\langle (\nabla \cdot \boldsymbol{\lambda}_h)\mathbf{E}_h,\, \nabla\left(\tfrac{r_h\varepsilon}{\varepsilon_h}\right)\right\rangle_{\Omega_T} = \sum_{K\in\mathcal{T}_h} \left\langle (\nabla \cdot \boldsymbol{\lambda}_h)\mathbf{E}_h,\, \nabla\left(\tfrac{r_h\varepsilon}{\varepsilon_h}\right)\right\rangle_{K_T}.$$

We now integrate by parts, using the notation $\partial K_T \coloneqq \partial K \times (0,\, T)$, $\partial K_T' \coloneqq (\partial K \setminus \Gamma) \times (0,\, T)$, $\partial K_T'' \coloneqq (\partial K \cap \Gamma) \times (0,\, T)$, $K \in \mathcal{T}_h$:

$$
\begin{aligned}
&\sum_{K\in\mathcal{T}_h} \left\langle (\nabla\cdot\boldsymbol{\lambda}_h)\mathbf{E}_h,\, \nabla\left(\tfrac{r_h\varepsilon}{\varepsilon_h}\right)\right\rangle_{K_T} \\
&\quad= \sum_{K\in\mathcal{T}_h} \left(-\left\langle \nabla\cdot\big((\nabla\cdot\boldsymbol{\lambda}_h)\mathbf{E}_h\big),\, \tfrac{r_h\varepsilon}{\varepsilon_h}\right\rangle_{K_T} + \left\langle (\nabla\cdot\boldsymbol{\lambda}_h)(\boldsymbol{\nu}\cdot\mathbf{E}_h),\, \tfrac{r_h\varepsilon}{\varepsilon_h}\right\rangle_{\partial K_T}\right) \\
&\quad= \sum_{K\in\mathcal{T}_h} \left(-\left\langle \tfrac{\nabla(\nabla\cdot\boldsymbol{\lambda}_h)\cdot\mathbf{E}_h}{\varepsilon_h},\, r_h\varepsilon\right\rangle_{K_T} - \left\langle \tfrac{(\nabla\cdot\boldsymbol{\lambda}_h)(\nabla\cdot\mathbf{E}_h)}{\varepsilon_h},\, r_h\varepsilon\right\rangle_{K_T}\right. \\
&\qquad\qquad \left. + \left\langle \tfrac{(\nabla\cdot\boldsymbol{\lambda}_h)(\boldsymbol{\nu}\cdot\mathbf{E}_h)}{\varepsilon_h},\, r_h\varepsilon\right\rangle_{\partial K_T'} + \left\langle \tfrac{(\nabla\cdot\boldsymbol{\lambda}_h)(\boldsymbol{\nu}\cdot\mathbf{E}_h)}{\varepsilon_h},\, r_h\varepsilon\right\rangle_{\partial K_T''}\right) \\
&\quad= -\sum_{K\in\mathcal{T}_h} \left\langle \tfrac{\nabla(\nabla\cdot\boldsymbol{\lambda}_h)\cdot\mathbf{E}_h}{\varepsilon_h},\, r_h\varepsilon\right\rangle_{K_T} - \left\langle \tfrac{(\nabla\cdot\boldsymbol{\lambda}_h)(\nabla\cdot\mathbf{E}_h)}{\varepsilon_h},\, r_h\varepsilon\right\rangle_{\Omega_T} \\
&\qquad + \sum_{K\in\mathcal{T}_h} \left\langle \tfrac{(\nabla\cdot\boldsymbol{\lambda}_h)(\boldsymbol{\nu}\cdot\mathbf{E}_h)}{\varepsilon_h},\, r_h\varepsilon\right\rangle_{\partial K_T'} + \left\langle \tfrac{(\nabla\cdot\boldsymbol{\lambda}_h)(\boldsymbol{\nu}\cdot\mathbf{E}_h)}{\varepsilon_h},\, r_h\varepsilon\right\rangle_{\Gamma_T}.
\end{aligned}
$$

We observe that $\nabla(\nabla\cdot\boldsymbol{\lambda}_h) \equiv 0$ on every K_T, $K \in \mathcal{T}_h$, since $\boldsymbol{\lambda}_h$ is piecewise linear, and that $\varepsilon \equiv 1$ on Γ so that $r_h\varepsilon|_\Gamma \equiv 0$. With this in mind, the above calculations yields

$$
\begin{aligned}
\left\langle (\nabla\cdot\boldsymbol{\lambda}_h)\mathbf{E}_h,\, \nabla\left(\tfrac{r_h\varepsilon}{\varepsilon_h}\right)\right\rangle_{\Omega_T} &= -\left\langle \tfrac{(\nabla\cdot\boldsymbol{\lambda}_h)(\nabla\cdot\mathbf{E}_h)}{\varepsilon_h},\, r_h\varepsilon\right\rangle_{\Omega_T} \\
&\quad + \sum_{K\in\mathcal{T}_h} \left\langle \tfrac{(\nabla\cdot\boldsymbol{\lambda}_h)(\boldsymbol{\nu}\cdot\mathbf{E}_h)}{\varepsilon_h},\, r_h\varepsilon\right\rangle_{\partial K_T'}.
\end{aligned}
$$

In order to obtain a residual defined in the whole of Ω, as opposed to one containing terms defined only on edges of elements $K \in \mathcal{T}_h$, we should manipulate the last term in the above expression further. Observe that

$$
\begin{aligned}
&\sum_{K\in\mathcal{T}_h} \left\langle \tfrac{1}{\varepsilon_h}(\nabla\cdot\boldsymbol{\lambda}_h)(\boldsymbol{\nu}\cdot\mathbf{E}_h),\, r_h\varepsilon\right\rangle_{\partial K_T'} = \\
&\qquad \frac{1}{2}\sum_{K\in\mathcal{T}_h} \left\langle \tfrac{1}{\varepsilon_h}\left\{(\nabla\cdot\boldsymbol{\lambda}_h)(\boldsymbol{\nu}\cdot\mathbf{E}_h)\right\}_{\mathrm{s}},\, r_h\varepsilon\right\rangle_{\partial K_T'},
\end{aligned}
$$

where the factor $\frac{1}{2}$ appears since every internal edge is counted exactly twice in the sum over all elements $K \in \mathcal{T}_h$.

Using the approximation

$$\int_{\partial K} f \,\mathrm{d}S \approx \int_K \frac{\tilde{f}}{h_K} \,\mathrm{d}\mathbf{x}$$

where $\tilde{f}$ denotes the maximum of f over ∂K (see for instance [12]), we finally get

$$\begin{aligned}
&\sum_{K\in\mathcal{T}_h} \left\langle \tfrac{1}{\varepsilon_h} \left\{ (\nabla\cdot\boldsymbol{\lambda}_h)(\boldsymbol{\nu}\cdot\mathbf{E}_h) \right\}_{\mathrm{s}}, r_h\varepsilon \right\rangle_{\partial K_T'} \\
&\qquad \approx \sum_{K\in\mathcal{T}_h} \left\langle \tfrac{1}{h_K\varepsilon_h} \left[(\nabla\cdot\boldsymbol{\lambda}_h)(\boldsymbol{\nu}\cdot\mathbf{E}_h) \right]_{\mathrm{s}}, r_h\varepsilon \right\rangle_{K_T} \\
&\qquad = \left\langle \tfrac{1}{h\varepsilon_h} \left[(\nabla\cdot\boldsymbol{\lambda}_h)(\boldsymbol{\nu}\cdot\mathbf{E}_h) \right]_{\mathrm{s}}, r_h\varepsilon \right\rangle_{\Omega_T},
\end{aligned}$$

which gives

$$\begin{aligned}
\frac{\partial L}{\partial \varepsilon}(u_h;\, r_h\varepsilon) &= \alpha \left\langle \varepsilon_h - \varepsilon_0,\, r_h\varepsilon \right\rangle_\Omega + \left\langle \tfrac{\partial \mathbf{E}_h}{\partial t} \cdot \tfrac{\partial \boldsymbol{\lambda}_h}{\partial t},\, r_h\varepsilon \right\rangle_{\Omega_T} \\
&\quad - \left\langle \tfrac{(\nabla\cdot\boldsymbol{\lambda}_h)(\nabla\cdot\mathbf{E}_h)}{\varepsilon_h},\, r_h\varepsilon \right\rangle_{\Omega_T} \\
&\quad + \left\langle \tfrac{1}{h\varepsilon_h} \left[(\nabla\cdot\boldsymbol{\lambda}_h)(\boldsymbol{\nu}\cdot\mathbf{E}_h) \right]_{\mathrm{s}}, r_h\varepsilon \right\rangle_{\Omega_T} \\
&= \left\langle R_\varepsilon,\, r_h\varepsilon \right\rangle_\Omega .
\end{aligned}$$

We can now estimate $r_h\varepsilon$ in terms of ε_h, using standard interpolation techniques (see for instance [13]), as

$$|r_h\varepsilon| \le Ch^2 \left| D^2\varepsilon \right| \approx Ch^2 \left| \frac{\left[\frac{\partial \varepsilon_h}{\partial \boldsymbol{\nu}} \right]_{\mathrm{s}}}{h} \right| = Ch \left| \left[\tfrac{\partial \varepsilon_h}{\partial \boldsymbol{\nu}} \right]_{\mathrm{s}} \right|,$$

where D^2 denotes derivatives of second order with respect to $\mathbf{x}$. Thus

$$\left| \frac{\partial L}{\partial \varepsilon}(u_h;\, r_h\varepsilon) \right| \lesssim C \left\langle |R_\varepsilon|,\, h \left| \left[\tfrac{\partial \varepsilon_h}{\partial \boldsymbol{\nu}} \right]_{\mathrm{s}} \right| \right\rangle_\Omega .$$

We continue with

$$\begin{aligned}
\frac{\partial L}{\partial \mathbf{E}}(u_h;\, r_h\mathbf{E}) &= \left\langle (\mathbf{E}_h - \mathbf{G}) z_\delta^2,\, r_h\mathbf{E} \right\rangle_{\Gamma_T} - \left\langle \varepsilon_h \tfrac{\partial \boldsymbol{\lambda}_h}{\partial t},\, \tfrac{\partial r_h\mathbf{E}}{\partial t} \right\rangle_{\Omega_T} \\
&\quad + \left\langle \nabla\boldsymbol{\lambda}_h,\, \nabla r_h\mathbf{E} \right\rangle_{\Omega_T} + \left\langle \tfrac{\nabla\cdot\boldsymbol{\lambda}_h}{\varepsilon_h} \nabla\varepsilon_h,\, r_h\mathbf{E} \right\rangle_{\Omega_T} .
\end{aligned}$$

Again, we seek to lift derivatives from the interpolation errors, and so we use integration by parts to get

$$\begin{aligned}
\left\langle \varepsilon_h \tfrac{\partial \boldsymbol{\lambda}_h}{\partial t},\, \tfrac{\partial r_h \mathbf{E}}{\partial t} \right\rangle_{\Omega_T} &= \sum_{k=1}^{N_\tau} \int_{t_{k-1}}^{t_k} \left\langle \varepsilon_h \tfrac{\partial \boldsymbol{\lambda}_h}{\partial t},\, \tfrac{\partial r_h \mathbf{E}}{\partial t} \right\rangle_{\Omega} \,\mathrm{d}t \\
&= -\sum_{k=1}^{N_\tau} \int_{t_{k-1}}^{t_k} \left\langle \varepsilon_h \tfrac{\partial^2 \boldsymbol{\lambda}_h}{\partial t^2},\, r_h \mathbf{E} \right\rangle_{\Omega} \,\mathrm{d}t \\
&\quad + \sum_{k=1}^{N_\tau} \left(\left\langle \varepsilon_h \tfrac{\partial \boldsymbol{\lambda}_h}{\partial t},\, r_h \mathbf{E} \right\rangle_{\Omega} |_{t=t_k} - \left\langle \varepsilon_h \tfrac{\partial \boldsymbol{\lambda}_h}{\partial t},\, r_h \mathbf{E} \right\rangle_{\Omega} |_{t=t_{k-1}} \right) \\
&= \sum_{k=1}^{N_\tau - 1} \left\langle \varepsilon_h \left\{ \tfrac{\partial \boldsymbol{\lambda}_h}{\partial t} \right\}_{\mathrm{t}},\, r_h \mathbf{E} \right\rangle_{\Omega} |_{t=t_k} + \left\langle \varepsilon_h \tfrac{\partial \boldsymbol{\lambda}_h}{\partial t},\, r_h \mathbf{E} \right\rangle_{\Omega} |_{t=T} \\
&\quad - \left\langle \varepsilon_h \tfrac{\partial \boldsymbol{\lambda}_h}{\partial t},\, r_h \mathbf{E} \right\rangle_{\Omega} |_{t=0},
\end{aligned}$$

where we have used the fact that $\frac{\partial^2 \boldsymbol{\lambda}_h}{\partial t^2} \equiv 0$ on each subinterval $(t_{k-1},\, t_k)$, for the piecewise linear function $\boldsymbol{\lambda}_h$.

Since $r_h \mathbf{E}(\cdot,\, 0) = \frac{\partial \boldsymbol{\lambda}_h}{\partial t}(\cdot,\, T) = 0$, this leaves us with

$$\left\langle \varepsilon_h \tfrac{\partial \boldsymbol{\lambda}_h}{\partial t},\, \tfrac{\partial r_h \mathbf{E}}{\partial t} \right\rangle_{\Omega_T} = \sum_{k=1}^{N_\tau - 1} \left\langle \varepsilon_h \left\{ \tfrac{\partial \boldsymbol{\lambda}_h}{\partial t} \right\}_{\mathrm{t}},\, r_h \mathbf{E} \right\rangle_{\Omega} |_{t=t_k}.$$

We now approximate the boundary terms by terms defined on the whole interval, using

$$f(t_k) \approx \frac{1}{\tau} \int_{t_{k-1}}^{t_k} f(t) \,\mathrm{d}t,$$

that is

$$\begin{aligned}
\sum_{k=1}^{N_\tau - 1} \left\langle \varepsilon_h \left\{ \tfrac{\partial \boldsymbol{\lambda}_h}{\partial t} \right\}_{\mathrm{t}},\, r_h \mathbf{E} \right\rangle_{\Omega} |_{t=t_k} &\approx \sum_{k=1}^{N_\tau - 1} \frac{1}{\tau} \int_{t_{k-1}}^{t_k} \left\langle \varepsilon_h \left[\tfrac{\partial \boldsymbol{\lambda}_h}{\partial t} \right]_{\mathrm{t}},\, r_h \mathbf{E} \right\rangle_{\Omega} \,\mathrm{d}t \\
&= \left\langle \tfrac{\varepsilon_h}{\tau} \left[\tfrac{\partial \boldsymbol{\lambda}_h}{\partial t} \right]_{\mathrm{t}},\, r_h \mathbf{E} \right\rangle_{\Omega_T}.
\end{aligned}$$

Moving on to

$$\langle \nabla \boldsymbol{\lambda}_h,\, \nabla r_h \mathbf{E} \rangle_{\Omega_T} = \sum_{K \in \mathcal{T}_h} \langle \nabla \boldsymbol{\lambda}_h,\, \nabla r_h \mathbf{E} \rangle_{K_T},$$

we integrate by parts and use the fact that $\Delta\boldsymbol{\lambda}_h \equiv 0$ in every $K \in \mathcal{T}_h$ to obtain

$$\begin{aligned}\langle \nabla\boldsymbol{\lambda}_h,\, \nabla r_h\mathbf{E}\rangle_{\Omega_T} &= \sum_{K\in\mathcal{T}_h}\left(-\langle \Delta\boldsymbol{\lambda}_h,\, r_h\mathbf{E}\rangle_{K_T} + \left\langle \tfrac{\partial\boldsymbol{\lambda}_h}{\partial\boldsymbol{\nu}},\, r_h\mathbf{E}\right\rangle_{\partial K_T}\right)\\ &= \sum_{K\in\mathcal{T}_h}\left(\left\langle \tfrac{\partial\boldsymbol{\lambda}_h}{\partial\boldsymbol{\nu}},\, r_h\mathbf{E}\right\rangle_{\partial K_T'} + \left\langle \tfrac{\partial\boldsymbol{\lambda}_h}{\partial\boldsymbol{\nu}},\, r_h\mathbf{E}\right\rangle_{\partial K_T''}\right)\\ &= \frac{1}{2}\sum_{K\in\mathcal{T}_h}\left\langle \left\{\tfrac{\partial\boldsymbol{\lambda}_h}{\partial\boldsymbol{\nu}}\right\}_{\mathrm{s}},\, r_h\mathbf{E}\right\rangle_{\partial K_T'} + \left\langle \tfrac{\partial\boldsymbol{\lambda}_h}{\partial\boldsymbol{\nu}},\, r_h\mathbf{E}\right\rangle_{\Gamma_T}.\end{aligned}$$

We again approximate inner products over $\partial K_T'$ by inner products over K_T, so that

$$\langle \nabla\boldsymbol{\lambda}_h,\, \nabla r_h\mathbf{E}\rangle_{\Omega_T} \approx \left\langle \tfrac{1}{2h}\left[\tfrac{\partial\boldsymbol{\lambda}_h}{\partial\boldsymbol{\nu}}\right]_{\mathrm{s}},\, r_h\mathbf{E}\right\rangle_{\Omega_T} + \left\langle \tfrac{\partial\boldsymbol{\lambda}_h}{\partial\boldsymbol{\nu}},\, r_h\mathbf{E}\right\rangle_{\Gamma_T}.$$

Together with previous calculations, this gives

$$\begin{aligned}\frac{\partial L}{\partial\mathbf{E}}(u_h;\, r_h\mathbf{E}) &\approx \left\langle (\mathbf{E}_h-\mathbf{G})z_\delta^2,\, r_h\mathbf{E}\right\rangle_{\Gamma_T} - \left\langle \tfrac{\varepsilon_h}{\tau}\left[\tfrac{\partial\boldsymbol{\lambda}_h}{\partial t}\right]_{\mathrm{t}},\, r_h\mathbf{E}\right\rangle_{\Omega_T}\\ &\quad + \left\langle \tfrac{1}{2h}\left[\tfrac{\partial\boldsymbol{\lambda}_h}{\partial\boldsymbol{\nu}}\right]_{\mathrm{s}},\, r_h\mathbf{E}\right\rangle_{\Omega_T} + \left\langle \tfrac{\partial\boldsymbol{\lambda}_h}{\partial\boldsymbol{\nu}},\, r_h\mathbf{E}\right\rangle_{\Gamma_T}\\ &\quad + \left\langle \tfrac{\nabla\cdot\boldsymbol{\lambda}_h}{\varepsilon_h}\nabla\varepsilon_h,\, r_h\mathbf{E}\right\rangle_{\Omega_T}\\ &= \langle R_{\boldsymbol{\lambda},\,\Omega},\, r_h\mathbf{E}\rangle_{\Omega_T} + \langle R_{\boldsymbol{\lambda},\,\Gamma},\, r_h\mathbf{E}\rangle_{\Gamma_T}.\end{aligned}$$

We once more use interpolation estimates

$$|r_h\mathbf{E}| \le C\left(h^2\left|D^2\mathbf{E}\right| + \tau^2\left|\frac{\partial^2\mathbf{E}}{\partial t^2}\right|\right) \approx C\left(h\left|\left[\tfrac{\partial\mathbf{E}_h}{\partial\boldsymbol{\nu}}\right]_{\mathrm{t}}\right| + \tau\left|\left[\tfrac{\partial\mathbf{E}_h}{\partial t}\right]_{\mathrm{s}}\right|\right).$$

to get

$$\begin{aligned}\left|\frac{\partial L}{\partial\mathbf{E}}(u_h;\, r_h\mathbf{E})\right| \lesssim C\Bigg(&\left\langle |R_{\boldsymbol{\lambda},\,\Omega}|,\, h\left|\left[\tfrac{\partial\mathbf{E}_h}{\partial\boldsymbol{\nu}}\right]_{\mathrm{t}}\right| + \tau\left|\left[\tfrac{\partial\mathbf{E}_h}{\partial t}\right]_{\mathrm{s}}\right|\right\rangle_{\Omega_T}\\ &+ \left\langle |R_{\boldsymbol{\lambda},\,\Gamma}|,\, h\left|\left[\tfrac{\partial\mathbf{E}_h}{\partial\boldsymbol{\nu}}\right]_{\mathrm{t}}\right| + \tau\left|\left[\tfrac{\partial\mathbf{E}_h}{\partial t}\right]_{\mathrm{s}}\right|\right\rangle_{\Gamma_T}\Bigg).\end{aligned}$$

It remains to estimate

$$\begin{aligned}\frac{\partial L}{\partial\boldsymbol{\lambda}}(u_h;\, r_h\boldsymbol{\lambda}) &= -\left\langle \varepsilon_h\tfrac{\partial\mathbf{E}_h}{\partial t},\, \tfrac{\partial r_h\boldsymbol{\lambda}}{\partial t}\right\rangle_{\Omega_T} + \langle \nabla\mathbf{E}_h,\, \nabla r_h\boldsymbol{\lambda}\rangle_{\Omega_T}\\ &\quad + \left\langle \tfrac{\nabla\varepsilon_h\cdot\mathbf{E}_h}{\varepsilon_h},\, \nabla\cdot r_h\boldsymbol{\lambda}\right\rangle_{\Omega_T} - \langle \mathbf{P},\, r_h\boldsymbol{\lambda}\rangle_{\Gamma_T}.\end{aligned}$$

Just as before, we obtain

$$\left\langle \varepsilon_h \frac{\partial \mathbf{E}_h}{\partial t},\, \frac{\partial r_h \boldsymbol{\lambda}}{\partial t} \right\rangle_{\Omega_T} \approx \left\langle \frac{\varepsilon_h}{\tau} \left[\frac{\partial \mathbf{E}_h}{\partial t} \right]_{\mathrm{t}},\, r_h \boldsymbol{\lambda} \right\rangle_{\Omega_T}$$

and

$$\langle \nabla \mathbf{E}_h,\, \nabla r_h \boldsymbol{\lambda} \rangle_{\Omega_T} \approx \left\langle \frac{1}{2h} \left[\frac{\partial \mathbf{E}_h}{\partial \boldsymbol{\nu}} \right]_{\mathrm{s}},\, r_h \boldsymbol{\lambda} \right\rangle_{\Omega_T} + \left\langle \frac{\partial \mathbf{E}_h}{\partial \boldsymbol{\nu}},\, r_h \boldsymbol{\lambda} \right\rangle_{\Gamma_T}.$$

Consider the term

$$\left\langle \tfrac{\nabla \varepsilon_h \cdot \mathbf{E}_h}{\varepsilon_h},\, \nabla \cdot r_h \boldsymbol{\lambda} \right\rangle_{\Omega_T} = \sum_{K \in \mathcal{T}_h} \left\langle \tfrac{\nabla \varepsilon_h \cdot \mathbf{E}_h}{\varepsilon_h},\, \nabla \cdot r_h \boldsymbol{\lambda} \right\rangle_{K_T}.$$

Integration by parts yields

$$\begin{aligned}
&\left\langle \tfrac{\nabla \varepsilon_h \cdot \mathbf{E}_h}{\varepsilon_h},\, \nabla \cdot r_h \boldsymbol{\lambda} \right\rangle_{\Omega_T} \\
&\quad = \sum_{K \in \mathcal{T}_h} \left(- \left\langle \nabla \left(\tfrac{\nabla \varepsilon_h \cdot \mathbf{E}_h}{\varepsilon_h} \right),\, r_h \boldsymbol{\lambda} \right\rangle_{K_T} + \left\langle \tfrac{\nabla \varepsilon_h \cdot \mathbf{E}_h}{\varepsilon_h} \boldsymbol{\nu},\, r_h \boldsymbol{\lambda} \right\rangle_{\partial K_T} \right) \\
&\quad = \sum_{K \in \mathcal{T}_h} \left\langle \tfrac{\nabla \varepsilon_h \cdot \mathbf{E}_h}{\varepsilon_h^2} \nabla \varepsilon_h - \tfrac{J^{\mathsf{T}}_{\nabla \varepsilon_h} \mathbf{E}_h + J^{\mathsf{T}}_{\mathbf{E}_h} \nabla \varepsilon_h}{\varepsilon_h},\, r_h \boldsymbol{\lambda} \right\rangle_{K_T} \\
&\qquad + \sum_{K \in \mathcal{T}_h} \left(\left\langle \tfrac{\nabla \varepsilon_h \cdot \mathbf{E}_h}{\varepsilon_h} \boldsymbol{\nu},\, r_h \boldsymbol{\lambda} \right\rangle_{\partial K'_T} + \left\langle \tfrac{\nabla \varepsilon_h \cdot \mathbf{E}_h}{\varepsilon_h} \boldsymbol{\nu},\, r_h \boldsymbol{\lambda} \right\rangle_{\partial K''_T} \right) \\
&\quad = \left\langle \tfrac{\nabla \varepsilon_h \cdot \mathbf{E}_h}{\varepsilon_h^2} \nabla \varepsilon_h - \tfrac{J^{\mathsf{T}}_{\nabla \varepsilon_h} \mathbf{E}_h + J^{\mathsf{T}}_{\mathbf{E}_h} \nabla \varepsilon_h}{\varepsilon_h},\, r_h \boldsymbol{\lambda} \right\rangle_{\Omega_T} \\
&\qquad + \sum_{K \in \mathcal{T}_h} \left\langle \tfrac{1}{\varepsilon_h} \left\{ (\nabla \varepsilon_h \cdot \mathbf{E}_h) \boldsymbol{\nu} \right\}_{\mathrm{s}},\, r_h \boldsymbol{\lambda} \right\rangle_{\partial K'_T} + \left\langle \tfrac{\nabla \varepsilon_h \cdot \mathbf{E}_h}{\varepsilon_h} \boldsymbol{\nu},\, r_h \boldsymbol{\lambda} \right\rangle_{\Gamma_T},
\end{aligned}$$

where for the second equality we have used the identity $\nabla(\nabla \varepsilon_h \cdot \mathbf{E}_h) = J^{\mathsf{T}}_{\nabla \varepsilon_h} \mathbf{E}_h + J^{\mathsf{T}}_{\mathbf{E}_h} \nabla \varepsilon_h$.

Noting that $\nabla \varepsilon_h|_\Gamma \equiv 0$ as $\varepsilon_h \in U_h^\varepsilon$, and using the usual approximation for $\{\cdot\}_{\mathrm{s}}$ inside elements $K \in \mathcal{T}_h$ we get

$$\begin{aligned}
\left\langle \tfrac{\nabla \varepsilon_h \cdot \mathbf{E}_h}{\varepsilon_h},\, \nabla \cdot r_h \boldsymbol{\lambda} \right\rangle_{\Omega_T} \approx &\left\langle \tfrac{\nabla \varepsilon_h \cdot \mathbf{E}_h}{\varepsilon_h^2} \nabla \varepsilon_h - \tfrac{J^{\mathsf{T}}_{\nabla \varepsilon_h} \mathbf{E}_h + J^{\mathsf{T}}_{\mathbf{E}_h} \nabla \varepsilon_h}{\varepsilon_h},\, r_h \boldsymbol{\lambda} \right\rangle \\
&+ \left\langle \tfrac{1}{2h\varepsilon_h} \left[(\nabla \varepsilon_h \cdot \mathbf{E}_h) \boldsymbol{\nu} \right]_{\mathrm{s}},\, r_h \boldsymbol{\lambda} \right\rangle_{\Omega_T}.
\end{aligned}$$

Combining the results for $\frac{\partial L}{\partial \boldsymbol{\lambda}}(u_h;\, r_h\boldsymbol{\lambda})$ and estimating $r_h\boldsymbol{\lambda}$ in terms of $\boldsymbol{\lambda}_h$ just as $r_h\mathbf{E}$ was estimated in terms of $\mathbf{E}_h$ gives

$$\left|\frac{\partial L}{\partial \boldsymbol{\lambda}}(u_h;\, r_h\boldsymbol{\lambda})\right| \lesssim C\left(\left\langle |R_{\mathbf{E},\,\Omega}|,\, h\left|\left[\frac{\partial \boldsymbol{\lambda}_h}{\partial \boldsymbol{\nu}}\right]_{\mathrm{s}}\right| + \tau\left|\left[\frac{\partial \boldsymbol{\lambda}_h}{\partial t}\right]_{\mathrm{t}}\right|\right\rangle_{\Omega_T}\right.$$
$$\left. + \left\langle |R_{\mathbf{E},\,\Gamma}|,\, h\left|\left[\frac{\partial \boldsymbol{\lambda}_h}{\partial \boldsymbol{\nu}}\right]_{\mathrm{s}}\right| + \tau\left|\left[\frac{\partial \boldsymbol{\lambda}_h}{\partial t}\right]_{\mathrm{t}}\right|\right\rangle_{\Gamma_T}\right),$$

which completes the proof. □

One should note that the terms in the error estimate of Theorem 3.1 which are derived from $\frac{\partial L}{\partial \boldsymbol{\lambda}}(u_h;\, r_h\boldsymbol{\lambda})$ and $\frac{\partial L}{\partial \mathbf{E}}(u_h;\, r_h\mathbf{E})$ estimate how accurately the solutions of Problem 2 and Problem 4 are approximated by the solutions of Problem 5 and Problem 6, respectively, for the approximate coefficient ε_h. The remaining term, $\left\langle R_\varepsilon,\, h\left|\left[\frac{\partial \varepsilon_h}{\partial \boldsymbol{\nu}}\right]_{\mathrm{s}}\right|\right\rangle_{\Omega}$ can be interpreted as the error induced by approximating ε by ε_h. Thus, if we are mainly interested in that error, or if we can postulate that the finite element approximations $\mathbf{E}_h$ and $\boldsymbol{\lambda}_h$ are computed with relatively high accuracy, then $|R_\varepsilon|$ may be used as an error indicator by itself. The significance of R_ε will be further illustrated by the error estimates for the coefficient and for the Tikhonov functional.

We now proceed with an error estimate for the coefficient itself. An error estimate for the Tikhonov functional will follow as a corollary.

THEOREM 3.2. *(A posteriori error estimate for the coefficient.) Suppose that the initial approximation ε_0 and the regularization parameter α are such that the strong convexity estimate* (2.8) *holds. Let $u = (\varepsilon,\, \mathbf{E},\, \boldsymbol{\lambda}) \in U$ be the solution to Problem 3, and let $u_h = (\varepsilon_h,\, \mathbf{E}_h,\, \boldsymbol{\lambda}_h) \in U_h$ be the solution to Problem 7, computed on meshes $\mathcal{T}_h$ and $\mathcal{I}_\tau$. Denote by $\tilde{\mathbf{E}}$ and $\tilde{\boldsymbol{\lambda}}$ the solutions to Problem 2 and Problem 4, respectively, with permittivity ε_h, and set $\tilde{u} = (\varepsilon_h,\, \tilde{\mathbf{E}},\, \tilde{\boldsymbol{\lambda}}) \in U$. Then there exists a constant C, which does not depend on u, u_h, h, or τ, such that*

$$\|\varepsilon - \varepsilon_h\|_{V^\varepsilon} \lesssim C(c_\varepsilon \eta + \|R_\varepsilon\|_\Omega),$$

where $c_\varepsilon := \max\{1, \|\nabla \varepsilon_h\|_{L_\infty(\Omega)}\}$ *and* $\eta = \eta(u_h)$ *is defined by*

$$\begin{aligned}\eta := &\left\langle \tfrac{1}{\tau}\left|\left[\frac{\partial \boldsymbol{\lambda}_h}{\partial t}\right]_{\mathrm{t}}\right| + |\nabla\cdot\boldsymbol{\lambda}_h|,\, h\left|\left[\frac{\partial \mathbf{E}_h}{\partial \boldsymbol{\nu}}\right]_{\mathrm{s}}\right| + \tau\left|\left[\frac{\partial \mathbf{E}_h}{\partial t}\right]_{\mathrm{t}}\right|\right\rangle_{\Omega_T}\\ &+\left\langle \tfrac{1}{\tau}\left|\left[\frac{\partial \mathbf{E}_h}{\partial t}\right]_{\mathrm{t}}\right|,\, h\left|\left[\frac{\partial \boldsymbol{\lambda}_h}{\partial \boldsymbol{\nu}}\right]_{\mathrm{s}}\right| + \tau\left|\left[\frac{\partial \boldsymbol{\lambda}_h}{\partial t}\right]_{\mathrm{t}}\right|\right\rangle_{\Omega_T}\\ &+\left\langle |\mathbf{E}_h|,\, \left|\left[\frac{\partial \boldsymbol{\lambda}_h}{\partial \boldsymbol{\nu}}\right]_{\mathrm{s}}\right| + \tau\left|\left[\frac{\partial \nabla\cdot\boldsymbol{\lambda}_h}{\partial t}\right]_{\mathrm{t}}\right|\right\rangle_{\Omega_T}.\end{aligned}$$

PROOF. Using strong convexity (2.8), we obtain

$$\|\varepsilon - \varepsilon_h\|_{V^\varepsilon}^2 \le c\left(F'(\varepsilon;\, \varepsilon - \varepsilon_h) - F'(\varepsilon_h;\, \varepsilon - \varepsilon_h)\right).$$

Since ε minimizes $F(\varepsilon)$ we have $F'(\varepsilon; \varepsilon - \varepsilon_h) = 0$ and thus

$$\|\varepsilon - \varepsilon_h\|_{V^\varepsilon}^2 \le c\left|F'(\varepsilon_h;\, \varepsilon - \varepsilon_h)\right| = c\left|\frac{\partial L}{\partial \varepsilon}(\tilde{u};\, \varepsilon - \varepsilon_h)\right|, \tag{3.1}$$

where the last equality follows from (2.10).

We expand

$$\begin{aligned}\left|\frac{\partial L}{\partial \varepsilon}(\tilde{u};\, \varepsilon - \varepsilon_h)\right| &= \left|\frac{\partial L}{\partial \varepsilon}(\tilde{u};\, \varepsilon - \varepsilon_h) - \frac{\partial L}{\partial \varepsilon}(u_h;\, \varepsilon - \varepsilon_h) + \frac{\partial L}{\partial \varepsilon}(u_h;\, \varepsilon - \varepsilon_h)\right|\\ &\le \left|\frac{\partial L}{\partial \varepsilon}(\tilde{u};\, \varepsilon - \varepsilon_h) - \frac{\partial L}{\partial \varepsilon}(u_h;\, \varepsilon - \varepsilon_h)\right| + \left|\frac{\partial L}{\partial \varepsilon}(u_h;\, \varepsilon - \varepsilon_h)\right|\\ &=: |\Theta_1| + |\Theta_2|,\end{aligned} \tag{3.2}$$

and estimate the two terms $|\Theta_1|$ and $|\Theta_2|$ separately.

For Θ_1 we use the linearization

$$\begin{aligned}\Theta_1 = &\frac{\partial^2 L}{\partial \mathbf{E}\partial \varepsilon}(u_h;\, \tilde{\mathbf{E}} - \mathbf{E}_h; \varepsilon - \varepsilon_h) + o(\|\tilde{\mathbf{E}} - \mathbf{E}_h\|_{\Omega_T,1})\\ &+ \frac{\partial^2 L}{\partial \boldsymbol{\lambda}\partial \varepsilon}(u_h;\, \tilde{\boldsymbol{\lambda}} - \boldsymbol{\lambda}_h; \varepsilon - \varepsilon_h) + o(\|\tilde{\boldsymbol{\lambda}} - \boldsymbol{\lambda}_h\|_{\Omega_T,1}),\end{aligned}$$

where $\frac{\partial^2 L}{\partial \mathbf{E}\partial \varepsilon}$ and $\frac{\partial^2 L}{\partial \boldsymbol{\lambda}\partial \varepsilon}$ denote mixed second partial Fréchet derivatives of L. Again, the remainder terms are neglected as they are of higher order with respect to the error. Thus, after exchanging the order of differentiation, we are left with

$$\Theta_1 \approx D_1|_{\varepsilon-\varepsilon_h}\left(\frac{\partial L}{\partial \mathbf{E}}(u_h;\, \tilde{\mathbf{E}} - \mathbf{E}_h) + \frac{\partial L}{\partial \boldsymbol{\lambda}}(u_h;\, \tilde{\boldsymbol{\lambda}} - \boldsymbol{\lambda}_h)\right), \tag{3.3}$$

where $D_1|_{\varepsilon-\varepsilon_h}$ denotes differentiation with respect to the first component in u_h and action on $\varepsilon - \varepsilon_h$.

We split $\tilde{\mathbf{E}} - \mathbf{E}_h = (\tilde{\mathbf{E}} - \Pi_h\tilde{\mathbf{E}}) + (\Pi_h\tilde{\mathbf{E}} - \mathbf{E}_h) = r_h\tilde{\mathbf{E}} + (\Pi_h\tilde{\mathbf{E}} - \mathbf{E}_h)$ and use the fact that $\boldsymbol{\lambda}_h$ solves Problem 4 with coefficient ε_h, so that $\frac{\partial L}{\partial \mathbf{E}}(u_h;\, \Pi_h\tilde{\mathbf{E}} - \mathbf{E}_h) = 0$ as $\Pi_h\tilde{\mathbf{E}} - \mathbf{E}_h \in V_h^{\mathrm{dir}}$. This gives

(3.4)
$$\frac{\partial L}{\partial \mathbf{E}}(u_h;\, \tilde{\mathbf{E}} - \mathbf{E}_h) = \frac{\partial L}{\partial \mathbf{E}}(u_h;\, r_h\tilde{\mathbf{E}}) + \frac{\partial L}{\partial \mathbf{E}}(u_h;\, \Pi_h\tilde{\mathbf{E}} - \mathbf{E}_h) = \frac{\partial L}{\partial \mathbf{E}}(u_h;\, r_h\tilde{\mathbf{E}}).$$

Similarly, we have

(3.5)
$$\frac{\partial L}{\partial \boldsymbol{\lambda}}(u_h;\, \tilde{\boldsymbol{\lambda}} - \boldsymbol{\lambda}_h) = \frac{\partial L}{\partial \boldsymbol{\lambda}}(u_h;\, r_h\tilde{\boldsymbol{\lambda}}) + \frac{\partial L}{\partial \boldsymbol{\lambda}}(u_h;\, \Pi_h\tilde{\boldsymbol{\lambda}} - \boldsymbol{\lambda}_h) = \frac{\partial L}{\partial \boldsymbol{\lambda}}(u_h;\, r_h\tilde{\boldsymbol{\lambda}}).$$

as $\mathbf{E}_h$ solves Problem 2 with coefficient ε_h.

Combining (3.3), (3.4), and (3.5) gives

$$\begin{aligned}
\Theta_1 &\approx D_1|_{\varepsilon-\varepsilon_h}\left(\frac{\partial L}{\partial \mathbf{E}}(u_h;\, r_h\tilde{\mathbf{E}}) + \frac{\partial L}{\partial \boldsymbol{\lambda}}(u_h;\, r_h\tilde{\boldsymbol{\lambda}})\right) \\
&= -\left\langle (\varepsilon-\varepsilon_h)\tfrac{\partial r_h\tilde{\mathbf{E}}}{\partial t},\, \tfrac{\partial \boldsymbol{\lambda}_h}{\partial t}\right\rangle_{\Omega_T} + \left\langle \nabla\left(\tfrac{\varepsilon-\varepsilon_h}{\varepsilon_h}\right) r_h\tilde{\mathbf{E}},\, \nabla\cdot\boldsymbol{\lambda}_h\right\rangle_{\Omega_T} \\
&\quad - \left\langle (\varepsilon-\varepsilon_h)\tfrac{\partial \mathbf{E}_h}{\partial t},\, \tfrac{\partial r_h\tilde{\boldsymbol{\lambda}}}{\partial t}\right\rangle_{\Omega_T} + \left\langle \nabla\left(\tfrac{\varepsilon-\varepsilon_h}{\varepsilon_h}\right) \mathbf{E}_h,\, \nabla\cdot r_h\tilde{\boldsymbol{\lambda}}\right\rangle_{\Omega_T}.
\end{aligned}$$

In the same manner as in the proof of Theorem 3.1, we integrate by parts in time and approximate jumps to get

$$\begin{aligned}
-\left\langle (\varepsilon-\varepsilon_h)\tfrac{\partial r_h\tilde{\mathbf{E}}}{\partial t},\, \tfrac{\partial \boldsymbol{\lambda}_h}{\partial t}\right\rangle_{\Omega_T} &= \sum_{k=1}^{N_\tau}\int_{t_{k-1}}^{t_k}\left\langle (\varepsilon-\varepsilon_h) r_h\tilde{\mathbf{E}},\, \left\{\tfrac{\partial \boldsymbol{\lambda}_h}{\partial t}\right\}_{\mathrm{t}}\right\rangle_{\Omega}\mathrm{d}t \\
&\approx \left\langle (\varepsilon-\varepsilon_h) r_h\tilde{\mathbf{E}},\, \tfrac{1}{\tau}\left[\tfrac{\partial \boldsymbol{\lambda}_h}{\partial t}\right]_{\mathrm{t}}\right\rangle_{\Omega_T}
\end{aligned}$$

and

$$\begin{aligned}
-\left\langle (\varepsilon-\varepsilon_h)\tfrac{\partial \mathbf{E}_h}{\partial t},\, \tfrac{\partial r_h\tilde{\boldsymbol{\lambda}}}{\partial t}\right\rangle_{\Omega_T} &= \sum_{k=1}^{N_\tau}\int_{t_{k-1}}^{t_k}\left\langle (\varepsilon-\varepsilon_h)\left\{\tfrac{\partial \mathbf{E}_h}{\partial t}\right\}_{\mathrm{t}},\, r_h\tilde{\boldsymbol{\lambda}}\right\rangle_{\Omega}\mathrm{d}t \\
&\approx \left\langle (\varepsilon-\varepsilon_h)\tfrac{1}{\tau}\left[\tfrac{\partial \mathbf{E}_h}{\partial t}\right]_{\mathrm{t}},\, r_h\tilde{\boldsymbol{\lambda}}\right\rangle_{\Omega_T}.
\end{aligned}$$

Thus

$$\begin{aligned}\Theta_1 &\lesssim \left\langle |\varepsilon-\varepsilon_h|\,\tfrac{1}{\tau}\left|\left[\tfrac{\partial \boldsymbol{\lambda}_h}{\partial t}\right]_{\mathrm{t}}\right|,\ \left|r_h\tilde{\mathbf{E}}\right|\right\rangle_{\Omega_T} + \left\langle \left|\nabla\left(\tfrac{\varepsilon-\varepsilon_h}{\varepsilon_h}\right)\right|\,|\nabla\cdot\boldsymbol{\lambda}_h|,\ \left|r_h\tilde{\mathbf{E}}\right|\right\rangle_{\Omega_T}\\ &\quad + \left\langle |\varepsilon-\varepsilon_h|\,\tfrac{1}{\tau}\left|\left[\tfrac{\partial \mathbf{E}_h}{\partial t}\right]_{\mathrm{t}}\right|,\ \left|r_h\tilde{\boldsymbol{\lambda}}\right|\right\rangle_{\Omega_T} + \left\langle \left|\nabla\left(\tfrac{\varepsilon-\varepsilon_h}{\varepsilon_h}\right)\right|\,|\mathbf{E}_h|,\ \left|\nabla\cdot r_h\tilde{\boldsymbol{\lambda}}\right|\right\rangle_{\Omega_T}\\ &\le \|\varepsilon-\varepsilon_h\|_{L_\infty(\Omega)}\left(\left\langle \tfrac{1}{\tau}\left|\left[\tfrac{\partial \boldsymbol{\lambda}_h}{\partial t}\right]_{\mathrm{t}}\right|,\ \left|r_h\tilde{\mathbf{E}}\right|\right\rangle_{\Omega_T} + \left\langle \tfrac{1}{\tau}\left|\left[\tfrac{\partial \mathbf{E}_h}{\partial t}\right]_{\mathrm{t}}\right|,\ \left|r_h\tilde{\boldsymbol{\lambda}}\right|\right\rangle_{\Omega_T}\right)\\ &\quad + \left\|\nabla\left(\tfrac{\varepsilon-\varepsilon_h}{\varepsilon_h}\right)\right\|_{L_\infty(\Omega)}\left(\left\langle |\nabla\cdot\boldsymbol{\lambda}_h|,\ \left|r_h\tilde{\mathbf{E}}\right|\right\rangle_{\Omega_T} + \left\langle |\mathbf{E}_h|,\ \left|\nabla\cdot r_h\tilde{\boldsymbol{\lambda}}\right|\right\rangle_{\Omega_T}\right).\end{aligned}$$

Note that

$$\begin{aligned}\left\|\nabla\left(\tfrac{\varepsilon-\varepsilon_h}{\varepsilon_h}\right)\right\|_{L_\infty(\Omega)} &= \left\|\tfrac{\nabla(\varepsilon-\varepsilon_h)}{\varepsilon_h} - \tfrac{(\varepsilon-\varepsilon_h)\nabla\varepsilon_h}{\varepsilon_h^2}\right\|_{L_\infty(\Omega)}\\ &\le \left\|\tfrac{1}{\varepsilon_h}\right\|_{L_\infty(\Omega)}\|\nabla(\varepsilon-\varepsilon_h)\|_{L_\infty(\Omega)}\\ &\quad + \left\|\tfrac{1}{\varepsilon_h^2}\right\|_{L_\infty(\Omega)}\|\nabla\varepsilon_h\|_{L_\infty(\Omega)}\,\|\varepsilon-\varepsilon_h\|_{L_\infty(\Omega)}\end{aligned}$$

and observe following facts:

$$\begin{aligned}\|\varepsilon-\varepsilon_h\|_{L_\infty(\Omega)} + \|\nabla(\varepsilon-\varepsilon_h)\|_{L_\infty(\Omega)} &\le C\,\|\varepsilon-\varepsilon_h\|_{V^\varepsilon},\\ \left\|\tfrac{1}{\varepsilon_h^p}\right\|_{L_\infty(\Omega)} &\le 1,\quad p\ge 0,\end{aligned}$$

the first following from the Sobolev inequality and the second from noting that $1 \le \varepsilon_h(\mathbf{x}) \le \varepsilon_{\max}$, $\mathbf{x}\in\Omega$, by (2.1).

Using these observations, and interpolation estimates

$$\begin{aligned}\left|r_h\tilde{\mathbf{E}}\right| &\le C\left(h\left|\left[\tfrac{\partial \mathbf{E}_h}{\partial \boldsymbol{\nu}}\right]_{\mathrm{s}}\right| + \tau\left|\left[\tfrac{\partial \mathbf{E}_h}{\partial t}\right]_{\mathrm{t}}\right|\right),\\ \left|r_h\tilde{\boldsymbol{\lambda}}\right| &\le C\left(h\left|\left[\tfrac{\partial \boldsymbol{\lambda}_h}{\partial \boldsymbol{\nu}}\right]_{\mathrm{s}}\right| + \tau\left|\left[\tfrac{\partial \boldsymbol{\lambda}_h}{\partial t}\right]_{\mathrm{t}}\right|\right),\\ \left|\nabla\cdot r_h\tilde{\boldsymbol{\lambda}}\right| &\le C\left(\left|\left[\tfrac{\partial \boldsymbol{\lambda}_h}{\partial \boldsymbol{\nu}}\right]_{\mathrm{s}}\right| + \tau\left|\left[\tfrac{\partial \nabla\cdot\boldsymbol{\lambda}_h}{\partial t}\right]_{\mathrm{t}}\right|\right),\end{aligned}$$

we get

(3.6)

$$\begin{aligned}\Theta_1 \lesssim C \Bigg(& \left\langle \tfrac{1}{\tau} \left| \left[\tfrac{\partial \boldsymbol{\lambda}_h}{\partial t} \right]_{\mathrm{t}} \right|, \, h \left| \left[\tfrac{\partial \mathbf{E}_h}{\partial \boldsymbol{\nu}} \right]_{\mathrm{s}} \right| + \tau \left| \left[\tfrac{\partial \mathbf{E}_h}{\partial t} \right]_{\mathrm{t}} \right| \right\rangle_{\Omega_T} \\ & + \|\nabla \varepsilon_h\|_{L_\infty(\Omega)} \left\langle |\nabla \cdot \boldsymbol{\lambda}_h|, \, h \left| \left[\tfrac{\partial \mathbf{E}_h}{\partial \boldsymbol{\nu}} \right]_{\mathrm{s}} \right| + \tau \left| \left[\tfrac{\partial \mathbf{E}_h}{\partial t} \right]_{\mathrm{t}} \right| \right\rangle_{\Omega_T} \\ & + \left\langle \tfrac{1}{\tau} \left| \left[\tfrac{\partial \mathbf{E}_h}{\partial t} \right]_{\mathrm{t}} \right|, \, h \left| \left[\tfrac{\partial \boldsymbol{\lambda}_h}{\partial \boldsymbol{\nu}} \right]_{\mathrm{s}} \right| + \tau \left| \left[\tfrac{\partial \boldsymbol{\lambda}_h}{\partial t} \right]_{\mathrm{t}} \right| \right\rangle_{\Omega_T} \\ & + \|\nabla \varepsilon_h\|_{L_\infty(\Omega)} \left\langle |\mathbf{E}_h|, \, \left| \left[\tfrac{\partial \boldsymbol{\lambda}_h}{\partial \boldsymbol{\nu}} \right]_{\mathrm{s}} \right| + \tau \left| \left[\tfrac{\partial \nabla \cdot \boldsymbol{\lambda}_h}{\partial t} \right]_{\mathrm{t}} \right| \right\rangle_{\Omega_T} \Bigg) \|\varepsilon - \varepsilon_h\|_{V^\varepsilon} \\ & \leq C c_\varepsilon \eta \, \|\varepsilon - \varepsilon_h\|_{V^\varepsilon} \, ,\end{aligned}$$

where c_ε and η were defined in the statement of the theorem.

Turning to Θ_2 of (3.2), we use the techniques of the proof of Theorem 3.1 to estimate

(3.7)

$$|\Theta_2| \lesssim C \, \langle |R_\varepsilon|, \, |\varepsilon - \varepsilon_h| \rangle_\Omega \leq C \, \|R_\varepsilon\|_\Omega \, \|\varepsilon - \varepsilon_h\|_\Omega \leq C \, \|R_\varepsilon\|_\Omega \, \|\varepsilon - \varepsilon_h\|_{V^\varepsilon} \, .$$

Combining estimates (3.6) and (3.7) with (3.1) and (3.2), we conclude that

$$\|\varepsilon - \varepsilon_h\|_{V^\varepsilon}^2 \lesssim C \left(c_\varepsilon \eta \, \|\varepsilon - \varepsilon_h\|_{V^\varepsilon} + \|R_\varepsilon\|_\Omega \, \|\varepsilon - \varepsilon_h\|_{V^\varepsilon} \right) ,$$

and the result follows. □

Again, just as for the error estimate for the Lagrangian, we see that if the numerical errors for solving the direct and adjoint problems are relatively small, that is, when $\tilde{u} \approx u_h$ with relatively high accuracy, then $\|R_\varepsilon\|_\Omega$ dominates the error estimate.

COROLLARY 1. *(A posteriori error estimate for the Tikhonov functional.) Under the hypothesis of Theorem 3.2, we have*

$$|F(\varepsilon) - F(\varepsilon_h)| \lesssim C \left(c_\varepsilon^2 \eta^2 + \|R_\varepsilon\|_\Omega^2 \right) ,$$

with c_ε and η as defined in Theorem 3.2.

PROOF. Using the definition of the Fréchet derivative and (2.10) we get

$$\begin{aligned} F(\varepsilon) - F(\varepsilon_h) &= F'(\varepsilon_h; \varepsilon - \varepsilon_h) + o(\|\varepsilon - \varepsilon_h\|_{V^\varepsilon}) \\ &= \frac{\partial L}{\partial \varepsilon}(\tilde{u}; \, \varepsilon - \varepsilon_h) + o(\|\varepsilon - \varepsilon_h\|_{V^\varepsilon}). \end{aligned}$$

Neglecting the remainder term as it is of higher order with respect to the error, and estimating $\frac{\partial L}{\partial \varepsilon}(\tilde{u};\, \varepsilon - \varepsilon_h)$ as in the proof of Theorem 3.2, we obtain

$$|F(\varepsilon) - F(\varepsilon_h)| \lesssim C(c_\varepsilon \eta + \|R_\varepsilon\|_{V^\varepsilon}) \, \|\varepsilon - \varepsilon_h\|_{V^\varepsilon} .$$

Applying Theorem 3.2 to estimate $\|\varepsilon - \varepsilon_h\|_{V^\varepsilon}$, we arrive at

$$|F(\varepsilon) - F(\varepsilon_h)| \lesssim C(c_\varepsilon \eta + \|R_\varepsilon\|_{V^\varepsilon})^2 \leq C \left(c_\varepsilon^2 \eta^2 + \|R_\varepsilon\|_{V^\varepsilon}^2 \right).$$

□

4. Conclusion

We have presented three a posteriori error estimates for an adaptive finite element method for the coefficient inverse problem, Problem 1: for the Lagrangian, for the Tikhonov functional and for the coefficient. The latter two are presented here for the first time. Each estimator consists essentially of three parts, an estimate for the error resulting from finite element approximation of the solution to the direct problem, a similar estimate for the finite element approximation of the adjoint problem and an estimate corresponding to the approximation of the coefficient. The latter part is characterized by the residual R_ε in all estimates.

Explicit solution schemes and numerical testing, including the proper choice of regularization parameter α, will be the subject of forthcoming papers.

References

[1] A.B. Bakushinsky, M.Yu. Kokurin, and A. Smirnova. *Iterative Methods for Ill-Posed Problems: An Introduction*. De Gruyter, Berlin, 2011.

[2] R. Becker, H. Kapp, and R. Rannacher. Adaptive finite element methods for optimal control of partial differential equations: Basic concept. *SIAM J. Control Optim.*, 39:113–132, 2000.

[3] L. Beilina. Adaptive finite element method for a coefficient inverse problem for the Maxwell's system. *Appl. Anal.*, 90:1461–1479, 2011.

[4] L. Beilina and M.V. Klibanov. A posteriori error estimates for the adaptivity technique for the tikhonov functional and global convergence for a coefficient inverse problem. *Inverse Problems*, 26:045012, 2010.

[5] L. Beilina and M.V. Klibanov. *Approximate Global Convergence and Adaptivity for Coefficient Inverse Problems*. Springer, New York, 2012.

[6] L. Beilina and M.V. Klibanov. The philosophy of the approximate global convergence for multidimensional coefficient inverse problems. *Complex Var. and Elliptic Equ.*, 57:277–299, 2012. ISSN 1747-6933.

[7] L. Beilina, M.V. Klibanov, and M.Yu. Kokurin. Adaptivity with relaxation for ill-posed problems and global convergence for a coefficient inverse problem. *J. Math. Sci.*, 167:279–325, 2010.

[8] L. Beilina, Nguyen T.T., M.V. Klibanov, and J.B. Malmberg. Reconstruction of shapes and refractive indices from backscattering experimental data using the adaptivity. *Inverse Problems*, 30:105007, 2014.

[9] L. Beilina, Nguyen T.T., M.V. Klibanov, and J.B. Malmberg. Globally convergent and adaptive finite element methods in imaging of buried objects from experimental backscattering radar measurements. *J. Comput. Appl. Math.*, 2014. ISSN 0377-0427. doi: http://dx.doi.org/10.1016/j.cam.2014.11.055. Article in press: http://dx.doi.org/10.1016/j.cam.2014.11.055.

[10] M. Bellassoued, M. Cristofol, and E. Soccorsi. Inverse boundary value problem for the dynamical heterogeneous Maxwell's system. *Inverse Problems*, 28:095009, 2012.

[11] A.L. Bukhgeĭm and M.V. Klibanov. Uniqueness in the large of a class of multidimensional inverse problems. *Dokl. Akad. Nauk SSSR*, 260(2):269–272, 1981. ISSN 0002-3264.

[12] K. Eriksson, D. Estep, P. Hansbo, and C. Johnson. *Computational Differential Equations*. Studentlitteratur, Lund, 1996.

[13] C. Johnson and A. Szepessy. Adaptive finite element methods for conservation laws based on a posteriori error estimates. *Comm. Pure Appl. Math.*, 48:199–234, 1995.

[14] M.V. Klibanov. Uniqueness of the solution of two inverse problems for a Maxwell system. *Zh. Vychisl. Mat. i Mat. Fiz.*, 26(7):1063–1071, 1119, 1986.

[15] K. Kraft and S. Larsson. The dual weighted residuals approach to optimal control of ordinary differential equations. *BIT*, 50(3):587–607, 2010. ISSN 0006-3835. doi: 10.1007/s10543-010-0270-8. URL `http://dx.doi.org/10.1007/s10543-010-0270-8`.

[16] O.A. Ladyzhenskaya. *The boundary value problems of mathematical physics*, volume 49 of *Applied Mathematical Sciences*. Springer-Verlag, New York, 1985. ISBN 0-387-90989-3. doi: 10.1007/978-1-4757-4317-3. URL `http://dx.doi.org/10.1007/978-1-4757-4317-3`. Translated from the Russian by Jack Lohwater [Arthur J. Lohwater].

[17] S. Li. An inverse problem for Maxwell's equations in bi-isotropic media. *SIAM J. Math. Anal.*, 37:1027–1043, 2005.

[18] S. Li and M. Yamamoto. An inverse problem for Maxwell's equations in anisotropic media. *Chin. Ann. Math. Ser. B*, 28(1):35–54, 2007.

[19] J.B. Malmberg. *A posteriori error estimate in the Lagrangian setting for an inverse problem based on a new formulation of Maxwell's system*, volume 120 of *Springer Proceedings in Mathematics and Statistics*, pages 42–53. Springer, 2015.

[20] A.N. Tikhonov, A.V. Goncharsky, V.V. Stepanov, and A.G. Yagola. *Numerical Methods for the Solution of Ill-Posed Problems*. Kluwer Academic Publishers, Dordrecht, 1995.

Paper III

Reprinted from Larisa Beilina, Nguyen Trung Thành, Michael V. Klibanov and John Bondestam Malmberg, Reconstruction of shapes and refractive indices from backscattering experimental data using the adaptivity, *Inverse problems* 30:105007, 2014, with permission from the publisher.

Reconstruction of shapes and refractive indices from backscattering experimental data using the adaptivity

Larisa Beilina[1], Nguyen Trung Thành[2],
Michael V. Klibanov[3], John Bondestam Malmberg[4]

Abstract. We consider the inverse problem of the reconstruction of the spatially distributed dielectric constant $\varepsilon_r(\mathbf{x})$, $\mathbf{x} \in \mathbb{R}^3$, which is an unknown coefficient in the Maxwell's equations, from time-dependent backscattering experimental radar data associated with a single source of electric pulses. The refractive index is $n(\mathbf{x}) = \sqrt{\varepsilon_r(\mathbf{x})}$. The coefficient $\varepsilon_r(\mathbf{x})$ is reconstructed using a two-stage reconstruction procedure. In the first stage an approximately globally convergent method proposed is applied to get a good first approximation of the exact solution. In the second stage a locally convergent adaptive finite element method is applied, taking the solution of the first stage as the starting point of the minimization of the Tikhonov functional. This functional is minimized on a sequence of locally refined meshes. It is shown here that all three components of interest of targets can be simultaneously accurately imaged: refractive indices, shapes and locations.

Keywords: Coefficient inverse problem, finite element method, globally convergent method, experimental backscattered data.

AMS classification codes: 65N15, 65N30, 35J25.

1. Introduction

In this paper we investigate the problem of imaging objects placed in air from time-dependent backscattering radar measurements, using a

[1]Corresponding author. Department of Mathematical Sciences, Chalmers University of Technology and University of Gothenburg, SE-412 96 Gothenburg, Sweden. E-mail: larisa@chalmers.se

[2]Department of Mathematics & Statistics, University of North Carolina at Charlotte, Charlotte, NC, USA. E-mail: tnguy152@uncc.edu

[3]Department of Mathematics & Statistics, University of North Carolina at Charlotte, Charlotte, NC, USA. E-mail: mklibanv@uncc.edu

[4]Department of Mathematical Sciences, Chalmers University of Technology and University of Gothenburg, SE-412 96 Gothenburg, Sweden. E-mail: john.bondestam.malmberg@chalmers.se

two-stage reconstruction method. In the first stage, initial images are calculated using the globally convergent method for Coefficient Inverse Problems (CIPs), which was originated in [4] with a number of follow up publications; results were summarized in the book [6]. In the second stage, those images are refined using an adaptive finite element method (adaptivity) of [10]. Results of the first stage for the data sets considered in this paper were presented in [8, 28]. Here, we present the results of the second stage. Only the maximum value of the dielectric constant and the location of a target were accurately reconstructed in [8, 28] using the globally convergent method. The accuracy of the reconstruction of the shape of the target was limited. Using the two-stage reconstruction procedure, it is shown here that we can simultaneously and accurately reconstruct all three components of interest of objects: refractive indices, shapes, and locations.

We reconstruct these three components simultaneously as parts of an unknown coefficient, which is the spatially varying dielectric constant $\varepsilon_r(\mathbf{x})$, $\mathbf{x} \in \mathbb{R}^3$, in the Maxwell's equations. Below $\mathbf{x} = (x, y, z) \in \mathbb{R}^3$, where x is the horizontal axis, y is the vertical axis and z is the axis which points from the target towards the measurement plane, see Figure 1. Even though only one component E_2 of the electric field $E = (E_1, E_2, E_3)$ was measured by our experimental device, we numerically solve here a CIP for the three-dimensional (3-d) Maxwell's equations. The boundary data for two other components E_1, E_3 are obtained via computational simulations.

Experimental data were collected by a microwave device which was recently assembled at the University of North Carolina at Charlotte, USA. Our desired application is imaging of explosives. In this paper we consider only targets located in air. The work on real data for the case when targets are buried under the ground is reported in [29]. Note that explosives may be located in air [18], e.g., improvised explosive devices (IEDs). We image both homogeneous and heterogeneous targets. Heterogeneous targets model IEDs.

To collect those data, a single location of the source of electric pulses was used. Hence, we used the minimal amount of the information. The use of more sources was both hard to arrange experimentally and undesirable for our target application. The backscattering time dependent signal was measured at a number of detectors covering a part of a plane, i.e., over a narrow range of backscattering angles, see Figure 1. That plane

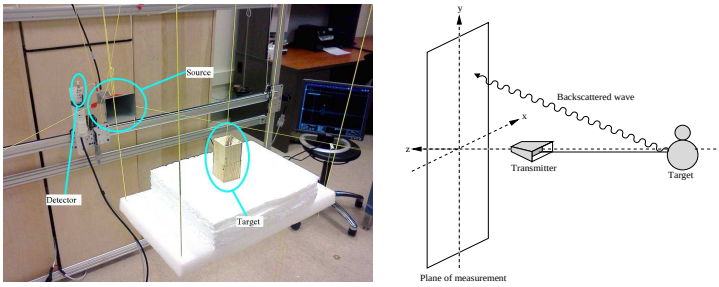

(A) (B)

FIGURE 1. (a): Experimental setup; (b) Our data collection scheme.

was placed behind the source. Experimental data of this paper were collected for targets located in air on the distance of 80 centimeters from the measurement plane, which is 20 wavelengths, i.e., in a far field zone. The distance between neighboring detectors was 2 centimeters.

We refer to, e.g., [20, 21] for treatments of experimental data in the frequency domain by other numerical methods for CIPs for Maxwell's equations. In particular, blind real data were considered in [21]. As to the adaptivity technique for inverse problems, we refer to, e.g., [11, 22]. There are many works dedicated to inverse problems of shape reconstruction; we refer to some most recent ones, e.g., [23, 24, 30, 31]. We also refer to [15] for a survey about inverse problems of shape reconstruction.

An outline of this paper is as follows. In section 2 we describe the two-stage reconstruction procedure. In section 3 we state the forward and inverse problems. In section 4 we present Tikhonov functional and optimality conditions. In section 5 we describe the finite element method used in our computation. In section 6 we present the mesh refinement recommendation and the adaptive algorithm. Some details of numerical implementation are described in section 7. In section 8 we present reconstruction results. Finally, a summary is given in section 9.

2. Two-stage reconstruction procedure

In [8, 28] we have considered the problem of the reconstruction of the spatially distributed dielectric constant $\varepsilon_r(\mathbf{x}), \mathbf{x} \in \mathbb{R}^3$ from experimental data, which were the same as in the current paper. In [8, 28] this function

was the unknown coefficient in a wave-like PDE

$$\varepsilon_r(\mathbf{x})\frac{\partial^2 E_2}{\partial t^2} = \Delta E_2. \tag{2.1}$$

To reconstruct $\varepsilon_r(\mathbf{x})$, we have used the approximately globally convergent algorithm of [6]. The notion of the approximate global convergence ("global convergence" in short) was introduced in [6, 7]. Indeed, conventional least squares cost functionals for CIPs are non convex and typically have many local minima. Hence, given a CIP, the first question to address in its numerical treatment is: *How to obtain a good approximation for the exact solution without any a priori knowledge of a small neighborhood of this solution?* We call a numerical method addressing this question *globally convergent*.

It is well known that it is tremendously difficult to address this question. For this reason, a certain reasonable approximation was made in [6, 7]. This approximation is used only on the first iteration of that method. Because of this approximation, we call the technique of [6, 7] approximately globally convergent. Due to that approximation, a room is left for a refinement of results.

An important point here is that there exists a rigorous guarantee within the framework of that approximate model that the solution resulting from the globally convergent method is located in a small neighborhood of the exact solution. This is achieved without any a priori knowledge of a small neighborhood of the exact solution. Thus, a locally convergent numerical method can be used for a refinement of the solution obtained by the globally convergent technique of [6, 7].

The latter is the main goal of the current paper. We synthesize here the adaptive finite element method of [10] with the globally convergent numerical method of [6] in order to improve the reconstruction of shapes of objects imaged in [8, 28]. The idea of this synthesis was first introduced in [5]. The synthesis represents the following two-stage reconstruction procedure:

Stage 1. In this stage the approximately globally convergent method of [6] is applied and a good first approximation for the exact solution is obtained.

Stage 2. This stage refines the solution obtained in the first stage. The locally convergent adaptivity technique of [10] is applied. The solution obtained in [8, 28] in the first stage is taken as the starting point in the minimization procedure of the Tikhonov functional.

An important advantage of using the two-stage reconstruction procedure follows from Theorem 1.9.1.2 of [6]. This theorem states that the minimizer of the Tikhonov functional (i.e., the regularized solution) is closer to the exact solution than the first guess, provided, however, that the first guess is sufficiently close to the exact solution. Therefore, that first guess should be delivered by the globally convergent method of the first stage. The adaptive finite element method of [10], which we use in the second stage, minimizes the Tikhonov functional on a sequence of locally refined meshes, which is the main attractive point of the adaptivity. It enables one to maintain a reasonable compromise between not using an exceedingly large number of finite elements and a good accuracy of the resulting solution. It follows from Theorem 4.9.3 of [6] and Theorem 5.2 of [3] that if the first guess is sufficiently close to the exact solution, then the accuracy of its reconstruction monotonically improves with local mesh refinements. On the other hand, it was shown in section 5.8.4 of the book [6] that a locally convergent numerical method taken alone does not work for transmitted time dependent experimental data generated by a single source. The same conclusion was drawn for a different type of experimental data in [25].

3. Statement of Forward and Inverse Problems

We model the electromagnetic wave propagation in an isotropic, non-magnetic space $\mathbb{R}^3$ with the dielectric constant coefficient $\varepsilon_r(\mathbf{x})$. The electric field $E = (E_1, E_2, E_3)$ satisfies the following Cauchy problem:

$$\begin{aligned} \varepsilon_r(\mathbf{x})\frac{\partial^2 E}{\partial t^2} + \nabla \times (\nabla \times E) &= (0, \delta(z - z_0)f(t), 0), \text{ in } \mathbb{R}^3 \times (0, T), \\ E(\mathbf{x}, 0) = 0,\ E_t(\mathbf{x}, 0) &= 0 \text{ in } \mathbb{R}^3. \end{aligned} \tag{3.1}$$

where $f(t) \not\equiv 0$ is the time-dependent waveform of the component E_2 of the incident plane wave, which is originated at the plane $\{z = z_0\}$ and propagates along the z-axis. In our experiment the component E_2 corresponds to the electromagnetic pulse which is sent into the medium. Thus, in (3.1) as well as in our computer simulations of section 7 the incident field has only one non-zero component $E_2(\mathbf{x}, t)$. This component propagates along the z-axis until it reaches the target, where it is scattered.

Let $\Omega \subset \mathbb{R}^3$ be a convex bounded domain. We impose the following conditions on the coefficient $\varepsilon_r(\mathbf{x})$:

$$\varepsilon_r(\mathbf{x}) \in C^\alpha\left(\mathbb{R}^3\right), \varepsilon_r(\mathbf{x}) \in [1, d],\ \varepsilon_r(\mathbf{x}) = 1 \text{ for } \mathbf{x} \in \mathbb{R}^3 \setminus \Omega, \tag{3.2}$$

where $d = const. > 1$. We a priori assume the knowledge of the constant d. This means the knowledge of the set of admissible coefficients in (3.2). However, we do not impose small-value assumptions on the unknown coefficient $\varepsilon_r(\mathbf{x})$, i.e., we do not assume that d is small. Here $C^\alpha, \alpha \in (0,1)$, is the Hölder space. Let $\Gamma \subset \partial\Omega$ be the part of the boundary $\partial\Omega$ on which the backscattered data are measured.

Coefficient Inverse Problem (CIP): *Suppose that the coefficient* $\varepsilon_r(\mathbf{x})$ *satisfies conditions (3.2) and that* $\overline{\Omega} \cap \{z = z_0\} = \varnothing$. *Determine the function* $\varepsilon_r(\mathbf{x})$ *for* $\mathbf{x} \in \Omega$, *assuming that the following function* $g(\mathbf{x}, t)$ *is known for a single incident plane wave*

$$g(\mathbf{x}, t) = E(\mathbf{x}, t), \forall (\mathbf{x}, t) \in \Gamma \times (0, \infty). \tag{3.3}$$

This is a 3-d CIP with the data generated by a single measurement event. It is well known that currently uniqueness theorems for such CIPs can be proved only by the method of Carleman estimates, which was originated in [13] with many follow up publications, see, e.g. the recent survey in [17]. This method works only for the case when in the forward problem either at least one of initial conditions or the right hand side at $\{t = 0\}$ does not vanish in the entire domain of interest $\overline{\Omega}$. However, the latter is obviously not true in our case. On the other hand, because of our target application mentioned above, it makes sense to solve this CIP numerically using experimental data. Therefore, we simply assume below that uniqueness of our CIP holds.

3.1. Domain decomposition finite element/finite difference method. It is impossible to solve the problem (3.1) in the whole space $\mathbb{R}^3$. Hence, we solve it in a bounded domain G which contains our domain of interest Ω. For the convenience of our local mesh refinement procedure, we use the domain decomposition finite element/finite difference method of [9]. For this purpose, we decompose G as $G = \Omega_{FEM} \cup \Omega_{FDM}$ with $\Omega_{FEM} = \Omega$. Here we use a finite element mesh in Ω_{FEM}, and in Ω_{FDM} we use a finite difference mesh. These two domains have a thin layer of structured overlapping nodes where we use an exchange procedure between computational solutions obtained by finite element and finite difference methods, see details in [9]. By (3.2)

$$\begin{aligned} &\varepsilon_r(\mathbf{x}) \geq 1, \text{ for } \mathbf{x} \in \Omega_{FEM}, \\ &\varepsilon_r(\mathbf{x}) = 1, \text{ for } \mathbf{x} \in \Omega_{FDM}. \end{aligned} \tag{3.4}$$

In our computation we use the following model problem in the computational domain G for the electric field E with the stabilizing divergence condition [1] with $s \geq 1$ and with boundary conditions specified in this section below:

$$\varepsilon_r \frac{\partial^2 E}{\partial t^2} + \nabla \times (\nabla \times E) - s\nabla(\nabla \cdot (\varepsilon_r E)) = 0, \text{ in } G \times (0,T), \tag{3.5}$$

$$E(\mathbf{x},0) = 0, \; E_t(\mathbf{x},0) = 0 \text{ in } G. \tag{3.6}$$

For simplicity, we choose the domains Ω and G by

$$\Omega = \Omega_{FEM} = \{\mathbf{x} = (x,y,z) : -a < x < a, -b < y < b, -c < z < c_1\}, \tag{3.7}$$

$$G = \{\mathbf{x} = (x,y,z) : -X < x < X, -Y < y < Y, -Z < z < z_0\}, \tag{3.8}$$

with positive numbers $a, b, c, \; X > a, \; Y > b, \; -Z < -c < c_1 < z_0$ and $\Omega_{FDM} = G \setminus \Omega_{FEM}$. Denote by

$$\begin{aligned} &\partial_1 G := \overline{G} \cap \{z = z_0\}, \quad \partial_2 G := \overline{G} \cap \{z = -Z\}, \\ &\partial_3 G := \partial G \setminus (\partial_1 G \cup \partial_2 G). \end{aligned} \tag{3.9}$$

The backscattering side of Ω is $\Gamma = \partial\Omega \cap \{z = c_1\}$. Next, define $\partial_i G_T := \partial_i G \times (0,T), i = 1,2,3$. Let $t_1 \in (0,T)$ be a number, and we assume that the function $f(t) \in C[0,t_1]$ and $f(t) = 0$, for $t > t_1$. We impose the following boundary conditions

$$E(\mathbf{x},t) = (0, f(t), 0) \text{ on } \partial_1 G \times (0,t_1], \tag{3.10}$$

$$\partial_n E(\mathbf{x},t) = -\partial_t E(\mathbf{x},t) \text{ on } \partial_1 G \times (t_1,T), \tag{3.11}$$

$$\partial_n E(\mathbf{x},t) = -\partial_t E(\mathbf{x},t) \text{ on } \partial_2 G_T, \tag{3.12}$$

$$\partial_n E(\mathbf{x},t) = 0 \text{ on } \partial_3 G_T, \tag{3.13}$$

where ∂_n is the normal derivative. Conditions (3.11), (3.12) are first order absorbing boundary conditions [14] at the planes $\partial_1 G$ and $\partial_2 G$ of the rectangular prism G, and (3.13) is the zero Neumann condition at the lateral part $\partial_3 G$ of the boundary ∂G. Condition (3.10) means that the incident plane wave is emitted only up to the time $t = t_1$ and then propagates inside of the domain G.

It was demonstrated numerically in [9] that the solution of the problem (3.5)–(3.13) approximates well the solution of the original Maxwell's equations for $s = 1$. The energy estimate of Theorem 4.1 of [9] guarantees the stability of the forward problem (3.5)–(3.13) for $s \geq 1$.

Using the transformation $\nabla \times (\nabla \times E) = \nabla(\nabla \cdot E) - \nabla \cdot (\nabla E)$, the model problem (3.5), (3.6), (3.10) – (3.13) can be rewritten as

$$\varepsilon_r \frac{\partial^2 E}{\partial t^2} + \nabla(\nabla \cdot E)$$

$$- \nabla \cdot (\nabla E) - s\nabla(\nabla \cdot (\varepsilon_r E)) = 0, \qquad \text{in } G \times (0,T), \tag{3.14}$$

$$E(\mathbf{x},0) = 0,\ E_t(\mathbf{x},0) = 0 \qquad \text{in } G, \tag{3.15}$$

$$E(\mathbf{x},t) = (0, f(t), 0) \qquad \text{on } \partial_1 G \times (0,t_1], \tag{3.16}$$

$$\partial_n E(\mathbf{x},t) = -\partial_t E(\mathbf{x},t) \qquad \text{on } \partial_1 G \times (t_1,T), \tag{3.17}$$

$$\partial_n E(\mathbf{x},t) = -\partial_t E(\mathbf{x},t) \qquad \text{on } \partial_2 G_T, \tag{3.18}$$

$$\partial_n E(\mathbf{x},t) = 0 \qquad \text{on } \partial_3 G_T. \tag{3.19}$$

We refer to [9] for details of the numerical solution of the forward problem (3.14)-(3.19).

4. Tikhonov functional and optimality conditions

Let Γ_1 be the extension of the backscattering side Γ up to the boundary $\partial_3 G$ of the domain G, i.e.,

$$\Gamma_1 = \{\mathbf{x} = (x,y,z) : -X < x < X, -Y < y < Y, z = c_1\}. \tag{4.1}$$

Let G_b be the part of the rectangular prism G which lies between the two planes Γ_1 and $\{z = -Z\}$:

$$G_b = \{\mathbf{x} = (x,y,z) : -X < x < X, -Y < y < Y, -Z < z < c_1\}. \tag{4.2}$$

Denote by $Q_T = G_b \times (0,T)$, $S_T = \partial G_b \times (0,T)$. Even though we have the data $g(\mathbf{x},t)$ in (3.3) only on Γ, we show in subsection 7.3.3 below how we complement these data on the rest of the boundary ∂G_b of the domain G_b, i.e., on $\partial G_b \setminus \Gamma$. This way we approximately obtain the function $\widetilde{g}(\mathbf{x},t)$:

$$\widetilde{g}(\mathbf{x},t) = E(\mathbf{x},t), \forall (\mathbf{x},t) \in S_T. \tag{4.3}$$

We reformulate our inverse problem as an optimization problem. Thus, we find ε_r by minimizing the Tikhonov functional:

$$F(E,\varepsilon_r) := \frac{1}{2}\int_{S_T} (E - \tilde{g})^2 z_\delta(t) d\mathbf{x} dt + \frac{1}{2}\gamma \int_G (\varepsilon_r - \varepsilon_{r\,glob})^2 \, d\mathbf{x}, \tag{4.4}$$

where $\gamma > 0$ is the regularization parameter, and $\varepsilon_{r,glob}(\mathbf{x})$ is the computed coefficient via the globally convergent method.

Let $E_{glob}(\mathbf{x},t)$ be the solution of the forward problem (3.14)–(3.19) with $\varepsilon_r(\mathbf{x}) := \varepsilon_{r,glob}(\mathbf{x})$. Denote by $p(\mathbf{x},t) = \partial_n E_{glob}(\mathbf{x},t) \mid_{S_T}$. In addition to the Dirichlet condition (4.3), we set the Neumann boundary condition as

$$\partial_n E(\mathbf{x},t) = p(\mathbf{x},t), \forall (\mathbf{x},t) \in S_T. \tag{4.5}$$

To formulate the Fréchet derivative of the Tikhonov functional (4.4) (see formula (4.16) below), we make use of the adjoint method. This method is based on the state and adjoint problems. The state problem in the domain G_b is given by

$$\varepsilon_r \frac{\partial^2 E}{\partial t^2} + \nabla(\nabla \cdot E) - \nabla \cdot (\nabla E) - s\nabla(\nabla \cdot (\varepsilon_r E)) = 0, \quad \text{in } Q_T, \tag{4.6}$$

$$E(\mathbf{x},0) = 0,\ E_t(\mathbf{x},0) = 0 \quad \text{in } G_b, \tag{4.7}$$

$$\partial_n E(\mathbf{x},t) = p(\mathbf{x},t) \quad \text{on } S_T. \tag{4.8}$$

The adjoint problem is:

$$\varepsilon_r \frac{\partial^2 \lambda}{\partial t^2} + \nabla(\nabla \cdot \lambda) - \nabla \cdot (\nabla \lambda) - s\varepsilon_r \nabla(\nabla \cdot \lambda) = 0, \quad \text{in } Q_T, \tag{4.9}$$

$$\lambda(\mathbf{x},T) = 0,\ \lambda_t(\mathbf{x},T) = 0 \quad \text{in } G_b, \tag{4.10}$$

$$\partial_n \lambda(\mathbf{x},t) = z_\delta(t)(\widetilde{g} - E)(\mathbf{x},t) \quad \text{on } S_T. \tag{4.11}$$

Here, $z_\delta(t)$ is used to ensure the compatibility conditions at $\overline{Q}_T \cap \{t = T\}$ for the adjoint problem and $\delta > 0$ is a small number. The function $z_\delta(t)$ is chosen such that

$$z_\delta \in C^\infty[0,T],\ z_\delta(t) = \begin{cases} 1 & \text{for} t \in [0, T-\delta], \\ 0 & \text{for } t \in \left(T - \frac{\delta}{2}, T\right], \\ 0 < z_\delta < 1 & \text{for } t \in \left(T-\delta, T-\frac{\delta}{2}\right), \end{cases}$$

Weak solutions $E, \lambda \in H^1(Q_T)$ to problems (4.6)–(4.8) and (4.9)–(4.11) are defined similarly with the case of only one hyperbolic equation in Chapter 4 of the book [19], also see formula (34) in [9]. The weak solution to the state problem (4.6)-(4.8) is the solution to the following

equation:

$$\begin{aligned}
&\int_{Q_T}(-\varepsilon_r\frac{\partial E}{\partial t}\frac{\partial v}{\partial t})\ d\mathbf{x}dt-\int_{Q_T}(\nabla\cdot E)(\nabla\cdot v)\ d\mathbf{x}dt\\
&+\int_{Q_T}(\nabla E)(\nabla v)\ d\mathbf{x}dt+s\int_{Q_T}(\nabla\cdot(\varepsilon_r E))(\nabla\cdot v)\ d\mathbf{x}dt\\
&-\int_{\partial S_T}vp\ d\sigma dt=0,\ \forall v\in H^1\left(Q_T\right),v\left(x,T\right)=0,
\end{aligned}\tag{4.12}$$

The weak solution to the adjoint problem (4.9)-(4.11) is the solution to the following equation:

$$\begin{aligned}
&-\int_{S_T}(\tilde{g}-E)\ w\ z_\delta\ d\sigma dt-\int_{Q_T}\varepsilon_r\frac{\partial\lambda}{\partial t}\frac{\partial w}{\partial t}\ d\mathbf{x}dt\\
&-\int_{Q_T}(\nabla\cdot\lambda)(\nabla\cdot w)\ d\mathbf{x}dt+\int_{Q_T}(\nabla\lambda)(\nabla w)\ d\mathbf{x}dt\\
&+s\int_{Q_T}(\nabla\cdot\lambda)(\nabla\cdot(\varepsilon_r w))\ d\mathbf{x}dt,\ \forall w\in H^1\left(Q_T\right),w\left(x,0\right)=0.
\end{aligned}\tag{4.13}$$

Introduce the following spaces of real valued vector functions

$$\begin{aligned}
H_E^1(Q_T)&=\left\{f\in[H^1(Q_T)]^3:f(\mathbf{x},0)=0\right\},\\
H_\lambda^1(Q_T)&=\left\{f\in[H^1(Q_T)]^3:f(\mathbf{x},T)=0\right\},\\
U^1&=H_E^1\left(G_T\right)\times H_\lambda^1\left(G_T\right)\times B\left(G\right),
\end{aligned}$$

where $B\left(G\right)$ is the space of functions bounded on G with the norm $\|f\|_{B(G)}=\sup_G|f|$. To minimize the functional (4.4) we introduce the Lagrangian

$$\begin{aligned}
L(E,\lambda,\varepsilon_r)&=F(E,\varepsilon_r)-\int_{Q_T}\varepsilon_r\frac{\partial\lambda}{\partial t}\frac{\partial E}{\partial t}\ d\mathbf{x}dt\\
&-\int_{Q_T}(\nabla\cdot E)(\nabla\cdot\lambda)\ d\mathbf{x}dt+\int_{Q_T}(\nabla E)(\nabla\lambda)\ d\mathbf{x}dt\\
&+s\int_{Q_T}(\nabla\cdot(\varepsilon_r E))(\nabla\cdot\lambda)\ d\mathbf{x}dt-\int_{\partial S_T}\lambda p\ d\sigma dt,
\end{aligned}\tag{4.14}$$

where E and λ are weak solutions of problems (4.6)-(4.8) and (4.9)-(4.11), respectively.

Clearly, (4.12) implies that the sum of integral terms in (4.14) equals zero. Hence, $L\left(E,\lambda,\varepsilon_r\right)=F\left(E,\varepsilon_r\right)$. In (4.14) $\left(E,\lambda,\varepsilon_r\right)=w\in U^1$ and

functions E and λ depend on the coefficient ε_r. To get the Fréchet derivative L' of the Lagrangian (4.14) rigorously, one should assume that variations of functions u and λ depend on variations of the coefficient ε_r, similarly with section 4.8 of [6], and we will do that in our future publications. In this work, to derive the Fréchet derivative of the Lagrangian (4.14) we assume for brevity that in (4.14) the vector function $(E, \lambda, \varepsilon_r)$ can be varied independently of each other. Thus, we search a point $w \in U^1$ such that

$$L'(w)(\overline{w}) = 0, \ \forall \overline{w} \in U^1. \tag{4.15}$$

To find the Fréchet derivative $L'(w)$, we consider $L(w+\overline{w}) - L(w)$, $\forall \overline{w} \in U^1$ and single out the linear, with respect to $\overline{w}$, part of the obtained expression. Thus, using (4.12), (4.13) and (4.4), we obtain

$$\begin{aligned} L'(w)(\mathbf{x}) = \gamma(\varepsilon_r - \varepsilon_{r,glob})(\mathbf{x}) - \int_0^T \frac{\partial \lambda}{\partial t} \frac{\partial E}{\partial t}(\mathbf{x}, t)\, dt \\ + s \int_0^T (\nabla \cdot E)(\nabla \cdot \lambda)(\mathbf{x}, t)\, dt, \mathbf{x} \in G_b. \end{aligned} \tag{4.16}$$

5. Finite element discretization

Consider a partition $K_h = \{K\}$ of G_b which consists of tetrahedra with a mesh function h defined as $h|_K = h_K$ — the local diameter of the element K. Let $J_\tau = \{J\}$ be a partition of the time interval $(0, T)$ into subintervals $J = (t_{k-1}, t_k]$ of uniform length $\tau = t_k - t_{k-1}$. We also assume the minimal angle condition on the K_h [12].

To formulate the finite element method for solving the state problem (4.6)–(4.8) and the adjoint problem (4.9)–(4.11), and to compute the gradient of the Lagrangian via (4.16), we define the finite element spaces $V_h \subset L_2(G_b)$, $W_h^E \subset H_E^1(Q_T)$ and $W_h^\lambda \subset H_\lambda^1(Q_T)$. First, we introduce the finite element trial space W_h^E for every component of the electric field E defined by

$$W_h^E := \{w \in H_E^1 : w|_{K \times J} \in P_1(K) \times P_1(J), \forall K \in K_h, \forall J \in J_\tau\},$$

where $P_1(K)$ and $P_1(J)$ denote the set of linear functions on K and J, respectively. We also introduce the finite element test space W_h^λ defined by

$$W_h^\lambda := \{w \in H_\lambda^1 : w|_{K \times J} \in P_1(K) \times P_1(J), \forall K \in K_h, \forall J \in J_\tau\}.$$

Hence, the finite element spaces W_h^E and W_h^λ consist of continuous piecewise linear functions in space and time. To approximate the function $\varepsilon_r(\mathbf{x})$, we use the space of piecewise constant functions $V_h \subset L_2(\Omega)$,

$$V_h := \{u \in L_2(\Omega) : u|_K \in P_0(K), \forall K \in K_h\}, \tag{5.1}$$

where $P_0(K)$ is the set of piecewise constant functions on K. In our computations we truncate computed functions $\varepsilon_r(\mathbf{x})$ to unity outside of the domain $\Omega_{FEM} = \Omega$ using (3.4) as

$$\overline{\varepsilon}_r(\mathbf{x}) = \begin{cases} \varepsilon_r(\mathbf{x}), \mathbf{x} \in \Omega_{FEM}, \\ 1, \mathbf{x} \in \Omega_{FDM}. \end{cases} \tag{5.2}$$

Next, we set $U_h = W_h^E \times W_h^\lambda \times V_h$. Obviously $\dim U_h < \infty$ and $U_h \subset U^1$ as a set. Because of this, we consider U_h as a discrete analogue of the space U^1. We introduce the same norm in U_h as the one in U^0, $\|\cdot\|_{U_h} := \|\cdot\|_{U^0}$, with

$$U^0 = L_2(G_T) \times L_2(G_T) \times L_2(\Omega).$$

The finite element method for solving equation (4.15) now reads: *Find* $u_h \in U_h$*, such that*

$$L'(u_h)(\bar{u}) = 0, \ \forall \bar{u} \in U_h. \tag{5.3}$$

6. Mesh refinement recommendation and the adaptive algorithm

From Theorem 5.1 and Remark 5.1 of [10] it follows that the finite element mesh should be locally refined in such subdomain of Ω where the maximum norm of the Frëchet derivative of the objective functional is large. For each mesh we first linearly interpolate the coefficient $\varepsilon_{r,glob}(\mathbf{x})$ on it, and use the interpolated coefficient as an initial guess for on the current mesh. Our algorithm consists of two loops: the outer loop deals with the locally adaptive mesh refinement. In the inner loop, i.e., on each mesh, we iteratively update the approximations ε_h^m of the function ε_h by solving (4.15) using an optimization procedure, where m is the iteration index in the optimization procedure. Denote

(6.1)

$$L_h'^{,m}(\mathbf{x}) = -\int_0^T \frac{\partial \lambda_h^m}{\partial t} \frac{\partial E_h^m}{\partial t} \, dt + s \int_0^T \nabla \cdot E_h^m \nabla \cdot \lambda_h^m dt + \gamma(\bar{\varepsilon_h}^m - \bar{\varepsilon}_{r,glob}).$$

Adaptive algorithm

- Step 0. Choose an initial mesh K_h in Ω and an initial time partition J_0 of the time interval $(0,T)$. Start from the initial guess $\varepsilon_h^0 = \varepsilon_{r,glob}$, we compute the approximations ε_h^m via the following steps:
- Step 1. Compute the solutions $E_h(x,t,\varepsilon_h^m)$ and $\lambda_h(x,t,\varepsilon_h^m)$ of the state problem (3.14)–(3.17) and the adjoint problem (4.9)–(4.11) on K_h and J_k, and compute the Frëchet derivative $L_h'^{,m}$ via (6.1).
- Step 2. Update the coefficient on K_h and J_k using the conjugate gradient method:

$$\varepsilon_h^{m+1} := \varepsilon_h^m + \alpha d^m(\mathbf{x}),$$

where $\alpha > 0$ is a step-size in the conjugate gradient method, given by a line search procedure, see, e.g., [26], and

$$d^m(\mathbf{x}) = -L_h'^{,m}(\mathbf{x}) + \beta^m d^{m-1}(\mathbf{x}),$$

with

$$\beta^m = \frac{||L_h'^{,m}||^2}{||L_h'^{,m-1}||^2},$$

where $d^0(\mathbf{x}) = -L_h'^{,0}(\mathbf{x})$.

- Step 3. Stop updating the coefficient and set $\varepsilon_h := \varepsilon_h^{m+1}$, $M := m+1$, if either $||L_h'^{,m}||_{L_2(\Omega)} \le \theta$ or norms $||\varepsilon_h^m||_{L_2(\Omega)}$ are stabilized. Here θ is a tolerance number. Otherwise, set $m := m+1$ and go to step 1.
- Step 4. Compute $L_h'^{,M}$ via (6.1). Refine the mesh at all grid points $\mathbf{x}$ where

$$|L_h'^{,M}(\mathbf{x})| \ge \beta_1 \max_{\overline{\Omega}} |L_h'^{,M}(\mathbf{x})|. \tag{6.2}$$

Here the tolerance number $\beta_1 \in (0,1)$ is chosen by the user.

- Step 5. Construct a new mesh K_h in Ω and a new time partition J_k of the time interval $(0,T)$. On J_k the new time step τ should be chosen in such a way that the CFL condition is satisfied. Interpolate the initial approximation $\varepsilon_{r,glob}$ from the previous mesh to the new mesh. Next, return to step 1 at $m = 1$ and perform all above steps on the new mesh.

- Step 6. Let $\left\|L'^{,M}_{h,prev}\right\|_{L_2(\Omega)}$ and $\left\|L'^{,M}_{h,current}\right\|_{L_2(\Omega)}$ be norms defined in step 4 on the previous and current mesh, respectively. Stop mesh refinements if $\left\|L'^{,M}_{h,current}\right\|_{L_2(\Omega)} \geq \left\|L'^{,M}_{h,prev}\right\|_{L_2(\Omega)}$.

7. Some details of numerical implementation

In this section we present results of reconstruction of dielectric constants/refractive indices and shapes of some targets using the adaptivity algorithm of section 6. One of the discrepancies between our mathematical model (3.14)- (3.19) and the measured experimental data is that formally equation (3.14) is invalid for the case when metallic targets are present (we refer to [8] for the description of other discrepancies). However, it was shown computationally in [18] that one can treat metallic targets as dielectrics with large dielectric constants.

We call these *effective* (or "appearing") dielectric constants and values for them are in the interval

$$\varepsilon_r \,(\text{metallic target}) \in (10, 30)\,. \tag{7.1}$$

Modeling metallic targets as integral parts of the unknown coefficient $\varepsilon_r(\mathbf{x})$ is convenient for our practical computations in order to image IEDs. Since IEDs usually consist of mixtures of some dielectrics with a number of metallic parts, these targets are heterogeneous ones, and we consider three heterogeneous cases in section 8. However, modeling metallic parts separately from dielectric ones is impractical for our application because of those mixtures.

Using (7.1), we define in all our tests the upper value of the function $\varepsilon_r(\mathbf{x})$ as $d = 25$, see (3.2). Thus, we set lower and upper bounds for the reconstructed function $\varepsilon_r(\mathbf{x})$ in Ω as

$$M_{\varepsilon_r} = \{\varepsilon_r(\mathbf{x}) : \varepsilon_r(\mathbf{x}) \in [1, 25]\}. \tag{7.2}$$

In our computation we ensure lower and upper bounds via truncating those values of $\varepsilon_r(\mathbf{x})$ which are outside of the interval (7.2).

Our choice of all parameters in the above adaptive algorithm is optimal for our problem. The regularization parameter γ is chosen such that it gives the smallest reconstruction error given by the relative discrete $L_{2(\Omega)}$ error $e_\varepsilon = ||\varepsilon - \varepsilon_h||/||\varepsilon_h||$. Here, ε is the function ε_r for the calibrating object either for metallic or dielectric targets, and ε_h is the computed function ε_r. We note, that we had one calibrating object

for metallic targets and one calibrating object for dielectric targets, see section 8.

Next, we choose the tolerance number β_1 in (6.2) in a computationally efficient way. If we would choose $\beta_1 \approx 1$, then we would refine the mesh in too narrow regions. On the other hand, if we would choose $\beta_1 \approx 0$, then we would refine the mesh in almost the entire domain Ω, which is inefficient. Hence, the tolerance number β_1 should be chosen numerically. The important point here is that in our computations we choose β_1 in accordance to the obtained reconstruction of the first stage. In other words, to obtain best shape reconstruction results, this parameter is to be chosen such that the refinement will be performed in a regions which are close to the reconstruction obtained on the first stage. In all our tests below the regularization parameter $\gamma = 0.01$ and the tolerance number $\theta = 10^{-9}$ in step 3 of our algorithm. These parameters were chosen computationally. The reason for this choice was the best reconstructions for both calibrating objects which we got with $\gamma = 0.01, \theta = 10^{-9}$.

7.1. Dirichlet and Neumann boundary conditions. In our experiments only one component $E_2(\mathbf{x}, t)$ of the electric field $E(\mathbf{x}, t) = (E_1, E_2, E_3)(\mathbf{x}, t)$ is both sent into the medium and measured. Thus, only the second component of the function g in the Dirichlet boundary condition (3.3) on Γ is available. We approximate the other two components of g on Γ by the numerical solution of the forward problem (3.14)–(3.19), with the coefficient given by $\varepsilon_r = \varepsilon_{r,glob}(\mathbf{x})$ — the solution of the globally convergent method. The Dirichlet data on the rest of the boundary ∂G_b, i.e., on $\partial G_b \setminus \Gamma$, as well as the Neumann condition $p(\mathbf{x}, t)$ in (4.5) at the entire boundary ∂G_b are taken from the numerical solution of that forward problem.

7.2. Computational domains. To generate the boundary data (4.3), (4.5) for all three components of the electric field E, as specified in the previous section, we solve the forward problem in the computational domain G, which we choose as

$$G = \{\mathbf{x} = (x, y, z) \in (-0.56, 0.56) \times (-0.56, 0.56) \times (-0.16, 0.1)\}.$$

The boundary of the domain G is $\partial G = \partial_1 G \cup \partial_2 G \cup \partial_3 G$. Here, $\partial_1 G$ and $\partial_2 G$ are front and back sides of the domain G at $\{z = 0.1\}$ and $\{z = -0.16\}$, respectively, and $\partial_3 G$ is the union of left, right, top and bottom sides of this domain.

We use a stabilized domain decomposition method of [9] implemented in the software package WavES [32]. The FEM domain Ω_{FEM} is chosen as

(7.3)
$$\Omega_{FEM} = \Omega = \{\mathbf{x} =(x, y, z) \in (-0.5, 0.5) \times (-0.5, 0.5) \times (-0.1, 0.04)\}.$$

After the data propagation procedure, see discussions in section 7.3, the data $g(\mathbf{x}, t)$ in (3.3) are given at the front side Γ of the domain Ω which is defined as

$$\Gamma = \{\mathbf{x} \in \partial\Omega : z = 0.04\}. \tag{7.4}$$

The waveform function $f(t)$ in our simulated incident plane wave is chosen as

$$f(t) = \sin \omega t,\ 0 \le t \le t_1 := \frac{2\pi}{\omega}.$$

Here, we initialize the plane wave at $\{z = 0.1\}$. We use $\omega = 30$, $T = 1.2$ and $s = 1$. We solve the problem (3.14)–(3.19) using the explicit scheme of [9] with the time step size $\tau = 0.003$, which satisfies the CFL condition. Note that this time step is dimensionless, which corresponds to the time step of 10 ps in our real experiment. Here we use the dimensionless time step in order to normalize the coefficient ε_r to be unity outside of Ω. The dimensionless time $T = 1.2$ corresponds to 4 ns in our real time. We do not use the whole 10 ns recorded data since after data preprocessing, they are shifted earlier in time and they do not contain any target's signal after 4 ns.

7.3. Data Preprocessing. In the previous section, we implicitly assumed that our model is comparable to the experimental data. Moreover, the data is available at the plane Γ of Ω, which is quite close to the targets. Unfortunately, this is not the case in practice. In fact, there is a huge misfit bewteen our experimental data and the simulated ones, see [28]. Therefore, data preprocessing is required in order to prepares the experimental data to become an input for our inversion algorithm. In our experience, data preprocessing of experimental data is always a heuristic procedure. That procedure for the globally convergent method was described in detail in [28]. Since the globally convergent method works with the PDE which is obtained by the Laplace transform of the original wave-like equation (2.1), and we work here directly in time domain, we

need less number of data preprocessing steps than in [28]. We only describe the following preprocessing steps which are different from those of [28].

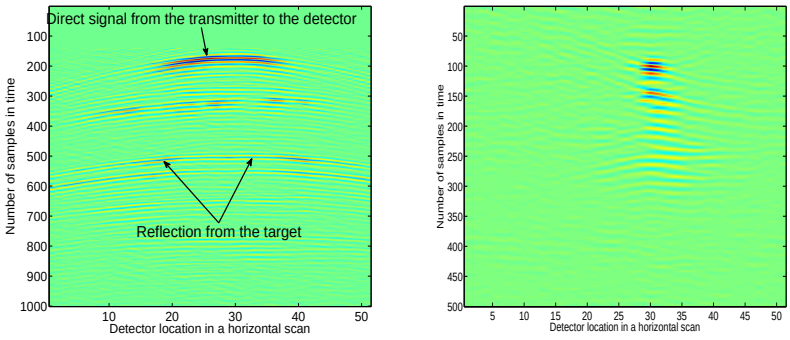

(A) (B)

FIGURE 2. Result of data propagation for target number 1 (Table 1). Horizontal axis is the indices of the detector's locations and vertical axis is number of samples in time. a) data at the measurement plane, b) data at the propagated plane. One can see that the propagated data are focused at the target, whereas original data are smeared out.

7.3.1. *Data propagation.* In [28], we used a time-reversal data propagation method in order to migrate our data from the measurement plane, which is in the far field zone, to the plane Γ, which is at about 4 cm far from the targets. In this paper, we use another data propagation method based on the Fourier transform. This technique is basically the same as the Stolt migration in Geophysics, see [27, 33]. However, in the standard Stolt migration the wave at the initial time is calculated in the whole spatial domain of interest, whereas we calculate the wave only at a plane parallel to the measurement plane but in the whole time interval. The technique is described in detail in [29].

A result of the data propagation is illustrated in Figure 2. The figure shows a horizontal scan of target number 1, see Table 1. The horizontal axis is the indices of the detector's locations and the vertical axis is the number of samples in time. Time increases from the top to the bottom.

Figure 2(a) shows the original data while Figure 2(b) shows the data after the propagation. As can be seen from these figures, the target's signas in the original data is smeared out. On the other hand, it is focused after the data propagation.

7.3.2. *Data calibration.* Since the amplitude of experimental data are very different from that of computational simulations, we must multiply the experimental data by a calibration factor θ so that they have similar amplitude as the simulated data. This factor is not easy to obtain in practice and we should somehow find an appropriate one. The calibration of the measured data was done in the Laplace transform domain in [28]. However, here we work with the time domain data only. Therefore, we use a new data calibation procedure we described below.

Let the function $g_{\text{exper}}(\mathbf{x},t), \mathbf{x} \in \Gamma, t \in (0,T)$ be our propagated experimental data. This function is given only on grid points $(\mathbf{x}_i, t_j)$. We compute the maximal value of this function,

$$g_{max} = \max_{(\mathbf{x}_i,t_j)} g_{\text{exper}}(\mathbf{x}_i,t_j). \tag{7.5}$$

Usually the number g_{max} is quite large. Next, let $E_{2,sim}(\mathbf{x},t)$ be the function which is computed via solving the problem (3.14)-(3.19). We compute the maximal value of this function on Γ,

$$E_{2,max} = \max_{\Gamma\times[0,T]} E_{2,sim}(\mathbf{x},t).$$

Define $r = E_{2,max}/g_{max}$. Next, we assign

$$g_{incl}(\mathbf{x}_i,t_j) := r \cdot g_{\text{exper}}(\mathbf{x}_i,t_j)$$

and use the function $g_{incl}(\mathbf{x}_i,t_j)$ as the second component of the vector function $g(\mathbf{x},t)$ in (3.3). Two other steps of data preprocessing are due to (4.3) and (4.5) in section 4. The final step of data preprocessing, the so-called "immersing procedure" is done as follows.

7.3.3. *Data immersing.* In this section we describe a heuristic immersing procedure of the time-dependent propagated experimental data $g_{incl}(\mathbf{x},t) = E_2(\mathbf{x},t)\,|_{\mathbf{x}\in\Gamma}$. This procedure does two things:

- immerses the data $g_{incl}(\mathbf{x},t)$ into computationally simulated ones;
- extends the data $g_{incl}(\mathbf{x},t)$ from Γ to Γ_1.

By (7.4) the rectangle Γ is smaller than the rectangle

$$\Gamma_1 = \{\mathbf{x} : (x,y) \in (-0.56,0.56)\times(-0.56,0.56), z = 0.04\}.$$

It is clear from the adjoint problem (4.9)-(4.11) that we need to get a proper data for the function $E_2(\mathbf{x},t)$ for $(\mathbf{x},t) \in \Gamma_1 \times (0,T)$ while having the data $E_2(\mathbf{x},t) = g_{incl}(\mathbf{x},t)$ only for $\mathbf{x} \in \Gamma$. We now describe how do we extend the data from Γ to Γ_1. Let $E_2(\mathbf{x},t)$ be the E_2-component of the solution $E(\mathbf{x},t)$ of the forward problem (3.14–3.19) with $\varepsilon_r := \varepsilon_{r,glob}$. Then we define our immersed function $E_2^{immers}(\mathbf{x},t)$ for $(\mathbf{x},t) \in \Gamma_1 \times (0,T)$ as

(7.6)
$$E_2^{immers}(\mathbf{x},t) = \begin{cases} g_{incl}(\mathbf{x},t), & \text{if } \mathbf{x} \in \Gamma \text{ and } g_{incl}(\mathbf{x},t) \geq \beta \max_{\overline{\Gamma}} g_{incl}(\mathbf{x},t), \\ E_2(\mathbf{x},t), & \text{if } \mathbf{x} \in \Gamma \text{ and } g_{incl}(x,t) < \beta \max_{\overline{\Gamma}} g_{incl}(\mathbf{x},t), \\ E_2(\mathbf{x},t), & \text{if } \mathbf{x} \in \Gamma_1 \setminus \Gamma. \end{cases}$$

We choose the parameter $\beta \in (0,1)$ in (7.6) in numerical experiments of section 8. It follows from (7.6) that $E_2^{immers}(\mathbf{x},t) = E_2(\mathbf{x},t)$ for $\mathbf{x} \in \Gamma_1 \setminus \Gamma$.

Figures 3, 4 show that, depending on the parameter β in (7.6), the data immersing procedure not only allows to extend the data from Γ to $\Gamma_1 \setminus \Gamma$ but also make the experimental data usable in our inverse algorithm. Indeed, we note that the experimental data is measured at a very high frequency, say, $\omega \approx 170$, whereas our simulations are done at $\omega = 30$ in order to reduce the computational cost. Therefore, the experimental data are not compatible with the simulations. Our immersing procedure helps to avoid solving the problem at a very high frequency. After this immersing procedure we solve the inverse problem using the algorithm of section 6.

7.4. Postprocessing of results. Results of the globally convergent algorithm of the first stage procedure have demonstrated that this algorithm provides accurate locations of targets as well as accurate values of refractive indices $n = \sqrt{\varepsilon_r}$ of dielectric targets and large values of appearing dielectric constants ε_r for metallic targets [8, 28]. However, it does not reconstruct shapes of targets well, especially the size in the z-direction. The latter is the reason why we apply the second stage to refine results of the first.

Let $\varepsilon_r(\mathbf{x})$ be the function obtained in the adaptive algorithm of section 6. We form the image of the dielectric targets based on the function $\varepsilon_{r,diel}(\mathbf{x})$,

$$\varepsilon_{r,diel}(\mathbf{x}) = \begin{cases} \varepsilon_r(\mathbf{x}) \text{ if } \varepsilon_r(\mathbf{x}) \geq 0.85 \max_{\overline{\Omega}} \varepsilon_r(\mathbf{x}), \\ 1 \text{ otherwise.} \end{cases} \tag{7.7}$$

As to the metallic targets (i.e., the ones with large computed maximal values of $\varepsilon_r(\mathbf{x})$), we use the function $\varepsilon_{r,metal}(\mathbf{x})$,

$$\varepsilon_{r,metal}(\mathbf{x}) = \begin{cases} \varepsilon_r(\mathbf{x}) & \text{if } \varepsilon_r(\mathbf{x}) \geq 0.3 \max_{\overline{\Omega}} \varepsilon_r(\mathbf{x}), \\ 1 & \text{otherwise.} \end{cases} \tag{7.8}$$

8. Reconstruction results

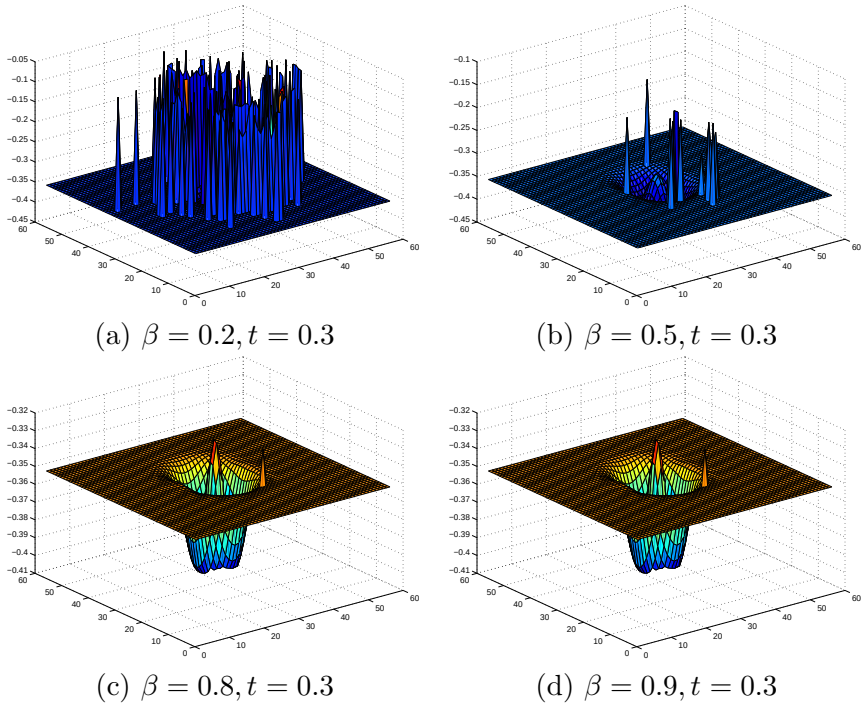

(a) $\beta = 0.2, t = 0.3$ (b) $\beta = 0.5, t = 0.3$

(c) $\beta = 0.8, t = 0.3$ (d) $\beta = 0.9, t = 0.3$

FIGURE 3. Backscattered immersed data of the second component E_2 of electric field for object number 7 (wooden doll, empty inside) of Table 1 for different values of the parameter β in (7.6). Recall that the final time is $T = 1.2$.

In our numerical studies we apply adaptive algorithm of section 6 to refine shape for nine (9) targets listed in Table 1. Three of them (targets number 1, 2, 5) were dielectrics, three were metallic objects (targets

Target number	**Specification of the target**
1	a piece of oak, rectangular prism
2	a piece of pine
3	a metallic sphere
4	a metallic cylinder
5	a piece of oak
6	a metallic rectangular prism
7	a wooden doll, air inside, heterogeneous target
8	a wooden doll, metal inside, heterogeneous target
9	a wooden doll, sand inside, heterogeneous target

TABLE 1. *Names of targets.*

Target number	1	2	5	7	9	Average error
Measured n, error	2.11, 19%	1.84, 18%	2.14, 28%	1.89, 30%	2.1, 26%	24%
n in glob.conv, error	1.92, 9%	1.8, 2%	1.83, 15%	1.86, 2%	1.92, 9%	8%
n, coarse mesh, error	1.94, 8%	1.82, 1%	1.84, 14%	1.88, 0.5%	1.93, 8%	6%
n, 1 time ref. mesh, error	1.94, 8%	1.82, 1%	1.85, 14 %	1.89, 0%	1.93, 8%	6%
n, 2 times ref. mesh, error		1.84, 0%		1.9, 0.5%	1.96, 7%	2%
n, 3 times ref. mesh, error				1.89, 0 %		0%

TABLE 2. *Computed n(target) and directly measured refractive indices of dielectric targets together with both measurement and computational errors as well as the average error. Note that the average computational errors are at least 4 times less than the average error of direct measurements. In all tests we have used the following values of above parameters: the regularization parameter $\gamma = 0.01$ in (4.4), $\theta = 10^{-9}$ in Step 3 of the adaptive algorithm, $\beta_1 = 0.7$ in (6.2) and $s = 1$ in (3.14).*

number 4, 5, 6) and three (targets number 7, 8, 9) were dolls with different objects placed inside them. Heterogeneous targets present models for explosive devices in which explosive materials are masked by dielectrics. Target number 7 was a wooden doll which was empty inside, target number 8 was a piece of a metal inserted inside that doll, and in target number 9 dry sand was partly inserted inside the doll.

The targets number 1 and 4 were used as calibration targets for metals and dielectrics respectively. The use of calibration targets has resulted in the optimal choices of all our parameters. In particular, the cut-off number in (7.7) was chosen 0.85 and the number $\beta = 0.5$ in (7.6) for all dielectric targets of Table 1. In the case of metallic targets, we have chosen the cut-off number 0.3 in (7.8). As to the parameter β in (7.6) for metallic targets, it was chosen $\beta = 0.5$: the same as for dielectric targets.

Figures 3, 4 show backscattered immersed data of the second component E_2 of the electric field for object 7 at different times and with different immersing factor β in (7.6).

In the case of dielectric targets we have *a posteriori* directly measured their refractive indices $n = \sqrt{\varepsilon_r}$. Let $\varepsilon_r^{comp}(\mathbf{x})$ be the computed coefficient. We consider maximal values of functions $\varepsilon_r^{comp}(\mathbf{x})$. This means that in our Tables 2, 3 we list values of dielectric constants ε_r (target) and refractive indices n (target) as

$$\varepsilon_r(\text{target}) = \max_{\overline{\Omega}} \varepsilon_r^{comp}(\mathbf{x}), n(\text{target}) = \sqrt{\varepsilon_r(\text{target})}.$$

Tables 2, 3 are quite informative ones since they show the accuracy of our reconstruction of either refractive indices (Table 2) or effective dielectric constants (Table 3). Table 2 lists refractive indices of dielectric targets, both computed n (target) and directly measured ones n. Computed numbers n (target) are displayed for different locally refined meshes. This table also shows the measurement error in direct measurements of n. Table 3 lists calculated effective dielectric constants ε_r (target) of metallic targets, again for different locally refined meshes. In Table 3 for all metallic targets we have ε (target) > 10, which means that (7.1) is satisfied.

One can derive several important observations from Table 2. First, for all targets and on all adaptively refined meshes the computational error is significantly less than the error of direct measurements. Thus, the average computational error is significantly less than the average measurement error on all adaptively refined meshes. Second, computed refractive

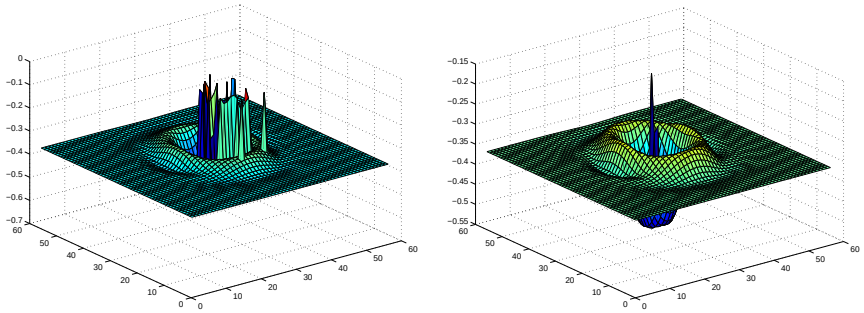

(a) $\beta = 0.2, t = 0.45$

(b) $\beta = 0.5, t = 0.45$

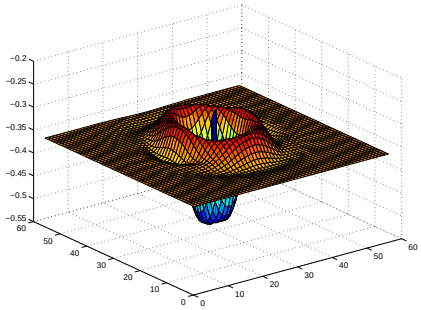

(c) $\beta = 0.8, t = 0.45$

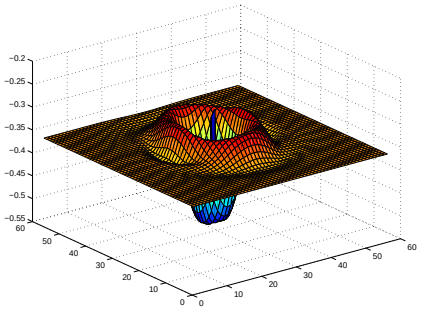

(d) $\beta = 0.9, t = 0.45$

FIGURE 4. Backscattered immersed data of the second component E_2 of electric field for object 7 (wooden doll, empty inside) of Table 1 for different values of the parameter β in (7.6). Recall that the final time is $T = 1.2$.

indices are within reasonable error estimates in all cases. The accuracy on all adaptively refined meshes is about the same.

We observe from Table 3 that for target number 8 we have obtained effective dielectric constant $\varepsilon\,(\text{target}) \in [13.6, 14]$ on all adaptively refined meshes, which is less than for other metallic objects. We can explain this by the fact that target number 8 is a mixture of metal and dielectric. An important observation, which can be deduced from Table 3, is that our two-stage algorithm can still compute large inclusion/background contrasts exceeding 10:1, just as the algorithm of the first stage.

Figures 6–16 display 3-d images of some targets listed in Table 1 as well as corresponding adaptively locally refined meshes. To have a better

visualization, we have zoomed some figures to 0.4×0.4 square from 1×1 square in the x, y directions. So, in these Figures we display only the image in the domain Ω_{zoom},

$$\Omega_{zoom} = \{\mathbf{x} = (x, y, z) \in (-0.2, 0.2) \times (-0.2, 0.2) \times (-0.1, 0.04)\}, \tag{8.1}$$

Figures 6– 16 also show estimates of sizes of the targets in the z-direction. Locations of all targets as well as their sizes in x, y, z directions are well estimated.

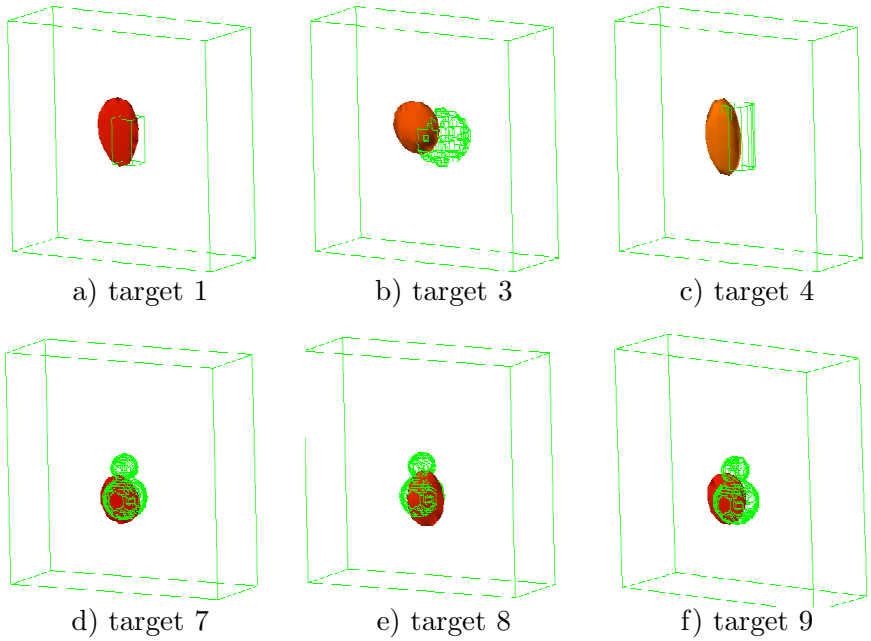

a) target 1 b) target 3 c) target 4

d) target 7 e) target 8 f) target 9

FIGURE 5. Reconstructions of some targets of Table 1 obtained in [8, 28] on the first stage of our two-stage numerical procedure.

9. Summary

We have used time dependent backscattering experimental data generated by a single source of electric pulses to simultaneously reconstruct all three parameters of interest of explosive-like targets: their refractive

indices, shapes and locations. To do this, we have used the two-stage reconstruction procedure, which was first proposed in [5]. On the first stage the globally convergent method of [4, 6] was used. This method has provided accurate estimates of refractive indices and locations of targets [8, 28]. On the second stage, which is the focus of this paper, images were refined using the adaptivity technique of [10]. The second stage has provided accurate estimates of the third component: the shape, in addition to the first two ones. Interestingly, even heterogeneous targets, which model heterogeneous IEDs, were quite accurately imaged.

In all cases one can observe a significant improvement of the image quality after the application of the adaptivity on the second stage. Another observation here is that we can accurately image shapes of not only targets with "straight" boundaries, like a rectangular prism (target number 1) or a cylinder (target number 4) but targets with curved boundaries as well (targets number 3 and 7). Even shadow parts of targets number $1, 3, 4, 8$ are imaged rather well. This is regardless on the fact that we use the minimal possible information content and on a narrow view angle: single location of the source and time resolved backscattering data.

Target number	3	4	6	8			
$\varepsilon_r(target)$ of glob.conv.	14.4	15.0	25	13.6			
$\varepsilon_r(target)$ coarse mesh	14.4	17.0	25	13.6			
$\varepsilon_r(target)$ 1 time ref.mesh	14.5	17.0	25	13.6			
$\varepsilon_r(target)$ 2 times ref.mesh	14.6	17.0	25	13.7			
$\varepsilon_r(target)$ 3 times ref.mesh	14.6	17.0		14.0			
$\varepsilon_r(target)$ 4 times ref.mesh		17.0					

TABLE 3. *Computed appearing dielectric constants* $\varepsilon_r(target)$ *of metallic targets with numbers 3,4,6 as well as of target number 8 which is a metal covered by a dielectric. The mesh refinement process for target number 6 has stopped on three (3) mesh refinements.*

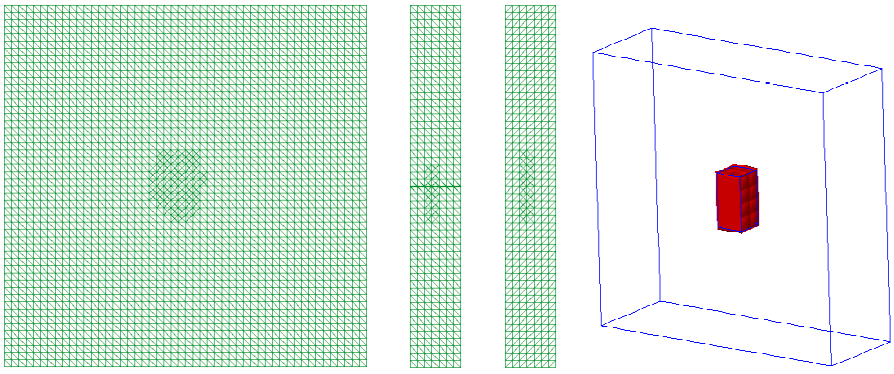

(a) (b) (c) (d)

FIGURE 6. (a) xy-projection, (b) xz-projection, and (c) yz-projection of the once refined (optimal) mesh; d) Computed image of target number 1 of Table 1 on that mesh. Thin lines indicate correct shapes. To have a better visualization we have zoomed the domain Ω in (7.3) in the domain Ω_{zoom} in (8.1). This target number 1 was used for the calibration purpose for the case of dielectric targets. A significant improvement of the image of d), compared with the image of Figure 5-a), obtained on the first stage is evident.

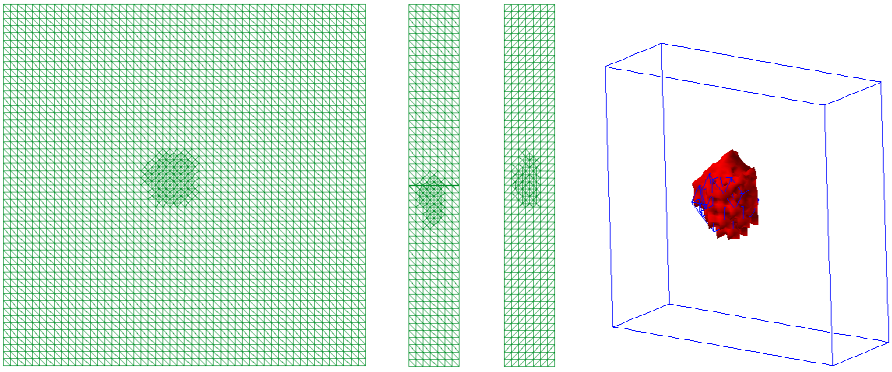

(a) (b) (c) (d)

FIGURE 7. (a) xy-projection, (b) xz-projection, and (c) yz-projection of the three times refined (optimal) mesh; d) Computed image of target number 3 of Table 1 on that mesh. Thin lines indicate correct shape. To have better a visualization we have zoomed the domain Ω in (7.3) in the domain Ω_{zoom} in (8.1). Comparison with Figure 5-b) shows a significant improvement compared with the first stage.

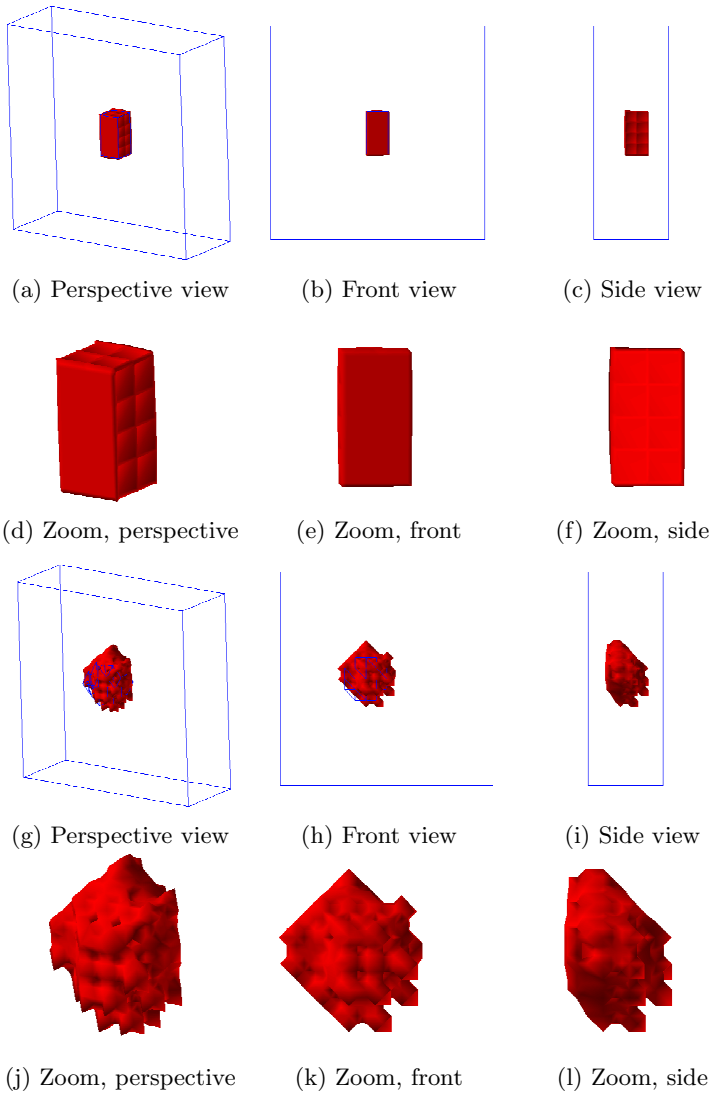

(a) Perspective view (b) Front view (c) Side view

(d) Zoom, perspective (e) Zoom, front (f) Zoom, side

(g) Perspective view (h) Front view (i) Side view

(j) Zoom, perspective (k) Zoom, front (l) Zoom, side

FIGURE 8. Three views and zooms of the reconstruction of target number 1 (figures a)-f)) on the once refined mesh. Three views and zooms of the reconstruction of target number 3 (figures g)-l)) of Table 1 on three times refined mesh. Recall that target number 3 is a metallic sphere.

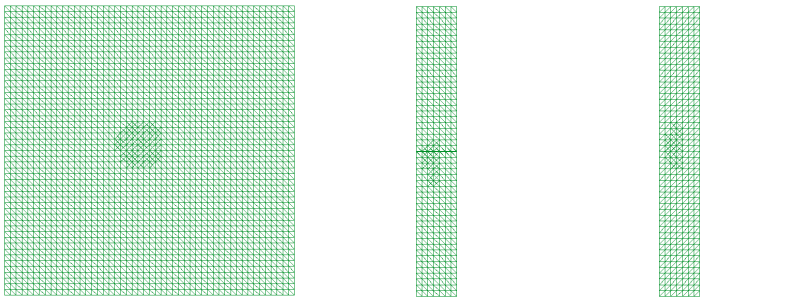

(a) xy-projection (b) xz-projection (c) yz-projection

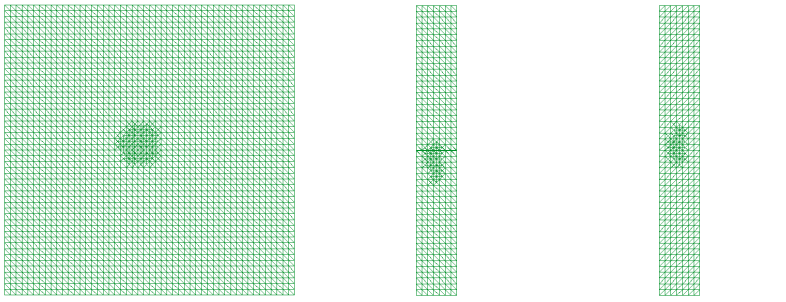

(d) xy-projection (e) xz-projection (f) yz-projection

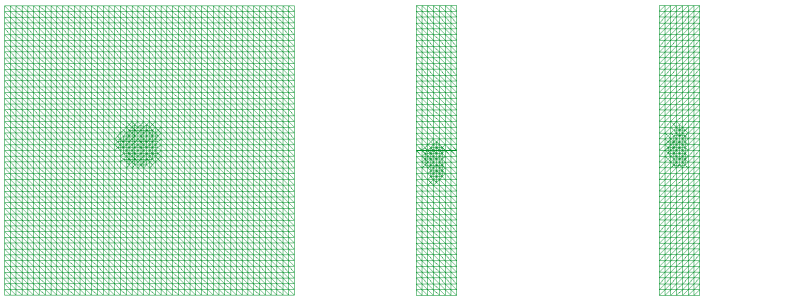

(g) xy-projection (h) xz-projection (i) yz-projection

FIGURE 9. Adaptively refined meshes for the target number 3 of Table 1. (a) - (c) once refined, (d) - (f) twice refined, (g) - (i) three times refined mesh.

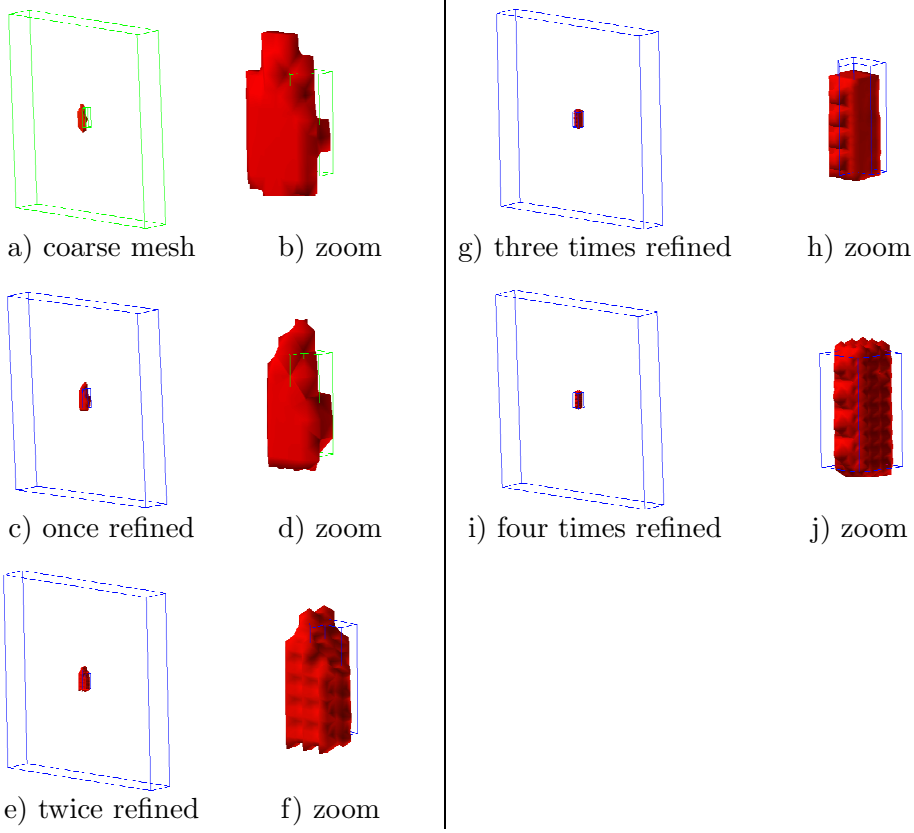

FIGURE 10. *Computed images of target number 4 of Table 1 on four times adaptively refined meshes. Compare with Figure 5-c).*

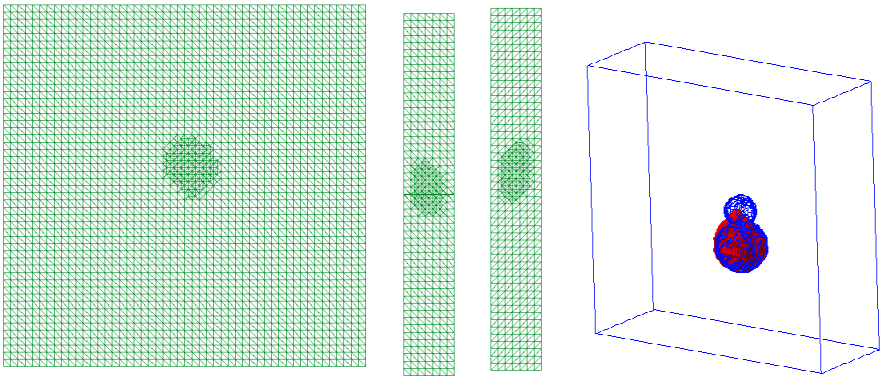

(a) (b) (c) (d)

FIGURE 11. (a) xy-projection, (b) xz-projection, and (c) yz-projection of the three times refined (optimal) mesh; d) Computed image of target number 7 (doll, air inside) of Table 1 on that mesh. Thin lines indicate correct shape.

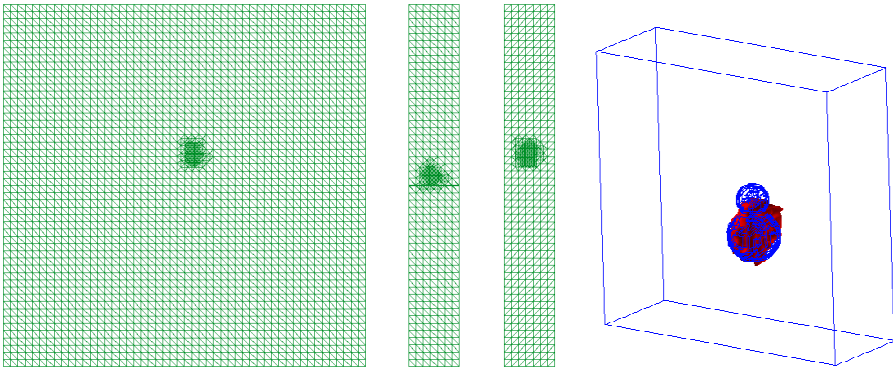

(a) (b) (c) (d)

FIGURE 12. (a) xy-projection, (b) xz-projection, and (c) yz-projection of the three times refined (optimal) mesh and the reconstruction (d) of target number 8 on the optimal mesh.

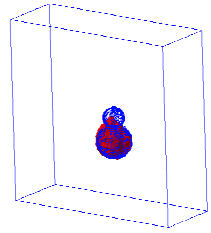

(a) Perspective view

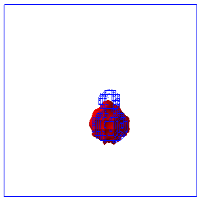

(b) Front view

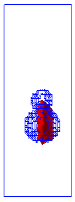

(c) Side view

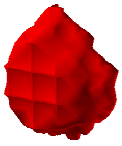

(d) Zoom, perspective

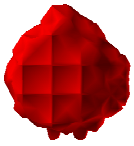

(e) Zoom, front

(f) Zoom, side

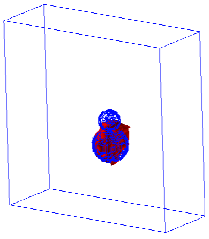

(g) Perspective view

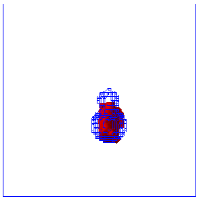

(h) Front view

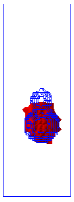

(i) Side view

(j) Zoom, perspective

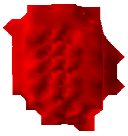

(k) Zoom, front

(l) Zoom, side

FIGURE 13. Three views and zooms of targets number 7 (figures a)-f), doll, air inside) and number 8 (figures g)-l), doll, metal inside) of Table 1 on three times refined mesh. Thin lines indicate correct shape. We observe that on d) and e) even the head of the doll is indicated, which was the most difficult part. As to images g)-l), it follows from (7.8) that they display mostly the metallic part. Comparison of d), j) with Figures 5-d), e) again shows a significant improvement of the image due to the adaptivity.

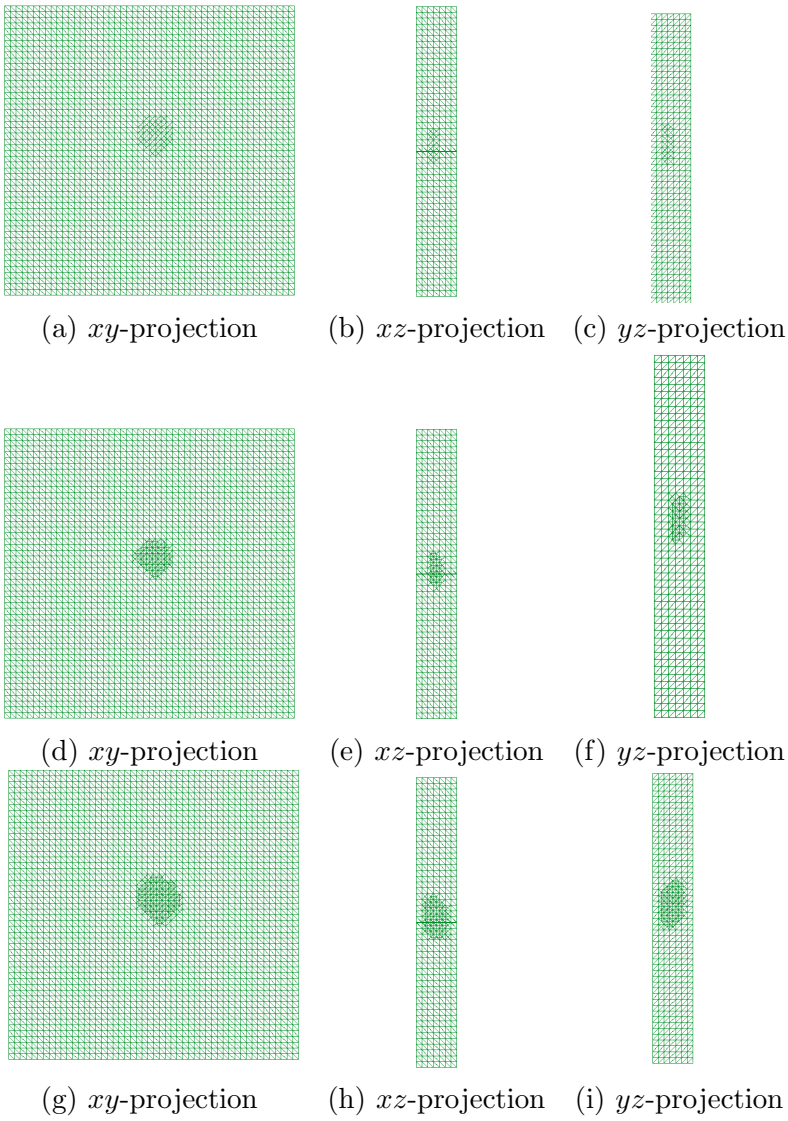

(a) xy-projection (b) xz-projection (c) yz-projection

(d) xy-projection (e) xz-projection (f) yz-projection

(g) xy-projection (h) xz-projection (i) yz-projection

FIGURE 14. Adaptively refined meshes for target number 7 (doll, air inside) of Table 1 used in our computations. (a) - (c) once refined, (d) - (f) twice refined, (g) - (i) three times refined.

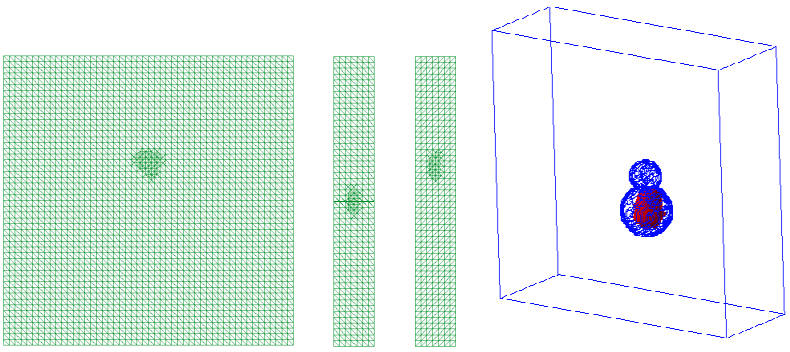

(a) (b) (c) (d)

FIGURE 15. (a) xy-projection, (b) xz-projection, and (c) yz-projection of the twice refined (optimal) mesh and the reconstruction (d) of target number 9 on the three times refined mesh.

Acknowledgments

This research was supported by US Army Research Laboratory and US Army Research Office grant W911NF-11-1-0399, the Swedish Research Council, the Swedish Foundation for Strategic Research (SSF) through the Gothenburg Mathematical Modelling Centre (GMMC). The computations were performed on resources at Chalmers Centre for Computational Science and Engineering (C3SE) provided by the Swedish National Infrastructure for Computing (SNIC).

References

[1] F. Assous, P. Degond, E. Heintze and P. Raviart, On a finite-element method for solving the three-dimensional Maxwell equations, *J. Comput.Physics*, 109, 222–237, 1993.

[2] A.B. Bakushinsky and M.Yu. Kokurin, *Iterative Methods for Approximate Solutions of Inverse Problems*, Springer, New York, 2004.

[3] L. Beilina and M.V. Klibanov, Relaxation property for the adaptivity for ill-posed problems, *Applicable Analysis*, 93, 223-253, 2014.

[4] L. Beilina and M.V. Klibanov, A globally convergent numerical method for a coefficient inverse problem, *SIAM J. Scientific Computing*, 31, 478-509, 2008.

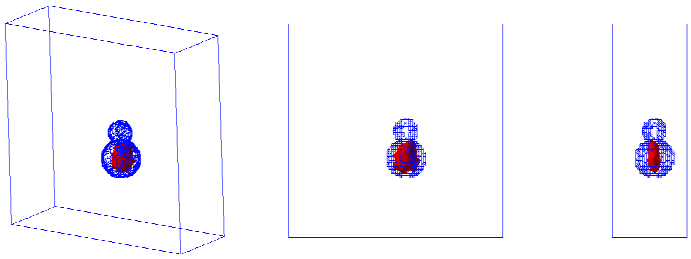

(a) Perspective view (b) Front view (c) Side view

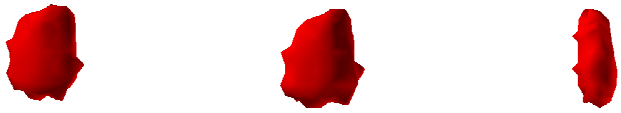

(d) Zoom, perspective (e) Zoom, front (f) Zoom, side

FIGURE 16. Three views and zooms of target number 9 of Table 1 on twice refined mesh. Thin lines indicate correct shape. Comparison of d) with Figure 5-f) again shows a significant improvement of the image due to the adaptivity.

[5] L. Beilina and M.V. Klibanov, Synthesis of global convergence and adaptivity for a hyperbolic coefficient inverse problem in 3D, *J. Inverse and Ill-Posed Problems*, 18, 85-132, 2010.

[6] L. Beilina and M.V. Klibanov, *Approximate Global Convergence and Adaptivity for Coefficient Inverse Problems*, Springer, New York, 2012.

[7] L. Beilina and M.V. Klibanov, A new approximate mathematical model for global convergence for a coefficient inverse problem with backscattering data, *J. Inverse and Ill-Posed Problems*, 20, 513-565, 2012.

[8] L. Beilina, Nguyen Trung Thành, M. V. Klibanov and M. A. Fiddy, Reconstruction from blind experimental data for an inverse problem for a hyperbolic equation, *Inverse Problems* 30, 025002, 2014.

[9] L. Beilina, Energy estimates and numerical verification of the stabilized domain decomposition finite element/finite difference approach for the Maxwell's system in time domain, *Central European Journal of Mathematics*, 11, 702-733, 2013.

[10] L. Beilina, Adaptive Finite Element Method for a coefficient inverse problem for the Maxwell's system, *Applicable Analysis*, 90, 1461-1479, 2011.

[11] L. Beilina and C. Johnson, A posteriori error estimation in computational inverse scattering, *Mathematical Models in Applied Sciences*, 1, 23-35, 2005.

[12] S. C. Brenner and L. R. Scott, *The Mathematical Theory of Finite Element Methods*, Springer-Verlag, Berlin, 1994.

[13] A.L. Bukhgeim and M.V. Klibanov, Uniqueness in the large of a class of multidimensional inverse problems, *Soviet Math. Doklady*, 17, 244-247, 1981.

[14] B. Engquist and A. Majda, Absorbing boundary conditions for the numerical simulation of waves, *Math. Comp.,* 31, 629-651, 1977.

[15] V. Isakov, Inverse obstacle problems, *Inverse Problems*, 25, 123002, 2009.

[16] P. Joly, *Variational Methods for Time-Dependent Wave Propagation Problems*, Lecture Notes in Computational Science and Engineering, Springer, New York, 2003.

[17] M.V. Klibanov, Carleman estimates for global uniqueness, stability and numerical methods for coefficient inverse problems, survey, *J. Inverse and Ill-Posed Problems*, 21, 477-560, 2013.

[18] A.V. Kuzhuget, L. Beilina, M.V. Klibanov, A. Sullivan, L. Nguyen and M.A. Fiddy, Blind experimental data collected in the field and an approximately globally convergent inverse algorithm, *Inverse Problems*, 28, 095007, 2012.

[19] O.A. Ladyzhenskaya, *Boundary Value Problems of Mathematical Physics*, Springer, New York, 1985.

[20] A. Lakhal, A decoupling based imaging method for inverse medium scattering for Maxwell's equations, *Inverse Problems*, 26, 015007, 2010.

[21] A. Lakhal, KAIRUAIN-algorithm applied on electromagnetic imaging, *Inverse Problems*, 29, 095001, 2013.

[22] J. Li, J. Xie and J. Zou, An adaptive finite element reconstruction of distributed fluxes, *Inverse Problems*, 27, 075009, 2011.

[23] J. Li, H. Y. Liu, H. Sun and J. Zou, Reconstructing acoustic obstacles by planar and cylindrical waves, *J. Math. Phys.*, 53, 103705, 2012.

[24] J. Li, H. Y. Liu, H. Sun and J. Zou, Imaging acoustic obstacles by singular and hypersingular point sources, *Inverse Problems and Imaging*, 7, 545–563, 2013.

[25] Y. Liu, J. Su, Z.-J. Lin, S. Teng, A. Rhoden, N. Pantong, and H. Liu. Reconstructions for continuous-wave diffuse optical tomography by a globally convergent method. 2013. Preprint, available online at http://www.ma.utexas.edu/mp_arc/, preprint number 13 - 87.

[26] O. Pironneau, *Optimal shape design for elliptic systems*, Springer-Verlag, Berlin, 1984.

[27] R. Stolt, Migration by Fourier transform, *Geophysics*, 43, 23–48, 1978.

[28] Nguyen Trung Thành, L. Beilina, M. V. Klibanov and M. A. Fiddy, Reconstruction of the refractive index from experimental backscattering data using a globally convergent inverse method, *SIAM J. Scientific Computing*, 36, B273-B293, 2014.

[29] N. T. Thành, L. Beilina, M. V. Klibanov, and M. A. Fiddy. Imaging of buried objects from experimental backscattering radar measurements using a globally convergent inverse method, *arxiv*: 1406.3500v1 [math-ph], 2014.

[30] M. Sini and Nguyen Trung Thành, Inverse acoustic obstacle scattering problems using multifrequency measurements, *Inverse Problems and Imaging*, 6, 749–773, 2012.

[31] M. Sini and Nguyen Trung Thành, Convergence rates of recursive Newton-type methods for multifrequency scattering, *arXiv*:1310.5156 [math.NA], 2013.

[32] WavES, the software package, http://www.waves24.com

[33] O. Yilmaz. *Seismic Data Imaging.* Society of Exploration Geophysicists, Tulsa Oklahoma, 1987.

Paper IV

Reprinted from Larisa Beilina, Nguyen Trung Thành, Michael V. Klibanov and John Bondestam Malmberg, Globally convergent and adaptive finite element methods in imaging of buried objects from experimental backscattering radar measurements, *Journal of Computational and Applied Mathematics*, Copyright (2014),
http://dx.doi.org/10.1016/j.cam.2014.11.055, with permission from Elsevier.

Globally convergent and adaptive finite element methods in imaging of buried objects from experimental backscattering radar measurements

Larisa Beilina[1], Nguyen Trung Thành[2],
Michael V. Klibanov[3], John Bondestam Malmberg[4]

Abstract. We consider a two-stage numerical procedure for imaging of objects buried in dry sand using time-dependent backscattering experimental radar measurements. These measurements are generated by a single point source of electric pulses and are collected using a microwave scattering facility which was built at the University of North Carolina at Charlotte. Our imaging problem is formulated as the inverse problem of the reconstruction of the spatially distributed dielectric constant $\varepsilon_{\mathrm{r}}(\mathbf{x})$, $\mathbf{x} \in \mathbb{R}^3$, which is an unknown coefficient in Maxwell's equations.

On the first stage the globally convergent method of [1] is applied to get a good first approximation for the exact solution. Results of this stage were presented in [2]. On the second stage the locally convergent adaptive finite element method of [3] is applied to refine the solution obtained on the first stage. The two-stage numerical procedure results in accurate imaging of all three components of interest of targets: shapes, locations and refractive indices. In this paper we briefly describe methods and present new reconstruction results for both stages.

Keywords: inverse scattering, refractive indices, globally convergent algorithm, adaptive finite element method.

[1]Department of Mathematical Sciences, Chalmers University of Technology and University of Gothenburg, SE-412 96 Gothenburg, Sweden. E-mail: larisa@chalmers.se

[2]Department of Mathematics, Iowa State University, Ames, IA, USA. E-mail: thanh@iastate.edu

[3]Department of Mathematics & Statistics, University of North Carolina at Charlotte, Charlotte, NC, USA. E-mail: mklibanv@uncc.edu

[4]Department of Mathematical Sciences, Chalmers University of Technology and University of Gothenburg, SE-412 96 Gothenburg, Sweden. E-mail: john.bondestam.malmberg@chalmers.se

1. Introduction

In this paper we consider the problem of reconstruction of refractive indices, shapes and locations of buried objects in the dry sand from backscattering time-dependent experimental data using the two-stage numerical procedure presented in [1, 4–6]. Our problem is a coefficient inverse problem (CIP) for Maxwell's equations in three dimensions. Experimental data were collected using a microwave scattering facility which was built at the University of North Carolina at Charlotte, USA. Our experimental data were collected using a single location of the source. The backscattered signal was measured on a part of a plane. Our potential applications are in imaging of explosives, such as land mines and improvised explosive devices. This work is a continuation of our recent works on this topic, where we have treated a much simpler case of experimental data for targets placed in air [5, 7, 8].

The two-stage numerical procedure means that we combine two different methods to solve our CIP. On the first stage the globally convergent numerical method of [1] is applied in order to obtain a good first approximation for the exact solution without any a priori knowledge of a small neighborhood of this solution, see section 2.9 of [1] as well as [9] for global convergence theorems. We presented results of reconstruction of the first stage in our publications [7, 8] for objects placed in air. In our recent study [2] we presented reconstructions of twenty five (25) objects. This study has demonstrated that the method of [1] works well in estimating the dielectric constants (equivalently, refractive indices) and locations of buried objects.

It was proved in [10] that a minimizer of the Tikhonov functional is indeed closer to the exact solution than the first guess for this solution. Thus, it makes sense to apply the Tikhonov functional in order to refine the solution which we have obtained on the first stage of our two-stage numerical procedure. To do this, the locally convergent adaptive finite element method of [3] (adaptivity) is applied on the second stage. The adaptivity uses the solution of the first stage as the starting point in the minimization of a Tikhonov functional in order to obtain better approximations of refractive indices and shapes of objects on the adaptively refined meshes. It was shown in [5] that the adaptivity helps to accurately image simultaneously all three components of interest for targets placed in the air: refractive indices, shapes and locations.

Compared to the case of imaging of targets placed in air (see [5, 7, 8]), there are three main difficulties in imaging of buried targets: (i) the signals of targets are much weaker than those when the targets are in air, (ii) these signals may overlap with the reflection from the ground's surface, which makes them difficult to distinguish, and (iii) the reflection from the grounds surface may dominate the target's signals after the Laplace transform since the kernel of this transform decays exponentially with respect to time. We have handled this difficulty in [2] via a new data preprocessing procedure. This procedure results in preprocessed data, which are used as the input for our globally convergent algorithm, i.e. the input for the first stage of our method.

It is notable that we have experimentally observed a rare superresolution phenomenon and have numerically reconstructed the corresponding image, see Figures 4-d) and 9. The resolution limit which follows from the Born approximation, i.e. the diffraction limit, is $\lambda/2$, where λ is the wavelength of the signal. In our experimental device $\lambda = 4.5$ centimeters (cm). We have resolved two targets at the distance of 1 cm $= \lambda/4.5$ between their surfaces. At the same time, the backscattering signal was measured at the distance of about 80 cm $\approx$ 18 wavelengths off the targets, i.e. in the far field zone. It was shown in, for instance [11], that the superresolution can occur because of nonlinear scattering, and our algorithm is nonlinear, including the step of extraction of the target's signal in our data preprocessing procedure [2]. Experimentally the superresolution phenomenon was demonstrated in [12]. We also refer to the recent work [13] where the superresolution is discussed.

An outline of this paper is as follows. In section 2 we briefly describe the globally convergent method. In section 3 we present the forward, inverse, and adjoint problems as well as the Tikhonov functional for the second stage. In section 4 we describe the finite element method used in computations and in section 5 we investigate general framework for a posteriori error estimation for CIPs. In section 6 we describe the mesh refinement recommendation and the adaptive algorithm. In section 7 we present results of our computations.

2. The first stage

In this section we state the forward and inverse problems which we consider on the first stage. We also briefly outline the globally convergent

method of [1] and present the algorithm used in computations of the first stage.

2.1. Forward and inverse problems. Let $\Omega \subset \mathbb{R}^3$ be a convex bounded domain with the boundary $\partial\Omega \in C^3$. Denote the spatial coordinates by $\mathbf{x} = (x, y, z) \in \mathbb{R}^3$. Let $C^{k+\alpha}$ be Hölder spaces, where $k \geq 0$ is an integer and $\alpha \in (0, 1)$. We consider the propagation of the electromagnetic wave in $\mathbb{R}^3$ generated by an incident plane wave. On the first stage we model the wave propagation by the following Cauchy problem for the scalar wave equation

$$\varepsilon_{\mathrm{r}}(\mathbf{x})\frac{\partial^2 u}{\partial t^2}(\mathbf{x}, t) - \Delta u(\mathbf{x}, t) = \delta(z - z_0)f(t), \quad (\mathbf{x}, t) \in \mathbb{R}^3 \times (0, \infty), \tag{2.1}$$

$$u(\mathbf{x}, 0) = 0, \quad \frac{\partial u}{\partial t}(\mathbf{x}, 0) = 0, \qquad \mathbf{x} \in \mathbb{R}^3. \tag{2.2}$$

Here $f(t) \not\equiv 0$ is the time-dependent waveform of the incident plane wave generated at the plane $\{z = z_0\}$ and propagating along the z-axis, and u is the total wave.

Let the function $E(\mathbf{x}, t) = (E_1, E_2, E_3)(\mathbf{x}, t)$ be the electric field. In our experiments the single non-zero component of the incident electric field is E_2 and we measure the backscattering function E_2, which is the voltage. Our mathematical model of the first stage uses only the single equation (2.1) with $u = E_2$ instead of the full Maxwell's system. Such approximation is reasonable, since it was shown numerically in [14] that the component E_2 of the electric field E dominates wo other components in the case which we consider. Also, see [1] where a similar scalar wave equation was used to work with transmitted experimental data.

The function $\varepsilon_{\mathrm{r}}(\mathbf{x})$ in (2.1) represents the spatially distributed relative dielectric constant, i.e. the dielectric constant. It is known that $\varepsilon(\mathbf{x}) = \varepsilon_{\mathrm{r}}(\mathbf{x})\varepsilon_0$, where $\varepsilon(\mathbf{x})$ is the absolute dielectric permittivity of the material and ε_0 is the dielectric permittivity of vacuum. Both $\varepsilon(x)$ and ε_0 are measured in Farad/meter. Thus, $\varepsilon_{\mathrm{r}}(x)$ is dimensionless. We assume that ε_{r} is unknown inside the domain $\Omega \subset \mathbb{R}^3$ and is known outside of it,

$$\varepsilon_{\mathrm{r}} \in C^{\alpha}\left(\mathbb{R}^3\right), \quad \varepsilon_{\mathrm{r}}(\mathbf{x}) \in [1, b] \text{ for } \mathbf{x} \in \mathbb{R}^3, \quad \varepsilon_{\mathrm{r}}(\mathbf{x}) = 1 \text{ for } \mathbf{x} \in \mathbb{R}^3 \setminus \Omega, \tag{2.3}$$

where $b > 1$ is a constant. We assume that the set of admissible coefficients in (2.3) is known. In our experiments the plane wave is initialized outside of the domain $\overline{\Omega}$, i.e. $\overline{\Omega} \cap \{z = z_0\} = \varnothing$.

Coefficient Inverse Problem 1 (CIP1). *Determine the function* $\varepsilon_r(\mathbf{x})$ *for* $\mathbf{x} \in \Omega$*, assuming that the following function* g *is known for a single incident plane wave generated at the plane* $\{z = z_0\}$ *outside of* $\overline{\Omega}$*:*

$$u(\mathbf{x}, t) = g(\mathbf{x}, t) \ \forall (\mathbf{x}, t) \in \Gamma \times (0, \infty),$$

where $\Gamma \subset \partial\Omega$ *is a part of the boundary* $\partial\Omega$*. In our experiments, this set corresponds to the backscattering boundary of* Ω*.*

Remark 2.1. Although the data function g is given only on the part Γ of $\partial\Omega$, we can extend it numerically to a function $\tilde{g}$ defined on all of $\partial\Omega$, see Section 4 of [5]. Hence we may assume that $g(\mathbf{x}, t)$ is known for every $(\mathbf{x}, t) \in \partial\Omega \times (0, T)$.

Global uniqueness theorems for multidimensional CIPs with a single measurement are currently known only under the assumption that at least one of initial conditions does not equal zero in the entire domain $\overline{\Omega}$ [1, 15]. However, this is not our case and the method of Carleman estimates is inapplicable to our CIP. Thus, we simply assume that uniqueness of our CIP holds.

2.2. The globally convergent method. Here we briefly present globally convergent method of [1].

First, consider the Laplace transformation

$$\tilde{u}(\mathbf{x}, s) = \int_0^\infty u(\mathbf{x}, t) e^{-st} \, dt, \tag{2.4}$$

where s is a positive parameter which we call *pseudo frequency*. We assume that $s \geq \underline{s} = const. > 0$ and denote by $\tilde{f}(s)$ the Laplace transform of $f(t)$. Here $\underline{s} = const. > 0$ is a certain parameter, which guarantees that integral (2.4) converges for $s \geq \underline{s}$. We assume that $\tilde{f}(s) \neq 0$ for all $s \geq \underline{s}$. Define $w(\mathbf{x}, s) := \tilde{u}(\mathbf{x}, s)/\tilde{f}(s)$. The function w satisfies the equation

$$\Delta w(\mathbf{x}, s) - s^2 \varepsilon_r(\mathbf{x}) w(\mathbf{x}, s) = -\delta(z - z_0), \quad \mathbf{x} \in \mathbb{R}^3, \ \ s \geq \underline{s}. \tag{2.5}$$

It was shown in [2] that $w(\mathbf{x}, s) > 0$ and $\lim_{|\mathbf{x}| \to \infty} [w(\mathbf{x}, s) - w_0(\mathbf{x}, s)] = 0$, where

$$w_0(\mathbf{x}, s) := \frac{e^{-s|z - z_0|}}{2s}$$

is such a solution of equation (2.5) for the case $\varepsilon_r(\mathbf{x}) \equiv 1$, which decays to zero as $|z| \to \infty$. Next, introduce the function v by $v(\mathbf{x}, s) := \ln\big(w(\mathbf{x}, s)\big)/s^2$ and substitute $w = \exp(vs^2)$ into (2.5). Noting that

$\overline{\Omega} \cap \{z = z_0\} = \varnothing$, we obtain the following equation for the explicit computation of the coefficient ε_{r}:

$$\Delta v(\mathbf{x},\, s) + s^2 |\nabla v(\mathbf{x},\, s)|^2 = \varepsilon_{\mathrm{r}}(\mathbf{x}), \quad \mathbf{x} \in \Omega,\ s \geq \underline{s}. \tag{2.6}$$

Next, we eliminate the unknown coefficient $\varepsilon_{\mathrm{r}}(\mathbf{x})$ from (2.6) by taking the derivative with respect to s both sides of (2.6). Let $q = \partial_s v$. Then

$$v(\mathbf{x},\, s) = -\int\limits_s^{\infty} q(\mathbf{x},\, \tau)\, \mathrm{d}\tau = -\int\limits_s^{\bar{s}} q(\mathbf{x},\, \tau)\, \mathrm{d}\tau + V(\mathbf{x}),$$

where $\bar{s} > \underline{s}$. We call the function $V(\mathbf{x}) = v(\mathbf{x},\, \bar{s})$ the "tail function". Hence,

$$V(\mathbf{x}) = \frac{\ln w(\mathbf{x},\, \bar{s})}{\bar{s}^2}. \tag{2.7}$$

From (2.6) we obtain the following equation for two unknown functions q and V

$$\begin{aligned} &\Delta q(\mathbf{x},\, s) - 2s^2 \nabla q(\mathbf{x},\, s) \cdot \int\limits_s^{\bar{s}} \nabla q(\mathbf{x},\, \tau)\, \mathrm{d}\tau \\ &+ 2s^2 \nabla V(\mathbf{x}) \cdot \nabla q(\mathbf{x},\, s) + 2s \left| \int\limits_s^{\bar{s}} \nabla q(\mathbf{x},\, \tau)\, \mathrm{d}\tau \right|^2 \\ &- 4s \nabla V(\mathbf{x}) \cdot \int\limits_s^{\bar{s}} \nabla q(\mathbf{x},\, \tau)\, \mathrm{d}\tau + 2s\, |\nabla V(\mathbf{x})|^2 = 0, \end{aligned} \tag{2.8}$$

for $\mathbf{x} \in \Omega$ and $s \in (\underline{s},\, \bar{s})$.

To find the tail function V we use an iterative procedure presented in the next section, see [7, 8] for details of this procedure. The function q satisfies the following boundary condition

$$q(\mathbf{x},\, s) = \psi(\mathbf{x},\, s), \quad \mathbf{x} \in \partial\Omega, \tag{2.9}$$

where

$$\psi(\mathbf{x},\, s) = \frac{\partial}{\partial s} \left[\frac{\ln \varphi(\mathbf{x},\, s)}{s^2} \right],\ \varphi(\mathbf{x},\, s) = \frac{1}{\tilde{f}(s)} \int\limits_0^{\infty} g(\mathbf{x},\, t) e^{-st}\, \mathrm{d}t.$$

2.3. Iterative procedure and description of the globally convergent algorithm. In our iterative procedure we divide the pseudo frequency interval $[\underline{s},\, \bar{s}]$ into N sub-intervals $\bar{s} = s_0 > s_1 > \cdots > s_N = \underline{s}$ with the step size h such that $s_n - s_{n+1} = h$. We approximate the function q by a piecewise constant function with respect s, $q(\mathbf{x},\, s) \approx q_n(\mathbf{x})$, $s \in (s_n,\, s_{n-1}]$, $n = 1,\, \ldots,\, N$, and set $q_0 \equiv 0$. Next, we multiply equation (2.8) by the Carleman Weight Function $\exp\left[\Lambda\,(s - s_{n-1})\right]$, $s \in (s_n,\, s_{n-1})$, where $\Lambda \gg 1$ is a large parameter chosen in the computations, and integrate with respect to s over every pseudo frequency interval $[s_n,\, s_{n-1}]$. Finally, we get a system of elliptic equations for the functions q_n for $\mathbf{x} \in \Omega$:

$$
\begin{aligned}
&\Delta q_n(\mathbf{x}) + A_{1,\,n} \nabla q_n(\mathbf{x}) \cdot (\nabla V_n(\mathbf{x}) - \nabla \overline{q_{n-1}}(\mathbf{x})) \\
&\qquad = A_{2,n} |\nabla q_n(\mathbf{x})|^2 + A_{3,\,n} |\nabla V_n(\mathbf{x}) - \nabla \overline{q_{n-1}}(\mathbf{x})|^2,
\end{aligned} \tag{2.10}
$$

where $A_{i,\,n}$, $i = 1,\, 2,\, 3$, are some coefficients defined in [1] and can be computed analytically and $\overline{q_{n-1}} = h \sum_{j=0}^{n-1} q_j$. The tail function $V = V_n$ is approximated iteratively, see the algorithm below. The discretized version of the boundary condition (2.9) is given by

(2.11)

$$
q_n(\mathbf{x}) = \psi_n(\mathbf{x}) := \frac{1}{h} \int\limits_{s_n}^{s_{n-1}} \psi(\mathbf{x},\, s)\, \mathrm{d}s \approx \frac{1}{2} [\psi(\mathbf{x},\, s_n) + \psi(\mathbf{x},\, s_{n-1})], \quad \mathbf{x} \in \partial\Omega.
$$

We also note that the first term on the right hand side of (2.10) is negligible compared to the other terms since $|A_{2,\,n}| \sim \Lambda^{-1}$ for sufficiently large Λ, while $|A_{i,\,n}| \sim 1$, $i = 1,\, 3$. Thus, we set $A_{2,\,n} |\nabla q_n|^2 = 0$. The system of elliptic equations (2.10) with boundary conditions (2.11) is solved sequentially starting from $n = 1$. To solve it, we use following algorithm:

Globally convergent algorithm.

- Compute the first tail function V_0 (see section 2.9 of [1] and [9] for details). Set $q_0 \equiv 0$.
- For $n = 1,\, 2,\, \ldots,\, N$
  (1) Set $q_{n,\,0} = q_{n-1}$, $V_{n,\,1} = V_{n-1}$
  (2) For $i = 1,\, 2,\, \ldots,\, m_n$
    - Find $q_{n,\,i}$ by solving (2.10)–(2.11) with $V_n := V_{n,\,i}$.
    - Compute $v_{n,\,i} = -h q_{n,\,i} - \overline{q_{n-1}} + V_{n,\,i}$.

– Compute $\varepsilon_{\mathrm{r},n,i}$ via (2.6). Then solve the forward problem (2.1)–(2.2) with the new computed coefficient $\varepsilon_{\mathrm{r}} := \varepsilon_{\mathrm{r},n,i}$, compute $w := w_{n,i}$ and update the tail $V_{n,i+1}$ by (2.7).

(3) Set $q_n = q_{n,m_n}$, $\varepsilon_{\mathrm{r},n} = \varepsilon_{\mathrm{r},n,m_n}$, $V_n = V_{n,m_n+1}$ and go to the next frequency interval $[s_{n+1},\, s_n]$ if $n < N$. If $n = N$, then stop.

Stopping criteria of this algorithm with respect to i and n are derived computationally and is presented in [7, 8] and its global convergence was proved in [1, 9]. We denote the solution obtained at this stage by $\varepsilon_{\mathrm{r,glob}}$.

3. Statement of Forward and Inverse Problems on the second stage

On the second stage we model the electromagnetic wave propagation in an isotropic and non-magnetic space in $\mathbb{R}^3$ with the dimensionless coefficient ε_{r}, which describes the spatially distributed dielectric constant of the medium. It is known that in the non-magnetic space the relative permeability $\mu_{\mathrm{r}} = 1$ since $\mu(\mathbf{x}) = \mu_0$, where $\mu(\mathbf{x})$ is the magnetic permeability of the material and μ_0 is the permeability of vacuum. Both $\mu(\mathbf{x})$ and μ_0 are measured in Henries/meter. Hence, μ_{r} is dimensionless.

We consider the following Cauchy problem as the model problem for the electric field $E(\mathbf{x},\, t) = (E_1,\, E_2,\, E_3)(\mathbf{x},\, t)$

(3.1)

$$\begin{aligned}
&\varepsilon_{\mathrm{r}}(\mathbf{x})\frac{\partial^2 E}{\partial t^2}(\mathbf{x},\, t) \\
&\qquad + \nabla \times \big(\nabla \times E(\mathbf{x},\, t)\big) = (0,\, \delta(z - z_0)f(t),\, 0), && (\mathbf{x},\, t) \in \mathbb{R}^3 \times (0,\, T), \\
&\nabla \cdot \big(\varepsilon_{\mathrm{r}}(\mathbf{x})E(\mathbf{x},\, t)\big) = 0, && (\mathbf{x},\, t) \in \mathbb{R}^3 \times (0,\, T), \\
&E(\mathbf{x},\, 0) = 0, \quad \frac{\partial E}{\partial t}(\mathbf{x},\, 0) = 0, && \mathbf{x} \in \mathbb{R}^3.
\end{aligned}$$

We assume that the coefficient ε_{r} of equation (3.1) is the same as in (2.3). Let again $\Gamma \subset \partial\Omega$ be a part of the boundary $\partial\Omega$.

Coefficient Inverse Problem 2 (CIP2). *Suppose that the coefficient ε_{r} satisfies* (3.1). *Determine the function $\varepsilon_{\mathrm{r}}(\mathbf{x})$, $\mathbf{x} \in \Omega$, assuming that the following vector function $\widetilde{g}(\mathbf{x},\, t) = (g_1, g_2, g_3)(\mathbf{x},\, t)$ is known for a single incident plane wave:*

$$E(\mathbf{x},\, t) = \widetilde{g}(\mathbf{x},\, t),\ \forall (\mathbf{x},\, t) \in \Gamma \times (0,\, T). \tag{3.2}$$

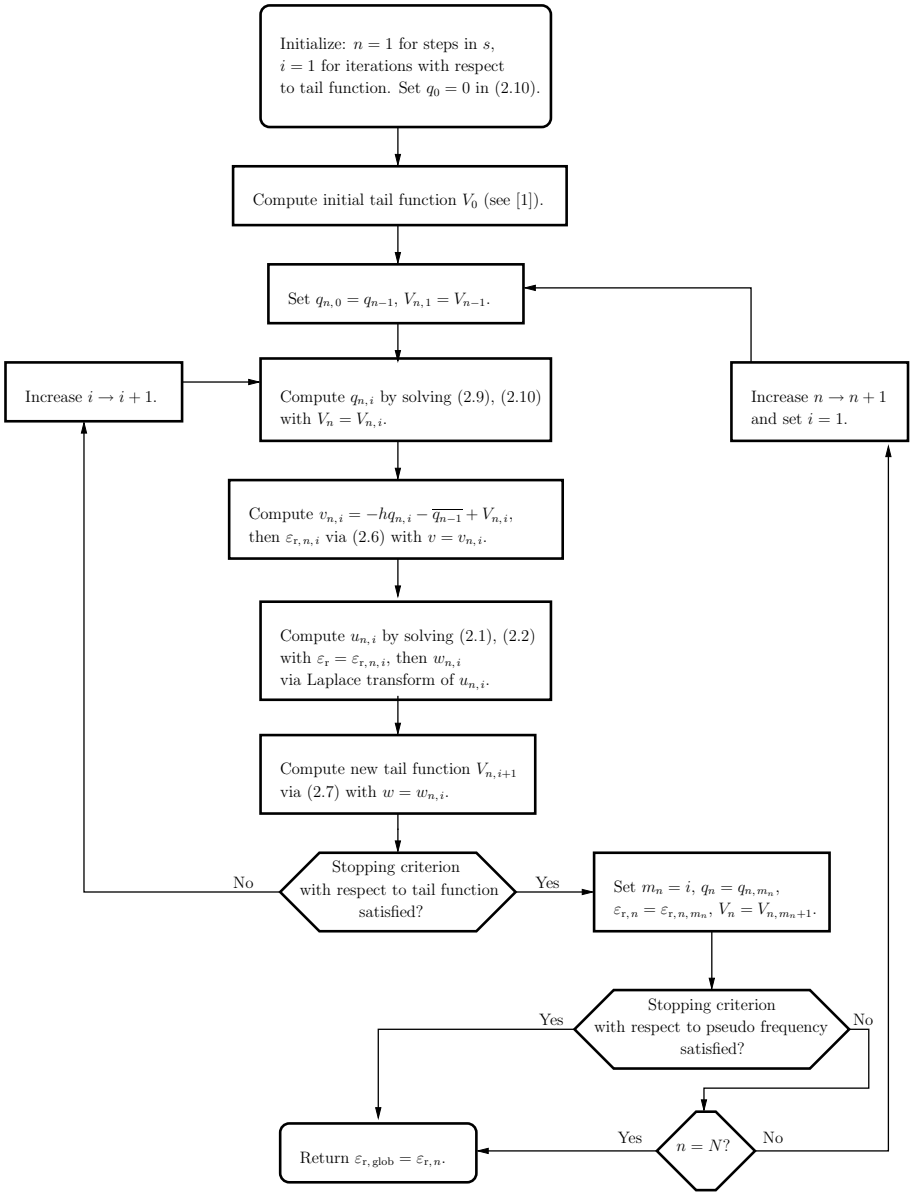

FIGURE 1. Flowchart for the globally convergent method. For the stopping criteria, see [7, 8].

In (3.2) the vector function $\widetilde{g}$ models time dependent measurements of the electric field at the part Γ of the boundary $\partial\Omega$ of the domain Ω in which the coefficient $\varepsilon_{\mathrm{r}}(\mathbf{x})$ is unknown. The uniqueness of CIP2 is currently known only if one would consider in (3.1) a Gaussian function $\widetilde{\delta}(z - z_0)$ centered around z_0, which approximates the function $\delta(z - z_0)$. We again assume that uniqueness holds for our CIP.

The function E_2 in (3.1) models the voltage of one component of the electric field $E(\mathbf{x}, t) = (E_1, E_2, E_3)(\mathbf{x}, t)$. And we indeed measure this component. In our computer simulations of section 7.5 the incident field has only one non-zero component E_2. This component propagates along the z-axis until it reaches the target, where it is scattered. When solving the forward problem in our computations of section 7.5, we first generate the data (3.2) by solving the problem (3.1) for the case when the function ε_{r} is taken as the one reconstructed by the globally convergent method. Next, the computed component E_2 on the surface Γ is replaced with the measured data. The other two components, E_1 and E_3, are left the same as the ones obtained by the solution of the problem (3.1), see details in [5].

3.1. Domain decomposition finite element/finite difference method. To solve the problem (3.1) numerically we choose a bounded domain G such that $\Omega \subset G$. In our computations of the second stage we use the domain decomposition finite element/finite difference method of [14]. To do that we decompose G as $G = \Omega_{\mathrm{FEM}} \cup \Omega_{\mathrm{FDM}}$ with $\Omega_{\mathrm{FEM}} = \Omega$. In our computations, a finite element method is used in Ω_{FEM} and a finite difference method is used in Ω_{FDM}, see details in [14].

Using (2.3) we have that

$$\varepsilon_{\mathrm{r}}(\mathbf{x}) \geq 1, \text{ for } \mathbf{x} \in \Omega_{\mathrm{FEM}},$$
$$\varepsilon_{\mathrm{r}}(\mathbf{x}) = 1, \text{ for } \mathbf{x} \in \Omega_{\mathrm{FDM}}.$$

As in [14] in our computations we used the following stabilized model problem with the parameter $\xi \geq 1$:

(3.3)
$$\varepsilon_{\mathrm{r}}(\mathbf{x})\frac{\partial^2 E}{\partial t^2}(\mathbf{x}, t) + \nabla \times \big(\nabla \times E(\mathbf{x}, t)\big) - \xi\nabla\Big(\nabla \cdot \big(\varepsilon_{\mathrm{r}}(\mathbf{x})E(\mathbf{x}, t)\big)\Big) = 0, \quad (\mathbf{x}, t) \in G \times (0, T),$$

$$E(\mathbf{x},\,0)=0,\quad \frac{\partial E}{\partial t}(\mathbf{x},\,0)=0,\qquad \mathbf{x}\in G. \tag{3.4}$$

To determine boundary conditions for (3.3), (3.4), we choose the domains Ω and G such that

$$\Omega=\Omega_{\mathrm{FEM}}=\left\{\mathbf{x}=(x,\,y,\,z):-a<x<a,\,-b<y<b,\,-c<z<c'\right\},$$

$$G=\left\{\mathbf{x}=(x,\,y,\,z):-A<x<A,\,-B<y<B,\,-C<z<z_0\right\},$$

where $0<a<A$, $0<b<B$, $-C<-c<c'<z_0$, and $\Omega_{\mathrm{FDM}}=G\backslash\Omega_{\mathrm{FEM}}$. Denote by

$$\partial_1 G:=\overline{G}\cap\left\{z=z_0\right\},\quad \partial_2 G:=\overline{G}\cap\left\{z=-C\right\},$$
$$\partial_3 G:=\partial G\setminus\left(\partial_1 G\cup\partial_2 G\right).$$

The backscattering side of Ω is $\Gamma=\partial\Omega\cap\{z=c'\}$. Next, define $\partial_i G_T:=\partial_i G\times(0,\,T)$, $i=1,\,2,\,3$. Let $t'\in(0,\,T)$ be a number, and we assume that the function $f(t)\in C\left[0,\,t'\right]$ and $f(t)=0$ for $t>t'$.

Then boundary conditions for (3.3)–(3.4) are:

$$E\left(\mathbf{x},\,t\right)=(0,\,f(t),\,0),\qquad (\mathbf{x},\,t)\in\partial_1 G\times\left(0,\,t'\right], \tag{3.5}$$

$$\frac{\partial E}{\partial n}(\mathbf{x},\,t)=-\frac{\partial E}{\partial t}(\mathbf{x},\,t),\qquad (\mathbf{x},\,t)\in\partial_1 G\times\left(t',\,T\right), \tag{3.6}$$

$$\frac{\partial E}{\partial n}(\mathbf{x},\,t)=-\frac{\partial E}{\partial t}(\mathbf{x},\,t),\qquad (\mathbf{x},\,t)\in\partial_2 G_T, \tag{3.7}$$

$$\frac{\partial E}{\partial n}(\mathbf{x},\,t)=0,\qquad (\mathbf{x},\,t)\in\partial_3 G_T, \tag{3.8}$$

where $\partial/\partial n$ is the normal derivative. Conditions (3.6) and (3.7) are first order absorbing boundary conditions [16]. At the lateral boundaries we impose a homogeneous Neumann condition (3.8). In [14] it was shown that the solution to the original Maxwell's equations is well approximated by the solution to (3.3)–(3.8) in the case where $\xi=1$ and the discontinuities in ε_{r} are not too large.

The model problem (3.3)–(3.8) can be also rewritten as

$$\begin{aligned}
&\varepsilon_{\mathrm{r}}(\mathbf{x})\frac{\partial^2 E}{\partial t^2}(\mathbf{x},\, t)\\
&\quad + \nabla\big(\nabla\cdot E(\mathbf{x},\, t)\big) - \nabla\cdot\big(\nabla E(\mathbf{x},\, t)\big)\\
&\qquad - \xi\nabla\Big(\nabla\cdot\big(\varepsilon_{\mathrm{r}}(\mathbf{x})E(\mathbf{x},\, t)\big)\Big) = 0, \quad (\mathbf{x},\, t)\in G\times(0,\, T),
\end{aligned} \tag{3.9}$$

$$E(\mathbf{x},\, 0) = 0, \quad \frac{\partial E}{\partial t}(\mathbf{x},\, 0) = 0, \qquad \mathbf{x}\in G, \tag{3.10}$$

$$E\,(\mathbf{x},\, t) = (0,\, f\,(t)\,,\, 0), \qquad (\mathbf{x},\, t)\in \partial_1 G\times(0,\, t']\,, \tag{3.11}$$

$$\frac{\partial E}{\partial n}(\mathbf{x},\, t) = -\frac{\partial E}{\partial t}(\mathbf{x},\, t), \qquad (\mathbf{x},\, t)\in \partial_1 G\times(t',\, T)\,, \tag{3.12}$$

$$\frac{\partial E}{\partial n}(\mathbf{x},\, t) = -\frac{\partial E}{\partial t}(\mathbf{x},\, t), \qquad (\mathbf{x},\, t)\in \partial_2 G_T, \tag{3.13}$$

$$\frac{\partial E}{\partial n}(\mathbf{x},\, t) = 0, \qquad (\mathbf{x},\, t)\in \partial_3 G_T. \tag{3.14}$$

Here we have used the well-known identity $\nabla\times(\nabla\times E) = \nabla(\nabla\cdot E) - \nabla\cdot(\nabla E)$. We refer to [14] for details of the numerical solution of the forward problem (3.9)–(3.14).

3.2. Tikhonov functional. We define Γ' as the extension of the backscattering side Γ up to the boundary $\partial_3 G$ of the domain G that is,

$$\Gamma' = \left\{\mathbf{x} = (x,\, y,\, z) : -X < x < X,\, -Y < y < Y,\, z = c'\right\}.$$

Let G' be the part of the rectangular prism G which lies between the two planes Γ' and $\{z = -C\}$:

$$G' = \left\{\mathbf{x} = (x,\, y,\, z) : -X < x < X,\, -Y < y < Y,\, -C < z < c'\right\}.$$

Denote by $Q_T = G'\times(0,\, T)$, and $S_T = \partial G'\times(0,\, T)$.

In our CIP we have the data g in (3.2) only on Γ. These data are complemented on the rest of the boundary $\partial G'$ of the domain G' by simulated data using the immersing procedure of [5]. Thus, we can approximately get the vector function $\widetilde{g}$:

$$\widetilde{g}\,(\mathbf{x},\, t) = E\,(\mathbf{x},\, t)\,, \quad (\mathbf{x},t)\in S_T. \tag{3.15}$$

We solve our inverse problem as an optimization problem. To do so, we minimize the Tikhonov functional:

$$
\begin{aligned}
F(E,\,\varepsilon_{\mathrm{r}}) &:= \frac{1}{2}\int_{S_T}\big(E(\mathbf{x},\,t)-\tilde{g}(\mathbf{x},\,t)\big)^2 z_\delta(t)\,\mathrm{d}\sigma\,\mathrm{d}t \\
&\quad+\frac{1}{2}\gamma\int_G\big(\varepsilon_{\mathrm{r}}(\mathbf{x})-\varepsilon_{\mathrm{r,\,glob}}(\mathbf{x})\big)^2\,\mathrm{d}\mathbf{x},
\end{aligned}
\tag{3.16}
$$

where $\gamma>0$ is the regularization parameter and $\varepsilon_{\mathrm{r,\,glob}}$ is the computed coefficient which we have obtained on the first stage via the globally convergent method. Here, the function $z_\delta(t)$ is used to ensure the compatibility conditions at $\overline{Q}_T\cap\{t=T\}$ for the adjoint problem (also, see section 4.3 of [1]),

$$
z_\delta\in C^2[0,\,T],\quad z_\delta(t)=\begin{cases}1, & t\in(0,\,T-\delta),\\ \in(0,1), & t\in(T-\delta,\,T-\delta/2),\\ 0, & t\in(T-\delta/2,T).\end{cases}
$$

Let E_{glob} be the solution of the forward problem (3.9)–(3.14) with $\varepsilon_{\mathrm{r}}:=\varepsilon_{\mathrm{r,\,glob}}$. Denote by $p=\partial_n E_{\mathrm{glob}}|_{S_T}$. In addition to the Dirichlet condition (3.15), we set the Neumann boundary condition as

$$
\frac{\partial E}{\partial n}(\mathbf{x},\,t)=p(\mathbf{x},\,t),\quad(\mathbf{x},\,t)\in S_T.
$$

Introduce the following spaces of real valued vector functions

$$
\begin{gathered}
H_E^1(Q_T)=\left\{f\in[H^1(Q_T)]^3:f(\mathbf{x},\,0)=0\right\},\\
H_\lambda^1(Q_T)=\left\{f\in[H^1(Q_T)]^3:f(\mathbf{x},\,T)=0\right\},\\
U^1=H_E^1(G_T)\times H_\lambda^1(G_T)\times B(G),
\end{gathered}
$$

where $B(G)$ is the space of functions bounded on G with the norm $\|f\|_{B(G)}=\sup_G|f|$.

To minimize the functional (3.16) we introduce the Lagrangian

$$
\begin{aligned}
&L(E,\,\lambda,\,\varepsilon_{\mathrm{r}})\\
&\quad=F(E,\,\varepsilon_{\mathrm{r}})-\int_{Q_T}\varepsilon_{\mathrm{r}}(\mathbf{x})\frac{\partial\lambda}{\partial t}(\mathbf{x},\,t)\cdot\frac{\partial E}{\partial t}(\mathbf{x},\,t)\,\mathrm{d}\mathbf{x}\,\mathrm{d}t\\
&\qquad-\int_{Q_T}\nabla\cdot E(\mathbf{x},\,t)\nabla\cdot\lambda(\mathbf{x},\,t)\,\mathrm{d}\mathbf{x}\,\mathrm{d}t+\int_{Q_T}\nabla E(\mathbf{x},\,t)\nabla\lambda(\mathbf{x},\,t)\,\mathrm{d}\mathbf{x}\,\mathrm{d}t\\
&\qquad+\xi\int_{Q_T}\nabla\cdot\big(\varepsilon_{\mathrm{r}}(\mathbf{x})E(\mathbf{x},\,t)\big)\nabla\cdot\lambda(\mathbf{x},\,t)\,\mathrm{d}\mathbf{x}\,\mathrm{d}t-\int_{S_T}\lambda(\mathbf{x},\,t)\cdot p(\mathbf{x},\,t)\,\mathrm{d}\sigma\,\mathrm{d}t,
\end{aligned}
\tag{3.17}
$$

where E and λ are weak solutions of problems (3.19)–(3.21) and (3.22)–(3.24), respectively, see details in [5].

We observe that in (3.17) $(E,\, \lambda,\, \varepsilon_{\rm r}) = w \in U^1$ and functions E and λ depend on the $\varepsilon_{\rm r}$. To get the Fréchet derivative L' of the Lagrangian (3.17) rigorously, one should assume that variations of functions E and λ depend on variations of the coefficient $\varepsilon_{\rm r}$. This can be done similarly with section 4.8 of [1]. However for brevity here, to derive the Fréchet derivative of the Lagrangian (3.17), we assume that in (3.17) the elements of the vector function $(E,\, \lambda,\, \varepsilon_{\rm r})$ can be varied independently of each other.

We search for a point $w \in U^1$ such that

$$L'(w)\,(\overline{w}) = 0,\ \forall \overline{w} \in U^1. \tag{3.18}$$

To find the Fréchet derivative $L'(w)$, we consider $L\,(w+\overline{w}) - L\,(w)$, for every $\overline{w} \in U^1$ and single out the linear part, with respect to $\overline{w}$, of the obtained expression. Then the state problem in the domain G' is given by

$$\begin{aligned} &\varepsilon_{\rm r}(\mathbf{x})\frac{\partial^2 E}{\partial t^2}(\mathbf{x},\, t) + \nabla\big(\nabla\cdot E(\mathbf{x},\, t)\big) \\ &\quad - \nabla\cdot\big(\nabla E(\mathbf{x},\, t)\big) - \xi\nabla\Big(\nabla\cdot\big(\varepsilon_{\rm r}(\mathbf{x})E(\mathbf{x},\, t)\big)\Big) = 0, \quad (\mathbf{x},\, t) \in Q_T, \end{aligned} \tag{3.19}$$

$$E(\mathbf{x},\, 0) = 0, \quad \frac{\partial E}{\partial t}(\mathbf{x},\, 0) = 0, \qquad \mathbf{x} \in G', \tag{3.20}$$

$$\frac{\partial E}{\partial n}\,(\mathbf{x},\, t) = p\,(\mathbf{x}, t)\,, \qquad (\mathbf{x},\, t) \in S_T. \tag{3.21}$$

The adjoint problem is:

$$\begin{aligned} &\varepsilon_{\rm r}(\mathbf{x})\frac{\partial^2 \lambda}{\partial t^2}(\mathbf{x},\, t) + \nabla\big(\nabla\cdot\lambda(\mathbf{x},\, t)\big) \\ &\quad - \nabla\cdot\big(\nabla\lambda(\mathbf{x},\, t)\big) - \xi\varepsilon_{\rm r}(\mathbf{x})\nabla\big(\nabla\cdot\lambda(\mathbf{x},\, t)\big) = 0, \quad (\mathbf{x},\, t) \in Q_T, \end{aligned} \tag{3.22}$$

$$\lambda(\mathbf{x},\, T) = 0, \quad \frac{\partial \lambda}{\partial t}(\mathbf{x},\, T) = 0, \qquad \mathbf{x} \in G', \tag{3.23}$$

$$\frac{\partial \lambda}{\partial t}(\mathbf{x},\, t) = z_\delta\,(t)\,\big(\widetilde{g}(\mathbf{x},\, t) - E(\mathbf{x},\, t)\big)\,(\mathbf{x}, t)\,, \qquad (\mathbf{x},\, t) \in S_T. \tag{3.24}$$

4. Finite element discretization

For the finite element discretization of $\Omega_T = \Omega \times (0, T)$ we used the stabilized finite element method of [14]. To do that we define a partition $K_h = \{K\}$ of G' which consists of tetrahedra. Here h is a mesh function defined as $h|_K = h_K$ – the local diameter of the element K. Let $J_\tau = \{J\}$

be a partition of the time interval $(0,\, T)$ into subintervals $J = (t_{k-1},\, t_k]$ of uniform length $\tau = t_k - t_{k-1}$. We also assume the minimal angle condition on the K_h [17].

To solve the state problem (3.19)–(3.21) and the adjoint problem (3.22)–(3.24) we define the finite element spaces, $W_h^E \subset H_E^1(Q_T)$ and $W_h^\lambda \subset H_\lambda^1(Q_T)$. First, we introduce the finite element trial space W_h^E for every component of the electric field E defined by

$$W_h^E := \{w \in H_E^1(Q_T) : w|_{K\times J} \in P_1(K) \times P_1(J),\ \forall K \in K_h,\ \forall J \in J_\tau\},$$

where $P_1(K)$ and $P_1(J)$ denote the set of linear functions on K and J, respectively. We also introduce the finite element test space W_h^λ defined by

$$W_h^\lambda := \{w \in H_\lambda^1(Q_T) : w|_{K\times J} \in P_1(K) \times P_1(J),\ \forall K \in K_h,\ \forall J \in J_\tau\}.$$

Hence, the finite element spaces W_h^E and W_h^λ consist of continuous piecewise linear functions in space and time. To approximate the function ε_{r}, we use the space of piecewise constant functions $V_h \subset L_2(\Omega)$,

$$V_h := \{u \in L_2(\Omega) : u|_K \in P_0(K),\ \forall K \in K_h\},$$

where $P_0(K)$ is the set of constant functions on K.

Next, we set $U_h = W_h^E \times W_h^\lambda \times V_h$. The finite element method for solving equation (3.18) now reads: *Find* $u_h \in U_h$, *such that*

$$L'(u_h)(\bar{u}) = 0,\ \forall \bar{u} \in U_h.$$

5. General framework for a posteriori error estimates for our CIPs

Let $(E_h,\, \lambda_h,\, \varepsilon_h) \in U_h$ be finite element approximations of functions $(E,\, \lambda,\, \varepsilon_{\mathrm{r}}) \in U^1$, see details in [3, 14]. In our recent works [1, 18–20] we derived a posteriori error estimates for three kinds of errors:

- The error $|L(u) - L(u_h)|$ of the Lagrangian with $u = (E,\, \lambda,\, \varepsilon_{\mathrm{r}})$, and $u_h = (E_h,\, \lambda_h,\, \varepsilon_h)$ [18, 19].
- The error $|F(\varepsilon_{\mathrm{r}}) - F(\varepsilon_h)|$ of the Tikhonov functional [1].
- The error $|\varepsilon_{\mathrm{r}} - \varepsilon_h|$ of the regularized solution ε_{r} of this functional. This error for hyperbolic CIPs was presented in [1, 6].

To derive errors in the Lagrangian or in the Tikhonov functional we first note that

$$\begin{aligned} L(u) - L(u_h) &= L'(u_h)(u - u_h) + R(u,\, u_h), \\ F(\varepsilon_{\mathrm{r}}) - F(\varepsilon_h) &= F'(\varepsilon_h)(\varepsilon_{\mathrm{r}} - \varepsilon_h) + R(\varepsilon_{\mathrm{r}},\, \varepsilon_h), \end{aligned} \tag{5.1}$$

where $R(u,\, u_h)$,and $R(\varepsilon_{\rm r},\, \varepsilon_h)$ are the second order remainders terms. We assume that ε_h is located in the small neighborhood of $\varepsilon_{\rm r}$. This assumption is reasonable, since we have a good initial guess both in the Tikhonov functional and in the Lagrangian. This guess is obtained by the globally convergent method of [1, 9, 21]. Thus, the terms $R(u,\, u_h)$, $R(\varepsilon_{\rm r},\, \varepsilon_h)$ are small and we can neglect them in (5.1).

We now use the Galerkin orthogonality principle

$$L'(u_h)(\bar{u}) = 0 \ \forall \bar{u} \in U_h,$$
$$F'(\varepsilon_h)(b) = 0 \ \forall b \in V_h,$$

together with the splitting

$$u - u_h = (u - u_h^{\rm I}) + (u_h^{\rm I} - u_h),$$
$$\varepsilon_{\rm r} - \varepsilon_h = (\varepsilon_{\rm r} - \varepsilon_h^{\rm I}) + (\varepsilon_h^{\rm I} - \varepsilon_h),$$

where $u_h^{\rm I} \in U_h$ is the interpolant of u, and $\varepsilon_h^{\rm I} \in V_h$ is the interpolant of $\varepsilon_{\rm r}$, and get the following representation of errors in the Lagrangian and in the Tikhonov functional, respectively:

$$\begin{aligned} L(u) - L(u_h) &\approx L'(u_h)(u - u_h^{\rm I}), \\ F(\varepsilon_{\rm r}) - F(\varepsilon_h) &\approx F'(\varepsilon_h)(\varepsilon_{\rm r} - \varepsilon_h^{\rm I}). \end{aligned} \tag{5.2}$$

In the a posteriori error estimates (5.2) we have two types of "factors":

- $L'(u_h)$ and $F'(\varepsilon_h)$ represent *residuals*, and
- $u - u_h^{\rm I}$ and $\varepsilon_{\rm r} - \varepsilon_h^{\rm I}$ represent *weights*.

While the residuals in (5.2) can be computed by knowing the finite element approximations $(E_h,\, \lambda_h,\, \varepsilon_h)$, weights must be further estimated.

Let $f \in H^1(\Omega)$ be approximated by its piecewise linear interpolant $f_h^{\rm I}$ and finite element approximation f_h over a mesh K_h of Ω as outlined in Section 4. Standard interpolation estimates (following from, for instance, [22]) then gives

$$\left\| f - f_h^{\rm I} \right\|_{L_2(\Omega)} \leq C_{\rm I} \left\| h \ \nabla f \right\|_{L_2(\Omega)}. \tag{5.3}$$

where $C_{\rm I} = C_{\rm I}\,(\Omega,\, h)$ is positive constant depending only on the domain Ω and the mesh function $h = h(x)$, the latter defined as in Section 4. In addition, we can estimate right hand side in (5.3), see [22], via

$$|\nabla f| \leq \frac{|[f_h]|}{h_K}, \tag{5.4}$$

where $[f_h]$ denotes the normal jump of the function f_h over the edges of the element K.

Similarly with (5.3), (5.4) we estimate $u - u_h^{\mathrm{I}}$ in terms of derivatives of the function u and the mesh parameters h and τ as

$$|u - u_h^{\mathrm{I}}| \leq C_{\mathrm{I}} \left(h^2 \left| \frac{[u_h]_{\mathrm{s}}}{h} \right| + \tau^2 \left| \frac{[u_h]_{\mathrm{t}}}{\tau} \right| \right), \tag{5.5}$$

where $[u_h]_{\mathrm{s}}$ is the maximum modulus of a jump in the normal derivative of u_h across a side of the element K, $[u_h]_{\mathrm{t}}$ is the maximum modulus of the jump of the time derivative of u_h across a boundary node of the time interval J, see details in [3, 18, 19, 23].

We also estimate $\varepsilon_{\mathrm{r}} - \varepsilon_h^{\mathrm{I}}$ in terms of derivatives of the function ε_{r} and the mesh parameter h as

$$|\varepsilon_{\mathrm{r}} - \varepsilon_h^{\mathrm{I}}| \leq C_{\mathrm{I}} h \left| \frac{[\varepsilon_h]}{h} \right|. \tag{5.6}$$

Here, $[\varepsilon_h]$ is the jump of the function ε_h over the element K. Substituting estimates (5.5) and (5.6) in the right hand side of (5.2) we can compute a posteriori errors in the Lagrangian or in the Tikhonov functional in explicit way as

$$|L(u) - L(u_h)| \approx C_{\mathrm{I}} ||L'(u_h)|| \cdot (h||[u_h]_{\mathrm{s}}|| + \tau||[u_h]_{\mathrm{t}}||),$$
$$|F(\varepsilon_{\mathrm{r}}) - F(\varepsilon_h)| \approx C_{\mathrm{I}} ||F'(\varepsilon_h)|| \cdot |||[\varepsilon_h]|||.$$

Finally, to derive an estimate for the error $\varepsilon_{\mathrm{r}} - \varepsilon_h$ in the regularized solution ε_{r}, we use the fact that the Tikhonov functional is strictly convex in a small neighborhood of the solution [1]. In addition, we use the interpolation property (5.3). We now formulate a theorem of [1] for the case of a posteriori error estimate in the reconstructed function ε_{r} for the problem (2.1)–(2.2).

Theorem [1] *Let $\varepsilon_h \in V_h$ be a finite element approximation of the solution $\varepsilon_{\mathrm{r}} \in H^1(\Omega)$ obtained after the minimization of the functional (3.16) on the finite element mesh K_h with the mesh function h. Then there exists a constant D such that $\|F'(\varepsilon_1) - F'(\varepsilon_2)\| \leq D\|\varepsilon_1 - \varepsilon_2\|$ for every ε_1, ε_2 satisfying* (2.3). *In addition, the following a posteriori error estimate for the regularized solution ε_{r} holds*

$$||\varepsilon_h - \varepsilon_{\mathrm{r}}||_{L^2(\Omega)} \leq \frac{D}{\alpha} C_I ||h\varepsilon_h||_{L_2(\Omega)}.$$

Remark 5.1. The natural question linked with the adaptivity is: Can one rigorously guarantee that the mesh obtained after the minimization of

the Tikhonov functional on sequentially refined meshes of finite elements results in an improvement of the accuracy? The first affirmative answer to this question was presented in [4], also, see the book [1] and the survey [6].

6. Mesh refinement recommendation and the adaptive algorithm

In our adaptive algorithm for the mesh refinement we have used ideas of [19], Theorem 5.1 and the criterion of Remark 5.1 of [3]. From this criterion follows that the finite element mesh should be locally refined in such subdomain of Ω where the maximum norm of the Fréchet derivative of the objective functional is large.

Define

(6.1)
$$L_h'^{,m}(\mathbf{x}) = -\int_0^T \frac{\partial \lambda_h^m}{\partial t}(\mathbf{x},\, t) \cdot \frac{\partial E_h^m}{\partial t}(\mathbf{x},\, t)\,\mathrm{d}t + \xi \int_0^T \nabla \cdot E_h^m(\mathbf{x},\, t) \nabla \cdot \lambda_h^m(\mathbf{x},\, t)\,\mathrm{d}t + \gamma(\varepsilon_h{}^m(\mathbf{x}) - \varepsilon_{\mathrm{r,\,glob}}(\mathbf{x})),$$

where m is the iteration index in the optimization procedure, and $(E_h^m,\, \lambda_h^m,\, \varepsilon_h^m)$ are finite element approximations of the functions $(E,\, \lambda,\, \varepsilon_{\mathrm{r}})$, see details in [3, 14].

Adaptive algorithm

- Step 0. Choose an initial mesh K_h in Ω and an initial time partition J_0 of the time interval $(0,\, T)$. Start from the initial guess $\varepsilon_h^0 = \varepsilon_{\mathrm{r,\,glob}}$. Compute the approximations ε_h^m as:
- Step 1. Compute the approximate solutions E_h^m and λ_h^m of the state problem (3.19)–(3.21) and the adjoint problem (3.22)–(3.24) on K_h and J_k, using coefficient ε_h^m, and compute the Fréchet derivative $L_h'^{,m}$ via (6.1).
- Step 2. Update the coefficient on K_h using the conjugate gradient method:

$$\varepsilon_h^{m+1}(\mathbf{x}) := \varepsilon_h^m(\mathbf{x}) + \alpha d^m(\mathbf{x}),$$

where $\alpha > 0$ is a step-size in the conjugate gradient method, and

$$d^m(\mathbf{x}) = -L_h'^{,m}(\mathbf{x}) + \beta^m d^{m-1}(\mathbf{x}),$$

with

$$\beta^m = \frac{||L_h'^{,m}||^2_{L_2(\Omega)}}{||L_h'^{,m-1}||^2_{L_2(\Omega)}},$$

and $d^0(\mathbf{x}) = -L_h'^{,0}(\mathbf{x})$.

- Step 3. Stop updating the coefficient and set $\varepsilon_h := \varepsilon_h^{m+1}$, $M := m+1$, if either $||L_h'^{,m}||_{L_2(\Omega)} \leq \theta$ or norms $||\varepsilon_h^m||_{L_2(\Omega)}$ are stabilized. Here θ is a tolerance number. Otherwise, set $m := m+1$ and go to step 1.
- Step 4. Compute $L_h'^{,M}$ via (6.1). Refine the mesh at all grid points $\mathbf{x}$ where

$$|L_h'^{,M}(\mathbf{x})| \geq \beta_1 \max_{\mathbf{x}\in\overline{\Omega}} |L_h'^{,M}(\mathbf{x})|.$$

  Here the tolerance number $\beta_1 \in (0, 1)$ is chosen by the user.
- Step 5. Construct a new mesh K_h in Ω and a new partition J_k of the time interval $(0, T)$. On J_k the new time step τ should be chosen in such a way that the CFL condition is satisfied. Interpolate the initial approximation $\varepsilon_{\mathrm{r,glob}}$ from the previous mesh to the new mesh. Next, return to step 1 at $m = 1$ and perform all above steps on the new mesh. Stop mesh refinements if norms defined in step 3 either increase or stabilize, compared with the previous mesh.

In step 2 of this algorithm the parameter α can be computed by a line search procedure, see, e.g. [24].

7. Numerical studies

In this section we present results of reconstructions of buried objects placed inside a sand box, using our two-stage numerical procedure. To do this, we use the globally convergent algorithm of section 2 on the first stage and the adaptive algorithm of section 6 on the second. To collect experimental data, we have used the same configuration as for the targets placed in the air, see [7, 8] for details. The only difference is that in this work we consider the objects placed inside a box filled with the dry sand. We refer to [2] for details of the data acquisition process. The relative dielectric constant of dry sand is $\varepsilon_{\mathrm{r}}(\mathrm{sand}) = 4$. We used this information to model the case of buried objects. In our experiment we have used different types of targets, including both metallic and nonmetallic ones.

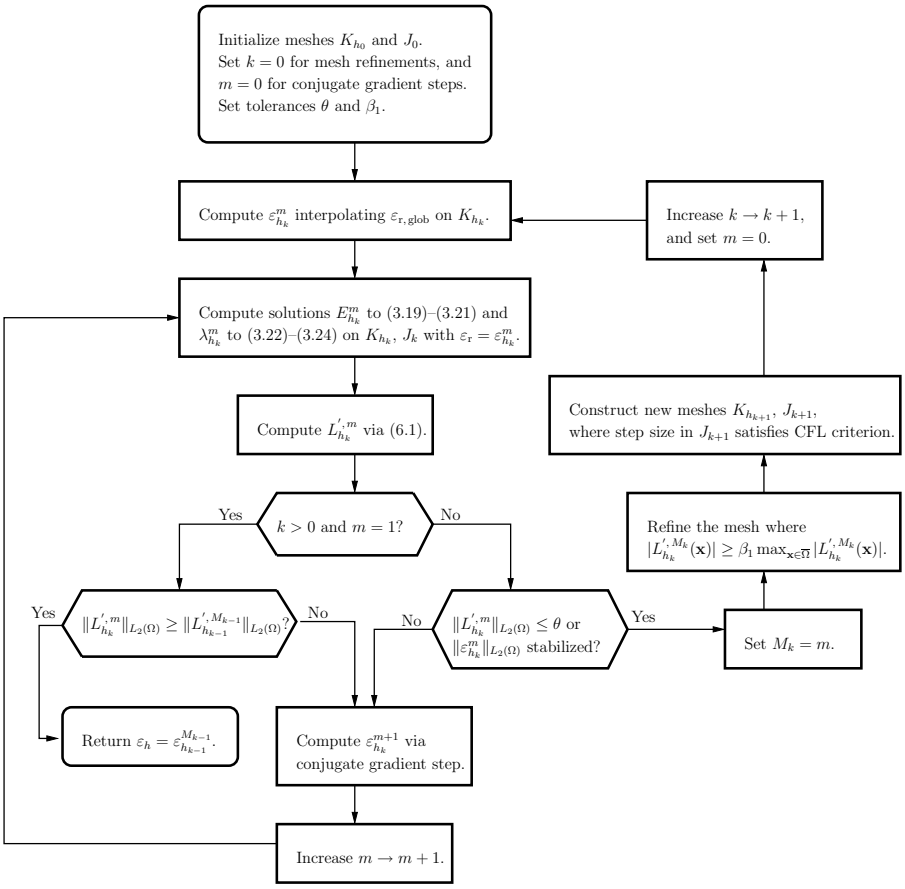

FIGURE 2. Flowchart for the adaptive algorithm.

We refer to the Table 1 of [2] for the full description of all data sets. In this paper we present reconstruction of eight (8) objects listed in the Table 1 below.

Our experimental setup includes a horn antenna (transmitter) which was fixed at a given position, and a detector. The scanned area was 1×1 (m) with space step 0.02 (m). Electrical pulses were emitted by the transmitter and received at each position of the detector. Pulses were generated by a Picosecond Pulse Generator 10070A and the backscattered

signals were measured by Tektronix DSA70000 series real-time oscilloscope. The emitted pulses were of the duration 300 picoseconds. The wavelength of the pulses was approximately 0.04 m. The timestep between two sets of recorded backscattered data was $\tau = 10$ ps. Duration of the time signal was 10 ns.

In our computational studies we had the following goals:

- to reconstruct refractive indices of dielectric targets and appearing dielectric constants of metals, and
- to image the location of targets, and their sizes and shapes.

To work with metallic objects, it is convenient to treat them as dielectrics with large dielectric constants, see [25] for details. We call these *appearing dielectric constants* and choose values for them such that

$$\varepsilon_{\mathrm{r}}\,(\text{metallic target}) \geq 10. \tag{7.1}$$

To compare our computational results with directly measured refractive indices $n = \sqrt{\varepsilon_{\mathrm{r}}}$ of dielectric targets and appearing dielectric constants of metallic targets (see (7.1)), we consider the maximal values of the computed functions ε_{r} obtained in both algorithms, and define

$$\varepsilon_{\mathrm{r}}^{\mathrm{comp}} = \max_{\mathbf{x}\in\overline{\Omega}} \varepsilon_{\mathrm{r}}\,(\mathbf{x})\,, \quad n^{\mathrm{comp}} = \sqrt{\varepsilon_{\mathrm{r}}^{\mathrm{comp}}}. \tag{7.2}$$

Remark 7.1. As the objects we reconstruct are buried in dry sand with relative dielectric constant 4, our computational results should be scaled by that factor in order to obtain correct apparent dielectric constants and refractive indices. In Tables 2, 3, we present such scaled results.

7.1. Data preprocessing. We point out that there is a *huge misfit* between our experimental data and computationally simulated data. There are several causes of this misfit listed in Section 4.2 of [8]. Because of this misfit, the *central procedure* required before applying of our two-stage numerical procedure is data preprocessing. This procedure is heuristic and cannot be rigorously justified. In this work we have used the same data preprocessing procedure consisting of several steps as was used in [8]. The three main steps of our data preprocessing procedure are:

(1) Data propagation.
(2) Extraction of the target's signal from the total signal, which is a mixture of the signal from the target and the signal from the sand. This extraction is applied to propagated data.

(3) Data calibration: to scale the measured data to the same scaling as in our simulations. In the case of the globally convergent method, a calibrating object was used. In the case of the above described adaptive finite element method a different calibration was used, see for details [5].

We have propagated the data to a plane, which we call the *propagated plane* and is located closer to the targets. This means that we approximate the scattered wave on the propagated plane using the measured scattered wave on the measurement plane. The distance between the measurement plane and the target was found using first time of arrival of the backscattered signal. A data calibration procedure was used to scale the measured data by a certain factor obtained in our computational simulations. We call this factor the *calibration factor*. The choice of this factor is based on the data of a known target which we call the *calibrating object*. The procedure of the extraction of the signal of the target from the total signal is more complicated and we refer to [2] for its many details.

7.2. Computational domains. We set spatial dimensions in our experiment in meters. Our experimental data were collected at the measurement plane which was about 0.8 m from targets. The data were collected at the detectors with a scanning step size in space 0.02 m in x and y directions. We choose the dimensionless spatial and time variables $\mathbf{x}' = \mathbf{x}/1$ (m), $t' = 0.3t$ where t is the time in nanoseconds (ns). The factor 0.3 is the speed of light in m/ns in free space. This factor was used to normalize the dielectric constant to be unity in the background medium. The time interval was chosen $t' \in [0, 1.2]$ since the amplitude of the signal for $t' > 1.2$ was negligibly small [2]. Below we keep the same notations x, t for dimensionless variables for brevity. As to the specific choice of sizes of domains below, we have slightly varied them and saw that these variations did not affect significantly our results. We also kept in mind that we cannot use exceedingly large domains due to the computational cost.

In our computations we propagated the experimentally measured data from measurement plane $P_{\rm m} = \{z = 0.8\}$ to the plane $P_{\rm p} = \{z = 0.04\}$. This means that the distance between front sides of our targets and the backscattered boundary was approximately 0.04 m. We choose this distance in all our computations since we have obtained good reconstruction results for all targets using this distance, see details in [2]. Thus, we work

below in both algorithms only with propagated experimental data given at the plane $P_{\rm p} = \{z = 0.04\}$.

We choose our computational domain G as

(7.3)
$$G = \{\mathbf{x} = (x,\, y,\, z) \in (-0.56,\, 0.56) \times (-0.56,\, 0.56) \times (-0.16,\, 0.1)\}\,.$$

The boundary of the domain G is $\partial G = \partial_1 G \cup \partial_2 G \cup \partial_3 G$. Here, $\partial_1 G$ and $\partial_2 G$ are front and back sides of the domain G at $\{z = 0.1\}$ and $\{z = -0.16\}$, respectively, and $\partial_3 G$ is the union of left, right, top and bottom sides of this domain.

For the solution of the state problem (3.19)–(3.21) and the adjoint problem (3.22)–(3.24) we have used domain decomposition finite element/finite difference method of [14]. To do that the the domain G is split into two subdomains $\Omega_{\rm FEM} = \Omega$ and $\Omega_{\rm FDM}$ so that $G = \Omega_{\rm FEM} \cup \Omega_{\rm FDM}$ and inner domain is defined as

(7.4)
$$\Omega_{\rm FEM} = \Omega = \{\mathbf{x} = (x,\, y,\, z) \in (-0.5,\, 0.5) \times (-0.5,\, 0.5) \times (-0.1,\, 0.04)\}\,.$$

The experimental data g for both algorithms are given at the front side Γ of the domain Ω which is defined as

$$\Gamma = \{\mathbf{x} = (x,\, y,\, z) \in \partial\Omega : z = 0.04\}.$$

In some tests of the first stage we used the shrunken computational domain G defined as

$$G = \{\mathbf{x} = (x,\, y,\, z) \in (-0.24,\, 0.24) \times (-0.24,\, 0.24) \times (-0.16,\, 0.1)\}\,,$$

as well as the shrunken computational domain $\Omega_{\rm FEM}$ defined as

(7.5)
$$\Omega_{\rm FEM} = \Omega = \{\mathbf{x} = (x,\, y,\, z) \in (-0.2,\, 0.2) \times (-0.2,\, 0.2) \times (-0.1,\, 0.04)\}\,.$$

7.3. Description of experimental data sets. Table 1 describes the details of used data sets together with the burial depths of the targets. After obtaining computational results the refractive indices of all dielectric targets were measured, and these measured refractive indices were compared to those predicted by the computations.

We note that the burial depths of the objects of Table 1 varied between 2 cm to 10 cm. Typically burial depths of antipersonnel land mines do not exceed 10 cm. The measured data of the sand box (without buried objects) was used for the calibration of all data for the objects of Table 1.

7.4. Numerical examples of the first stage. In Tables 2 and 3 we summarize reconstruction results for all objects of Table 1. Table 2 shows shows the reconstructed refractive indices for the non-metallic targets. For these targets, the refractive index $n = \sqrt{\varepsilon_{\mathrm{r}}(\text{target})}$. Here, $\varepsilon_{\mathrm{r}}(\text{target})$ was chosen as $\varepsilon_{\mathrm{r}}(\text{target}) = \max_{\mathbf{x}\in\Omega} \varepsilon_{\mathrm{r}}(\mathbf{x})$. Table 3 shows the burial depths and the effective dielectric constants of the metallic targets. From Tables 2 and 3 we can see that the burial depth was accurately estimated in most cases, with the errors not exceeding 1 cm.

The estimates of the refractive indices of non-metallic targets with refractive indices larger than that of the sand (water and wet wood) are quite accurate with the average error of about 4%.

For water, we were unable to directly measure its refractive index at the used frequency of the signal, which was about 7.5 GHz. Since this is a high frequency, then we cannot rely on the standard value of the refractive index of water

$$n\,(\text{water}) = \sqrt{\varepsilon_{\mathrm{r}}\,(\text{water})} = \sqrt{80} \approx 8.94,$$

which is given in many tables of dielectric constants for low frequencies. Therefore, we have made a separate experiment described in [2], where we have obtained a reference value $n\,(\text{water}) = 4.88$. This value has coincided with the value of an experimental paper cited in [26], see details in [2]. We observe from Table 2 that our computed value of n for water is close to the reference value. Targets with refractive indices smaller than that of the sand model plastic land mines and improvised explosive devices (IEDs). We have observed that in this case we can image these targets only if their burial depths do not exceed 5 cm, see for example, reconstruction of Object #3 in Table 2 and in Figure 4-c).

In our experiments we observed that the signals of the metallic targets were stronger compared to the signal from sand. By (7.1) appearing dielectric constant of metals should be larger than 10, also, see [25]. We see from Table 3 that our results for metallic objects satisfy this criterion.

We observe in Table 1 that in our experiment for Object #4 we were supposed to reconstruct two metallic blocks with 1 cm separation between them. On the other hand, the wavelength of our device is $\lambda = 4.5$ cm. Thus, $\lambda/4.5$ is the distance between these two targets. Table 3 and Figure 4-d) show that we have accurately imaged both targets. Thus, we have achieved the *superresolution* beyond the diffraction limit. This phenomenon is rare and should be studied further because of its importance when combined with quantitative imaging.

7.5. Numerical examples of the second stage. We can conclude from the results of the first stage that this stage provides accurate locations of the targets as well as accurate values of the refractive indices $n = \sqrt{\varepsilon_r}$ of the dielectric targets and large values of appearing dielectric constants ε_r for the metallic targets. However, the globally convergent algorithm does not reconstruct shapes of targets well, see Figure 4. To refine shapes, we have used the second stage, on which we have minimized the Tikhonov functional on locally adaptively refined meshes.

7.5.1. *Computations of the forward problem.* The data g in our experiments of the second stage are given only for the second component E_2 of the electric field E in (3.2) and are measured on the front side Γ of the domain Ω,

$$\Gamma = \{\mathbf{x} = (x, y, z) \in \partial\Omega : z = 0.04\}.$$

To generate backscattering data for other two components E_1 and E_3 we solve the forward problem (3.9)–(3.14) in the computational domain G defined as in the first stage in (7.3) with the known value of ε_r obtained at the first stage of our two-stage numerical procedure. We use the stabilized domain decomposition method of [14] implemented in the software package WavES [27]. We split G into two subdomains $\Omega_{\text{FEM}} = \Omega$ and Ω_{FDM} so that $G = \Omega_{\text{FEM}} \cup \Omega_{\text{FDM}}$ and the inner domain is defined as in (7.4).

Once the forward problem (3.9)–(3.14) is solved to generate backscattering data for the two components E_1 and E_3 at the boundary Γ', then after the data immersing procedure described in Section 7.3.3 of [5] the inverse problem is solved via the algorithm of section 6. The immersing procedure of [5] immerses the time-dependent propagated experimental data $g(\mathbf{x}, t) = E_2(\mathbf{x}, t)|_{\mathbf{x}\in\Gamma}$ into the computationally simulated data and then extends the data g from Γ to Γ'.

We choose the waveform f in (3.9)–(3.14) as

$$f(t) = \sin(\omega t), \quad 0 \le t \le t' := \frac{2\pi}{\omega},$$

where we use $\omega = 30$ and $T = 1.2$. We solve the problem (3.9)–(3.14) using the explicit scheme of [14] with the time step size $\tau = 0.003$, which satisfies the CFL condition.

7.5.2. *Reconstructions.* Suppose that in the adaptive algorithm of section 6 we have obtained the function ε_r. We obtain then the image of

the dielectric targets based on the function $\varepsilon_{\mathrm{r,\,diel}}$, which we define as

$$\varepsilon_{\mathrm{r,\,diel}}(\mathbf{x}) = \begin{cases} \varepsilon_{\mathrm{r}}(\mathbf{x}) \ \text{ if } \varepsilon_{\mathrm{r}}(\mathbf{x}) \geq 0.5 \max_{\mathbf{x}\in\overline{\Omega}} \varepsilon_{\mathrm{r}}(\mathbf{x}), \\ 1 \text{ otherwise.} \end{cases}$$

For metallic targets use a similar function $\varepsilon_{\mathrm{r,\,metal}}$,

$$\varepsilon_{\mathrm{r,\,metal}}(\mathbf{x}) = \begin{cases} \varepsilon_{\mathrm{r}}(\mathbf{x}) \ \text{ if } \varepsilon_{\mathrm{r}}(\mathbf{x}) \geq 0.5 \max_{\mathbf{x}\in\overline{\Omega}} \varepsilon_{\mathrm{r}}(\mathbf{x}), \\ 1 \text{ otherwise.} \end{cases}$$

Table 2 displays computed and directly measured refractive indices of dielectric objects as well as their correct and calculated burial depths. These computations were made on the first stage. One can see that refractive indices are reconstructed pretty accurately. Burial depths of Objects #2 and #3 are reconstructed accurately. However, the error in the calculated burial depth of object #6 is 4.3 cm.

Table 3 displays computed appearing dielectric constants of metallic objects as well as their true and calculated burial depths. Again, these computations were done on the first stage. One can see that in all cases burial depths were calculated with a good accuracy. As to the computed values of appearing dielectric constants, they all exceed 10, which is in a good agreement with (7.1). An interesting observation which can be derived from Table 3 is that even though burial depths of targets Objects #7 and #8 were significantly different (3 cm in #7 and 10 cm in #8), our reconstructed values of their appearing dielectric constants were the same.

As to the second stage, computed refractive indices of dielectric targets and appearing dielectric constants of metallic targets, were very close to ones of the first stage.

Recall that in order to apply immersing procedure of the experimental data g into simulated data E_2, we solve the problem (3.9)–(3.14) numerically with the known values of the function $\varepsilon_{\mathrm{r}} = \varepsilon_{\mathrm{r,\,glob}}$ obtained at the first stage of our two-stage numerical procedure. Figure 3 shows backscattering immersed data of the second component of electric field E_2 for Object #4 (two metallic blocks) of Table 1 at different times

Figures 5–11 display 3D reconstructions of Objects #1–#6 of Table 1. Figures 12, 13 present adaptively refined meshes and 3D images of Objects #7, #8 of Table 1, respectively. To obtain a better visualization, we have zoomed some figures from the domain Ω_{FEM} defined in (7.4) to the domain defined in (7.5). We can conclude that the location of

Object #	Description of target	Material
1	A metallic ball, 3 cm burial depth	Metal
2	A bottle filled with clear water, 3.6 cm burial depth	Water
3	A ceramic mug, 5 cm burial depth	Ceramic
4	Two metallic blocks at 1 cm separation, 4 cm burial depth	Metal/Metal
5	Metallic prism, 2 cm burial depth	Metal
6	Wet wooden block, 9.8 cm burial depth	Water
7	Two metallic prisms at 6 cm separation, 3 cm burial depth	Metal/Metal
8	Two metallic prisms at 6 cm separation, 10 cm burial depth	Metal/Metal

TABLE 1. *Description of the data sets. Note that although targets for Object #7 and Object #8 are the same, their burial depths are different.*

Object #	Material	Computed depth (cm)	Exact depth (cm)	Computed n	Measured n
2	Water	3.6	4.0	4.7	4.88
3	Ceramic	4.0	5.0	1.0	1.39
6	Wet wood	5.5	9.8	4.2	4.016

TABLE 2. *Results of the first stage: the refractive indices* $n = \sqrt{\varepsilon_{\mathrm{r}}}$ *and the burial depths of non-metallic targets.*

all targets as well as their sizes in the x-, y-, and z-directions are well estimated on the second stage of our two-stage numerical procedure.

8. Summary

This is the fifth (5th) paper (after [2, 5, 7, 8]) in the recent series of publications of this group about the performance of the two-stage numerical procedure of [1] on experimental backscattering time-dependent data generated by a single location of the source of electromagnetic waves. While in [5, 7, 8] we have considered the case of targets placed in air, in [2] and here we consider the more challenging case of targets buried in the ground. This case is more challenging because the signal scattered by the ground is heavily mixed with the signal scattered by the target.

Object #	Material	Computed depth (cm)	Exact depth (cm)	Computed ε_r
1	Metal	2.9	3.0	31.0
4	Metal	3.8	4.0	99.8
	Metal	4.0	4.0	56.5
5	Metal	1	2	50.0
7	Metal	3.0	3.0	23.4
	Metal	3.6	3.0	30.5
8	Metal	7.3	10.0	23.4
	Metal	8.2	10.0	30.5

TABLE 3. *Results of the first stage: the estimated effective dielectric constants and the burial depths of metallic targets. Object #4 consists of two metallic targets with 1 cm distance between their surfaces (case of the superresolution). Objects #7, #8 also consist of two metallic targets, see Table 1.*

It was shown in [2] that the globally convergent numerical method of [1] accurately images refractive indices and locations of buried targets. In this paper we complement that globally convergent method by the locally convergent adaptivity technique. The adaptivity takes the image of the globally convergent method as the starting point for subsequent iterations. The theory of the adaptivity was fully developed in [1, 3, 4, 6, 10, 18–20, 23, 28, 29] In particular, the important analytical guarantee of the fact that adaptivity indeed refines images was first established in [4] and then also published in [1] and [6]. As a result of the application of the adaptivity, our images are significantly refined: the shapes of the targets are accurately imaged. A particularly interesting case is the case of the superresolution (Figure 4-d and Figures 9). We have accurately imaged both targets in this case. We also refer to the recent paper [30] for a numerical study of the method of [1] for a CIP for a hyperbolic PDE, which is different from (2.1).

In conclusion, we believe that the two-stage numerical procedure of [1] is now completely verified on experimental data.

Acknowledgments

This research was supported by US Army Research Laboratory and US Army Research Office grant W911NF-11-1-0399, the Swedish Research Council, the Swedish Foundation for Strategic Research (SSF) through the Gothenburg Mathematical Modelling Centre (GMMC). The

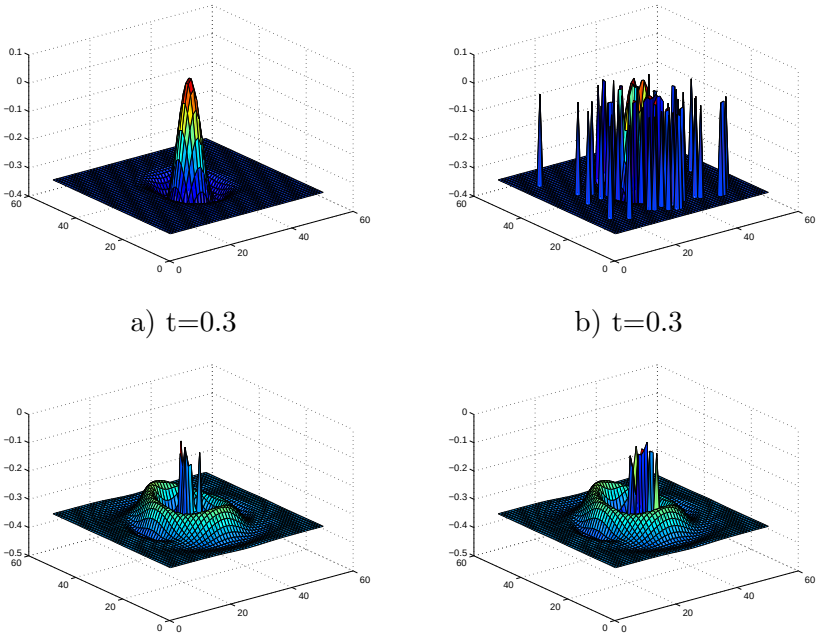

a) t=0.3 b) t=0.3

c) t=0.45 d) t=0.45

FIGURE 3. Backscattering immersed data of the second component E_2 of the electric field for Object #4 (two metallic blocks at 1 cm separation) of Table 1. On the left we show backscattering immersed data which are immersed into measured data without presence of sand, on the right - with presence of sand. Recall that the final time is $T = 1.2$.

computations were performed on resources at Chalmers Centre for Computational Science and Engineering (C3SE) provided by the Swedish National Infrastructure for Computing (SNIC).

References

[1] L. Beilina, M. Klibanov, Approximate Global Convergence and Adaptivity for Coefficient Inverse Problems, Springer, New York, 2012.

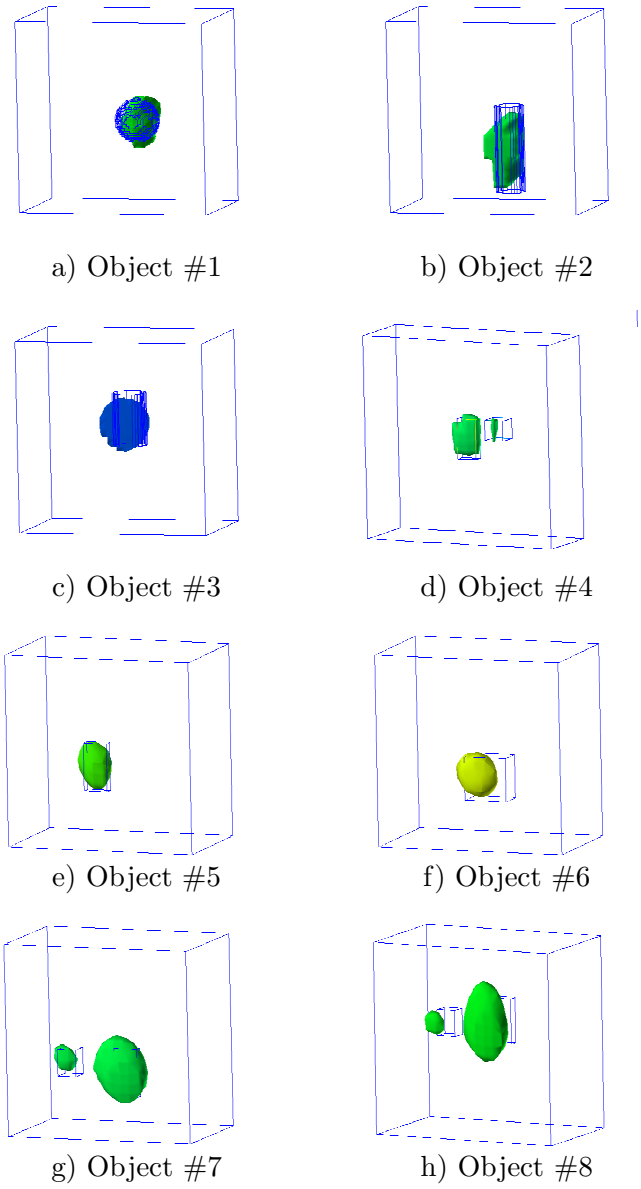

a) Object #1 b) Object #2

c) Object #3 d) Object #4

e) Object #5 f) Object #6

g) Object #7 h) Object #8

FIGURE 4. *Reconstructions of targets of Table 1 obtained on the first stage of our two-stage numerical procedure.*

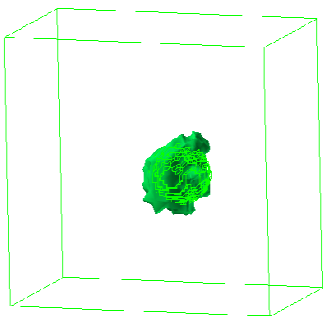

a) three times refined mesh, xy-view

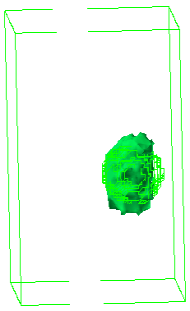

b) three times refined mesh, yz-view

FIGURE 5. *Computed image of Object #1 of Table 1 . Thin lines indicate correct shape. To have a better visualization we have zoomed the domain* Ω *in (7.4) in the domain* Ω_{FEM} *in (7.5).*

[2] N. T. Thành, L. Beilina, M. V. Klibanov, M. A. Fiddy, Imaging of buried objects from experimental backscattering radar measurements using a globally convergent inverse algorithm, preprint, available online at arxiv: 1406.3500, 2014 as well as at Chalmers Publication Library, http://www.math.chalmers.se/Math/Research/Preprints/, preprint number 2014-15.

[3] L. Beilina, Adaptive finite element method for a coefficient inverse problem for the Maxwell's system, Applicable Analysis 90 (2011) 1461–1479.

[4] L. Beilina, M. Klibanov, M. Kokurin, Adaptivity with relaxation for ill-posed problems and global convergence for a coefficient inverse problem, Journal of Mathematical Sciences 167 (2010) 279–325.

[5] L. Beilina, N. T. Thành, M. V. Klibanov, J. B. Malmberg, Reconstruction of shapes and refractive indices from backscattering experimental data using the adaptivity, Inverse Problems 30 (2014) 105007.

[6] L. Beilina, M. Klibanov, Relaxation property for the adaptivity for ill-posed problems, Applicable Analysis 93 (2013) 223–253.

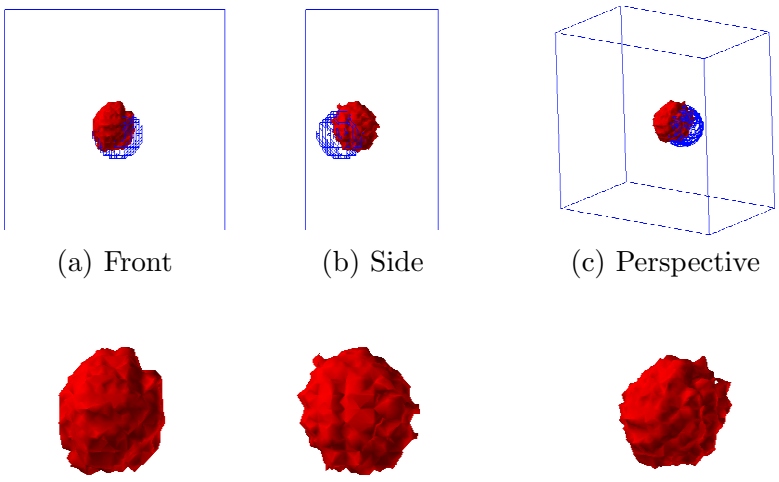

(a) Front (b) Side (c) Perspective

(d) Front, zoomed (e) Side, zoomed (f) Perspective, zoomed

FIGURE 6. Three views and zooms of the reconstruction of the Object #1 of Table 1 on the three times refined mesh. The initial guess in this test is taken from Test 2 of [2], see Figure 5.1-b),d) of [2]. Recall that Object #1 is a metallic ball.

[7] L. Beilina, N. T. Thành, M. V. Klibanov, M. A. Fiddy, Reconstruction from blind experimental data for an inverse problem for a hyperbolic equation, Inverse Problems 30 (2014) 025002.

[8] N. T. Thành, L. Beilina, M. V. Klibanov, M. A. Fiddy, Reconstruction of the refractive index from experimental backscattering data using a globally convergent inverse method, SIAM J. Scientific Computing 36 (2014) B273–B293.

[9] L. Beilina, M. Klibanov, A new approximate mathematical model for global convergence for a coefficient inverse problem with backscattering data, J. Inverse and Ill-Posed Problems 20 (2012) 513–565.

[10] M. Klibanov, A. Bakushinskii, L. Beilina, Why a minimizer of the Tikhonov functional is closer to the exact solution than the first guess?, J. Inverse and Ill-posed problems 19 (2011) 83–105.

[11] F. Simonetti., Localization of pointlike scatterers in solids with subwavelength resolution, Appl. Phys. Lett. 89 (2006) 094105.

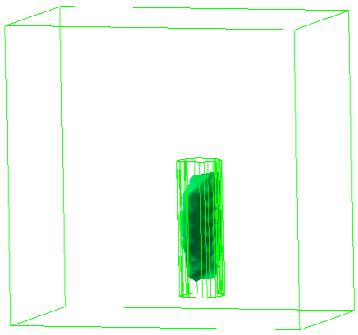

a) twice refined mesh, xy-view

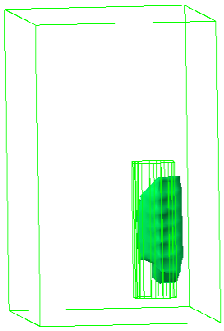

b) twice refined mesh, yz-view

FIGURE 7. *Computed image of Object #2 of Table 1 . Thin lines indicate correct shape. To have a better visualization we have zoomed the domain* Ω *in (7.4) in the domain* Ω_{FEM} *in (7.5). This target, which was a plastic bottle filled with water, was quite a large vertical size of 20 cm. On the other hand, our incident signal had a low power, which was much lower at the top and bottom of this target. This is why we were unable to image well the vertical size of this target. Still, one can observe that the image is stretched in the vertical direction.*

[12] F.-C. Chen, W. C. Chew, Experimental verification of superresolution in nonlinear inverse scattering, App. Phys. Lett. 72 (1998) 3081–3086.

[13] H. Ammari, J. Garnier, J. de Rosny, K. Solna, Medium induced resolution enhancement broadband imaging, Inverse Problems 30 (2014) 085006.

[14] L. Beilina, Energy estimates and numerical verification of the stabilized domain decomposition finite element/finite difference approach for the Maxwell's system in time domain, Central European Journal of Mathematics 11 (2013) 702–733.

[15] A. L. Bukhgeim, M. V. Klibanov, Uniqueness in the large of a class of multidimensional inverse problems, Soviet Math. Doklady 17 (1981) 244–247.

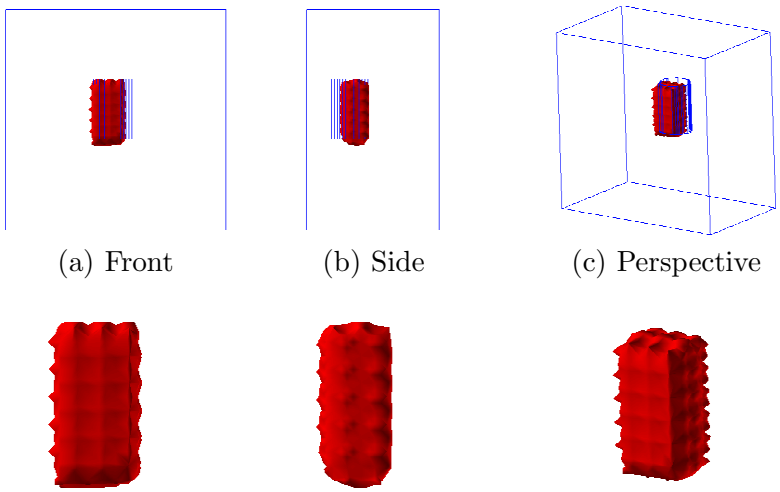

(a) Front (b) Side (c) Perspective

(d) Front, zoomed (e) Side, zoomed (f) Perspective, zoomed

FIGURE 8. Three views and zooms of the reconstruction of the Object #3 of Table 1 on the once refined mesh. Recall that Object #3 is a ceramic mug.

[16] B. Engquist, A. Majda, Absorbing boundary conditions for the numerical simulation of waves, Math. Comp. 31 (1977) 629–651.
[17] S. C. Brenner, L. R. Scott, The Mathematical theory of finite element methods, Springer-Verlag, Berlin, 2012.
[18] L. Beilina, C. Johnson, A hybrid fem/fdm method for an inverse scattering problem, in: Numerical Mathematics and Advanced Applications, ENUMATH 2001, Springer-Verlag, Berlin, 2001.
[19] L. Beilina, C. Johnson, A posteriori error estimation in computational inverse scattering, Mathematical Models in Applied Sciences 1 (2005) 23–35.
[20] L. Beilina, M. Klibanov, A posteriori error estimates for the adaptivity technique for the Tikhonov functional and global convergence for a coefficient inverse problem, Inverse Problems 26 (2010) 045012.
[21] L. Beilina, M. Klibanov, The philosophy of the approximate global convergence for multidimensional coefficient inverse problems, Complex Variables and Elliptic Equations 57 (2-4) (2012) 277–299.

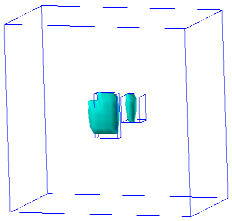

a) coarse mesh

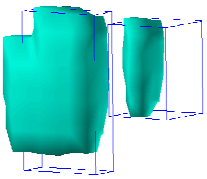

b) zoomed view

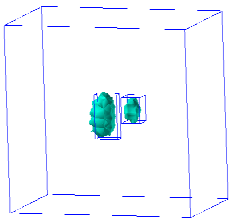

c) two times refined mesh

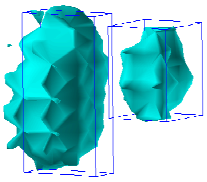

d) zoomed view

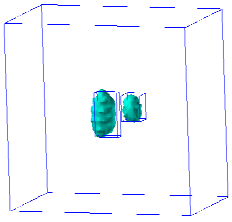

e) three times refined mesh

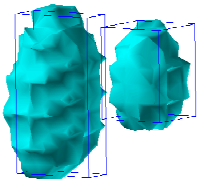

f) zoomed view

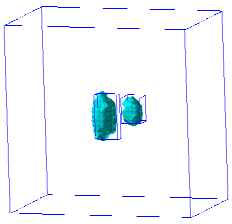

g) four times refined mesh

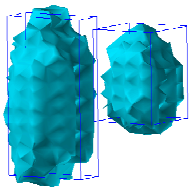

h) zoomed view

FIGURE 9. *Computed images of Object #4 of Table 1 when the superresolution is achieved on four times adaptively refined meshes. Compare with Figure 4-d).*

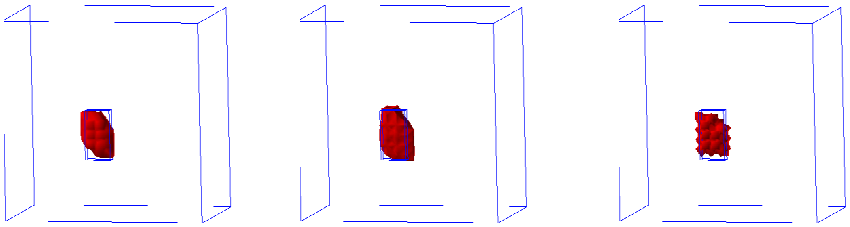

a) once refined mesh b) twice refined mesh c) three times refined mesh

FIGURE 10. *Reconstructions of Object #5 of Table 1 on adaptively refined meshes.*

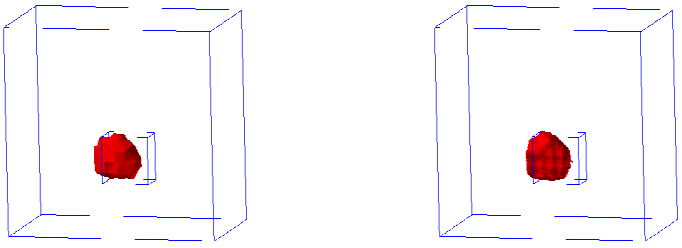

a) once refined mesh twice refined mesh

FIGURE 11. *Reconstructions of Object #6 of Table 1 on adaptively refined meshes.*

[22] K. Eriksson, D. Estep, C. Johnson, Calculus in Several Dimensions, Springer-Verlag, Berlin, 2004.

[23] L. Beilina, Adaptive hybrid fem/fdm methods for inverse scattering problems, Inverse problems and information technologies 1 (2002) 73–116.

[24] O. Pironneau, Optimal Shape Design for Elliptic Systems, Springer-Verlag, Berlin, 1984.

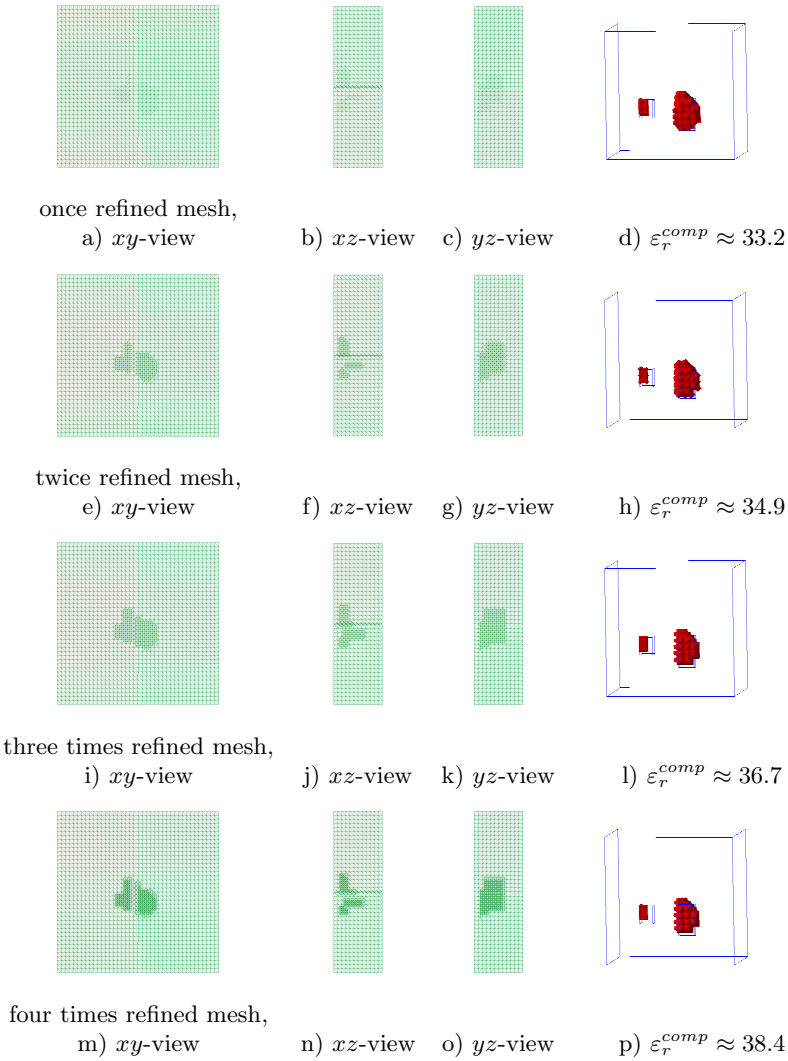

FIGURE 12. *Reconstructions of Object #7 of Table 1 on adaptively refined meshes.*

[25] A. V. Kuzhuget, L. Beilina, M. V. Klibanov, A. Sullivan, L. Nguyen, M. A. Fiddy, Blind experimental data collected in the field and an

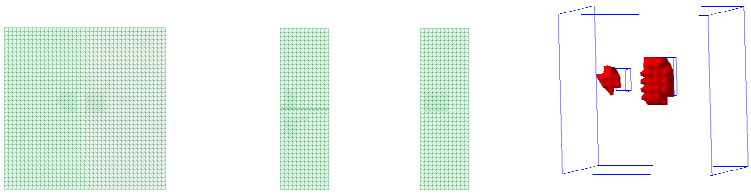

once refined mesh,
a) xy-view b) xz-view c) yz-view d) $\varepsilon_r^{comp} \approx 32.7$

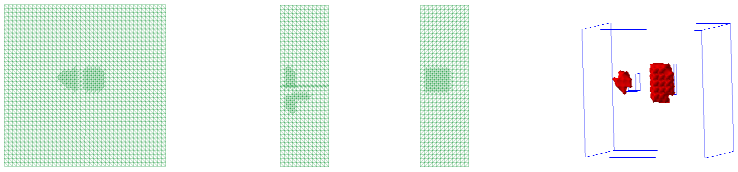

twice refined mesh,
e) xy-view f) xz-view g) yz-view h) $\varepsilon_r^{comp} \approx 34.5$

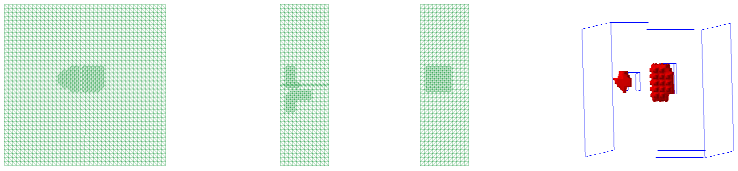

three times refined mesh,
i) xy-view j) xz-view k) yz-view l) $\varepsilon_r^{comp} \approx 37.4$

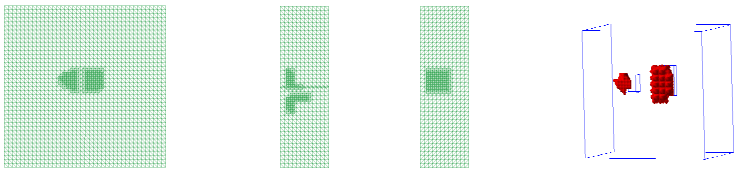

four times refined mesh,
m) xy-view n) xz-view o) yz-view p) $\varepsilon_r^{comp} \approx 39$

FIGURE 13. *Reconstructions of Object #8 of Table 1 on adaptively refined meshes.*

approximately globally convergent inverse algorithm, Inverse Problems 28 (2012) 095007.

[26] E. Farr, C. Frost, Impulse propagation measurements of dielectric properties of water, dry sand, moist sand and concrete, Tech. rep., Farr Research, Measurement Note 52 (1997).

[27] WavES, the software package. URL `http://www.waves24.com`

[28] M. Asadzadeh, L.Beilina, A posteriori error analysis in a globally convergent numerical method for a hyperbolic, Inverse Problems 26 (2010) 115007.

[29] L. Beilina, M. Klibanov, Synthesis of global convergence and adaptivity for a hyperbolic coefficient inverse problem in 3d, J. Inverse and Ill-Posed Problems 18 (2010) 85–132.

[30] Y. Chow, J. Zou, A numerical method for reconstructing the coefficient in a wave equation, Numerical Methods for Partial Differential Equations, published online, DOI: 10.1002/num.21904.